MIT/WHOI

Massachusetts Institute of Technology
Woods Hole Oceanographic Institution

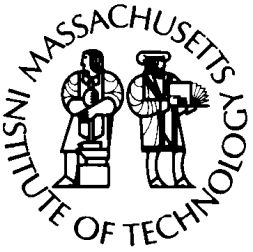

Joint Program in Oceanography/ Applied Ocean Science and Engineering

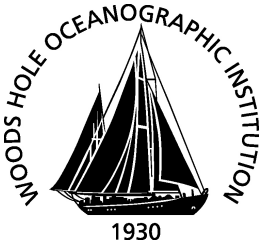

DOCTORAL DISSERTATION

The Response of Ocean Salinity Patterns to Climate Change: Implications for Circulation

by

Samuel J. Levang

June 2019

The Response of Ocean Salinity Patterns to Climate Change: Implications for Circulation

by

Samuel J. Levang

B.A., Macalester College (2012)

Submitted to the Joint Program in Oceanography & Applied Ocean Science & Engineering
in partial fulfillment of the requirements for the degree of

Doctor of Philosophy in Physical Oceanography

at the

MASSACHUSETTS INSTITUTE OF TECHNOLOGY

and the

WOODS HOLE OCEANOGRAPHIC INSTITUTION

June 2019

Author .....
MIT-WHOI Joint Program in Oceanography & Applied Ocean Science & Engineering
May 13, 2019

Certified by .....
Raymond W. Schmitt
Scientist Emeritus
Woods Hole Oceanographic Institution
Thesis Supervisor

Accepted by ....
Glenn R. Flierl
Chairman, Joint Committee for Physical Oceanography
Massachusetts Institute of Technology

The Response of Ocean Salinity Patterns to Climate Change: Implications for Circulation

by

Samuel J. Levang

Submitted to the MIT-WHOI Joint Program in Oceanography & Applied Ocean Science & Engineering
on May 13, 2019, in partial fulfillment of the
requirements for the degree of
Doctor of Philosophy in Physical Oceanography

Abstract

Global patterns of ocean salinity arise from the exchange of freshwater between the sea surface and the atmosphere. For a quasi-steady state system, these surface fluxes are balanced by compensating transports of salt in the ocean interior. In a warming climate, the atmosphere holds additional water vapor which acts to intensify the global water cycle. Amplified freshwater fluxes are then absorbed at the surface and propagate along ocean circulation pathways. Here, we use coupled model results from the CMIP5 experiment to identify coherent responses in the atmospheric water cycle and in ocean salinity patterns. Some aspects of the response are consistent across models, while other regions show large inter-model spread. In particular, the salinity response in the North Atlantic subpolar gyre, where the mean salinity plays a role in maintaining high surface density for deep-water formation, has low confidence in CMIP5 models.

To understand how differences in ocean circulation may affect this response, we use two techniques to diagnose the role of salt transports in the present-day climate. The first is a salt budget within the surface mixed layer, which identifies major transport processes. The second is a Lagrangian particle tracking tool, used to understand the regional connectivity of water masses. From this analysis, we find that anomalous freshwater signals become well mixed within the ocean gyres, but can be isolated on larger scales. The subpolar Atlantic salinity response generally shows freshening at the surface, but is sensitive to the transport of anomalously salty water from the subtropics, a largely eddy-driven process. As CMIP5 models use a range of eddy parameterizations, this is likely a source of uncertainty in the salinity response. Finally, we investigate the effect of salinity changes on the deep overturning cells and other circulations, and find a complex influence that also depends on the details of advective pathways. In a warming scenario, water cycle amplification actually works to strengthen the Atlantic meridional overturning circulation due to the influence of enhanced subtropical evaporation.

Thesis Supervisor: Raymond W. Schmitt
Title: Scientist Emeritus
Woods Hole Oceanographic Institution

Acknowledgments

First, I would like to sincerely thank my advisor Ray Schmitt for all the support he has provided during my time in the Joint Program. We have had many stimulating discussions over the years that have inspired the bulk of my scientific interests. Ray has been generous with his time, given me the freedom to pursue whatever scientific questions I found exciting, and offered exceptional flexibility as a supervisor. I couldn't have asked for a better advisor.

The remaining members of my thesis committee have also been essential in guiding this thesis. John Marshall helped steer the work towards impactful questions with his expertise in the AMOC and climate dynamics. Tom Farrar offered his detail-oriented focus and knowledge of upper ocean dynamics to ensure accuracy in the budgets and other calculations presented here. Arnold Gordon provided many useful insights on the role of oceanic connectivity and inter-basin exchange to support the global perspective of this thesis. Caroline Ummenhofer kindly agreed to chair the defense and succinctly summarized the revisions needed to produce a final draft.

I would also like to thank many other great people involved in the Joint Program. The professors and scientists at MIT and WHOI taught me most of what I know about the oceans and climate. The administrative staff have been exceptionally helpful in navigating the details of this complex program. My classmates have made the last 6 years truly fun.

Finally, I owe immense gratitude to my family. My parents, Jim and Julie, inspired my curiosity at a young age and have provided endless support through the years. My wife and best friend Emma generously agreed to move to Cambridge for my studies, and has kept me sane through the completion of my degree.

Funding for this thesis was provided by NASA grant NNX12AF59GS03, a NASA Earth and Space Science Fellowship award 80NSSC17K0372, and the WHOI Academic Programs Office.

THIS PAGE INTENTIONALLY LEFT BLANK

Contents

THIS PAGE INTENTIONALLY LEFT BLANK

List of Figures

List of Tables

THIS PAGE INTENTIONALLY LEFT BLANK

Chapter 1

Introduction

The transport of water molecules between oceans, atmosphere, land, and ice is collectively known as the "global water cycle." On land, water is often scarce, and life as we know it depends on the whims of seasonal rainfall. In the ocean, of course, water is plentiful, and the major impact of the water cycle is to alter the ocean's salinity by diluting or concentrating its salt content. The close match between the pattern of sea surface salinity (SSS) and the net rate of evaporation (E) minus precipitation (P) has been noted since at least Wüst (1936). In the present-day climate, seawater is 3.5% salt by weight on average, or 35 practical salinity units (psu), varying from around 32 psu in the tropical Pacific and Arctic, up to 38 psu in the evaporative North Atlantic subtropical gyre.

In a changing climate, such as that due to anthropogenic greenhouse gas emissions, fundamental thermodynamic influences alter the water cycle, also affecting the distribution of ocean salinity. This thesis focuses on the salinity changes that occur in a warming climate, and the oceanic processes that control those changes. Furthermore, salinity is an important contributor to several components of the ocean circulation, namely the thermohaline currents which are forced by density differences, and we seek to understand salinity change in the context of circulation.

Because salinity is only forced at the surface, we focus primarily on the sea surface salinity here, where the response is strongest. Changes in deep ocean salinity also occur following new surface forcing, but are largely an advective propagation of changes felt along outcropping isopycnal surfaces (Walin, 1982). The final chapter of this thesis investigates the subsurface changes in the context of circulation. Furthermore, we focus on changes over

the 21st century, the period for which extensive climate modeling simulations exist.

1.1 The Combined Ocean-Atmosphere Water Cycle

Best estimates indicate that 85% of E and 77% of P occur over the oceans (Schanze et al., 2010), making up the vast majority of the global water cycle. The climatological $E-P$ field predominantly controls SSS (see Fig. 1-1), and these patterns are a result of the global atmospheric circulation. The subtropical Hadley cell consists of a precipitative ascending branch in the Intertropical Convergence Zone (ITCZ) and a dry descending branch in the midlatitudes. Further poleward, the Ferrell cell creates another zone of high precipitation in the high latitudes. Evaporation rates over the ocean are a function of temperature, near-surface humidity, and wind speed. The subtropics, having a favorable combination of all these variables, are regions of high evaporation, with the warm western boundary currents having the strongest rates of evaporation. The subtropical oceans can be considered the primary source of water vapor for the global atmosphere, with 63% of E occurring over the ocean between the latitudes of 10° to 40° N/S (34% of Earth's surface area). Much of this water is transported equatorward via the trade winds, or poleward via mesoscale weather systems.

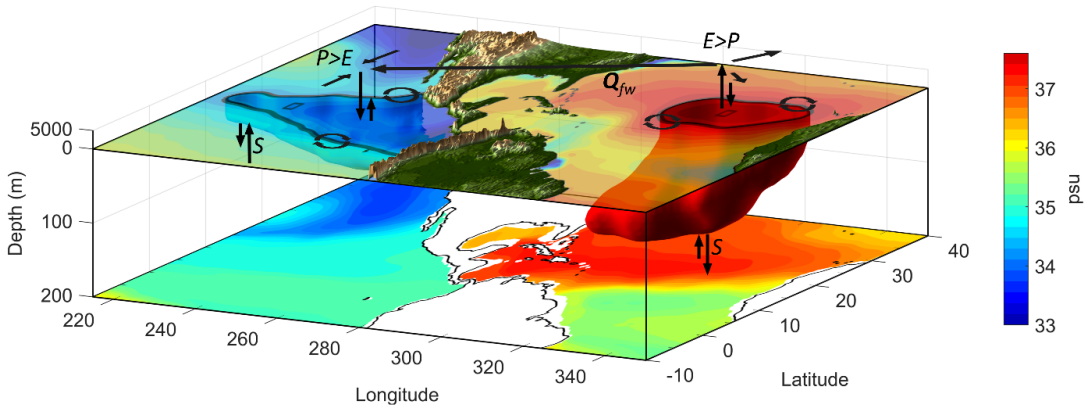

Figure 1-1: Schematic view of how the water cycle sets the ocean salinity field. In regions where $E > P$, the atmosphere exports moisture and the ocean becomes saltier. Where $E < P$, the atmosphere imports moisture and freshens the ocean. Advection and mixing then must transport freshwater into (salty water out of) dry regions and salty water into (freshwater out of) precipitative ones. This process occurs both within ocean basins, transporting water between different latitude bands, and between basins, such as the significant moisture transport from Atlantic to Pacific.

Salinity is forced directly at the ocean surface by these fluxes, along with smaller contributions from runoff in coastal areas and from sea-ice in the high latitudes. This leads to a pattern of high salinity in the subtropics and lower salinities in the tropics and high latitudes. The atmosphere also transports moisture over land between the three major ocean basins. Across the Americas, there is a relatively large flux of moisture from Atlantic to Pacific which is not balanced by an equivalent transport across Africa. Subsequently, the Atlantic is around 2 psu saltier than the Pacific at most latitudes.

While there is a strong correlation between the mean fields of SSS and $E-P$, the relationship is not exact. When the two are superimposed (Fig. 1-2), it is evident that ocean circulation alters the salinity pattern. For example: subtropical SSS maxima are displaced poleward relative to the corresponding $E-P$ maxima due to Ekman advection; relatively fresh streaks protrude equatorward from the high latitudes in the return flow of the gyres and in locations of coastal upwelling; and the poleward flanks of the subtropical gyres are saltier than the local $E-P$ would suggest due to advection of waters in the western boundary current extensions.

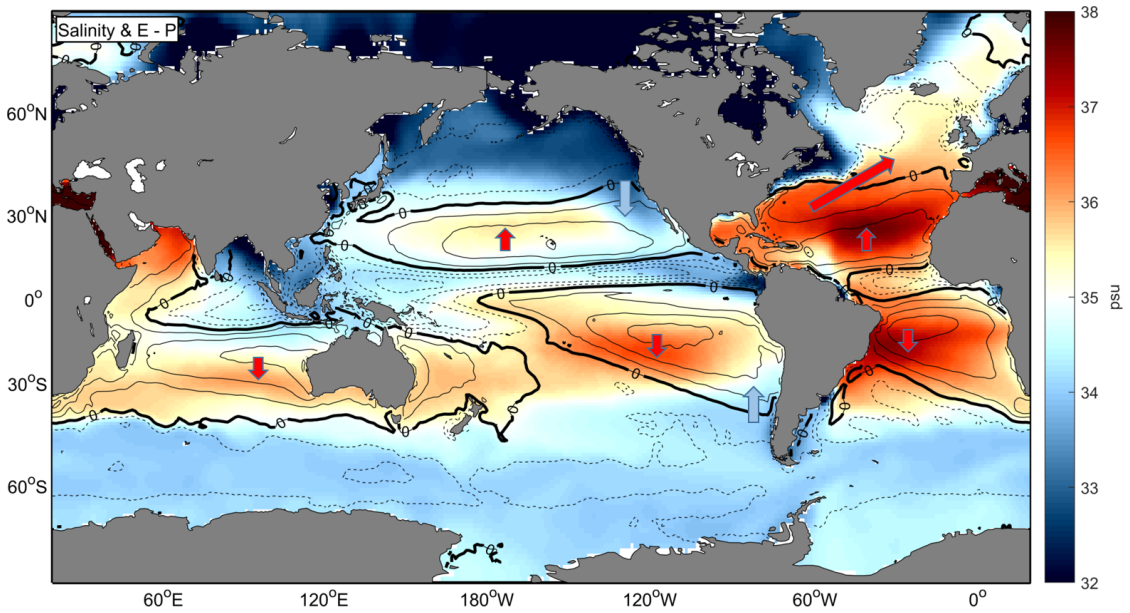

Figure 1-2: Climatological average SSS from Argo and other profiles (dataset described in Chapter 3) in color overlaid with contours of the annual average $E-P$ calculated from GPCP and OAflux data. Contours are $0.4\,\mathrm{m\,yr^{-1}}$ with freshwater flux into the ocean indicated by dashed lines and freshwater flux out of the ocean in solid lines. Areas where SSS features have been displaced relative to the corresponding $E-P$ pattern by ocean circulation are indicated with arrows.

Another way in which circulation affects the salinity pattern is through the mean salinity of each basin. As the peak evaporation rate in each of the five subtropical gyres is nearly identical, there must be another reason why the North Pacific is 2 psu fresher than the North Atlantic. The largest difference between the two basins is the higher rates of P and larger relative area of the Pacific ITCZ. These waters are then spread via mixing and advection, such that the freshening influence of the ITCZ is communicated to the rest of the basin.

1.2 Role of Salinity in Ocean Circulation and Climate

Unlike temperature, salinity does not feedback directly on atmospheric freshwater fluxes, meaning that salt can be considered a quasi-passive tracer within the ocean for many purposes, an idea that will be explored in more detail in this thesis. That is not to say, however, that the oceanic component of the water cycle doesn't play an important role in global climate, as latent heat fluxes associated with evaporation from the ocean are the dominant supply of energy to the atmosphere in many regions (Yu and Weller, 2007).

The addition and removal of freshwater at the ocean surface drives a direct barotropic flow known as the Goldsbrough circulation (Goldsbrough, 1933). In the subtropical gyres, this flow opposes the wind driven circulation but is roughly an order of magnitude smaller. In the North Atlantic, the southward boundary current associated with the Goldsbrough circulation reaches about 2 Sv, likely impacting the separation point of the Gulf Stream (Huang and Schmitt, 1993).

Perhaps more importantly, salinity plays a role in the so-called thermohaline circulations of the ocean. In both the high-latitude North Atlantic and the coastal margins of Antarctica, dense convective plumes work to set water properties for the entire abyssal ocean. These convective water masses are very cold ($-2\,^{\circ}$C to $2\,^{\circ}$C), but must also be relatively salty. Salt is particularly important in determining density gradients in the high latitudes, because the thermal expansion coefficient of seawater becomes small at low temperatures.

Fig. 1-3 shows where salinity provides a stabilizing or destabilizing influence on the ocean's surface layer. At both poles, there is a broad region where stable density stratification is provided primarily by salinity. Additionally, significant precipitation in the tropics generates stable salinity stratification there, and the phenomenon of "barrier layers." Across all of the subtropics, salt provides a destabilizing influence on the surface layer.

An interesting feature apparent in Fig. 1-3 is the difference between the North Atlantic and North Pacific subpolar gyres. In the North Atlantic, high salinity destabilizes the surface due to propagation of subtropical water along the upper limb of the Atlantic Meridional Overturning Circulation (AMOC). This is in contrast to the North Pacific, which has a more stable stratification and no deep overturning circulation. The salinity of the North Atlantic subpolar gyre is thought to be an important element of the AMOC dynamics, and is explored in more detail in Chapters 4 and 5.

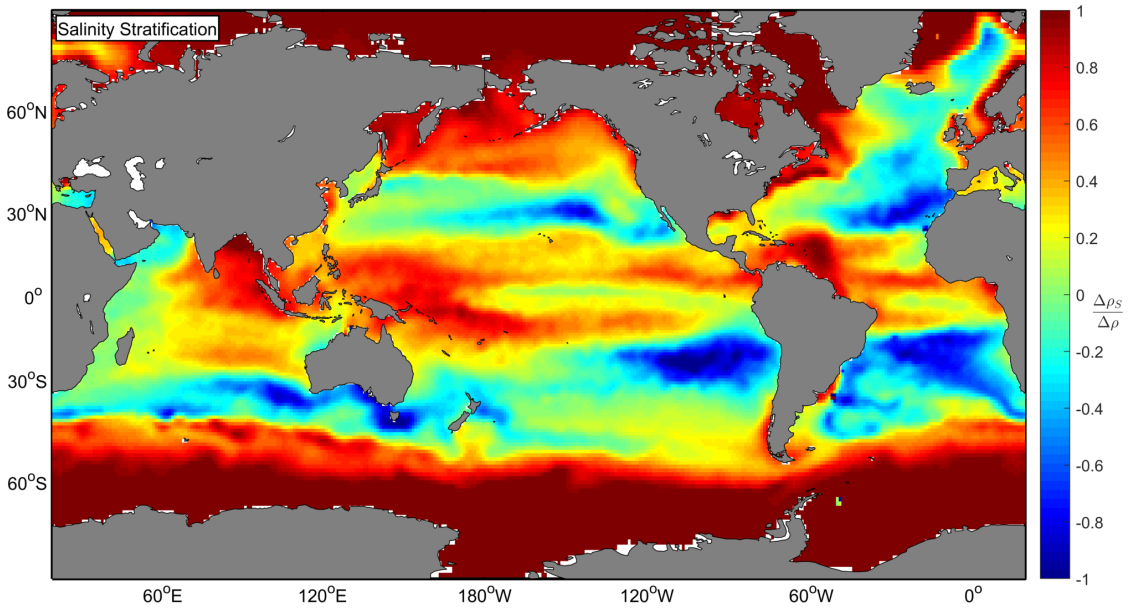

Figure 1-3: The fraction of the density difference from top to bottom of the surface mixed-layer ($\frac{\Delta\rho_S}{\Delta\rho}$) due to salinity. Where salinity provides all of the stable stratification the value is 1, and where salinity is destabilizing the value is negative. Salinity entirely controls the stratification at high latitudes, and also stabilizes the tropical surface layer. Salinity is destabilizing in the subtropics and in the subpolar North Atlantic.

1.3 Water Cycle in a Warming Climate

As Earth's temperature warms, the atmosphere holds more moisture according to the Clausius-Clapeyron relation. Increased specific humidity leads to increased moisture fluxes in the atmosphere. Even with uniform warming and fixed circulation, increased humidities result in greater convergences and divergences of water vapor in the atmosphere. This phenomenon leads to the classic "dry-get-dryer" and "wet-get-wetter" response to warming, often referred to as an intensification or amplification of the water cycle.

The response of the atmospheric water cycle to warming has been well studied (Held

and Soden, 2006), although uncertainty remains in the precise rates of intensification and regional details of the response (Stephens et al., 2010; Hegerl et al., 2014).

The ocean salinity response has also received significant attention (i.e. Durack et al., 2012). Changes in climatological salinity are a direct response to altered atmospheric freshwater fluxes, and the salinity field gradually accumulates these changes over time. It has therefore been suggested that salinity measurements, which tend to be smoother and less noisy than precipitation measurements, may be useful as an independent monitoring tool for the atmospheric water cycle (the so-called "ocean rain-gauge"). Because of the complicating role of ocean salt transports, many authors have encouraged caution in directly assigning salinity changes as a 1:1 intensification of $E - P$ patterns (Vinogradova and Ponte, 2017). However, little progress has been made in understanding precisely how the oceanic response may differ from the atmospheric one.

1.4 Thesis Organization

In the context of these motivating factors, this thesis strives to bridge the gap between the water cycle and ocean salinity responses in the present-day climate change scenario. The driving questions are as follows:

- How robust is the atmospheric water cycle response seen in coupled climate models?
- How do patterns of salinity change differ from the patterns of precipitation change, and what are the uncertainties in the salinity response?
- What are the dominant ocean transport processes that maintain the mean salinity field?
- How might newly-forced salinity anomalies propagate along these pathways?
- What impact can salinity change have on ocean circulation, particularly the AMOC?

Chapter 2 begins with a broad assessment of the water cycle in state-of-the-art coupled ocean-atmosphere models from the Coupled Model Intercomparison Project Phase 5 (CMIP5). We start from these complex simulations to identify where a robust response arises between different models, and to determine aspects of the dynamics that are uncertain and require further study.

Chapter 3 uses a mixed-layer budget framework to assess the role of different processes in maintaining the ocean's quasi-steady salinity field. We derive a fully closed budget from an ocean state-estimate and compare it to terms derived from observational products. This budget is used to identify major advective and mixing pathways for salt transport within the ocean's surface mixed-layer. We hypothesize that in regions of fast lateral transport, such as the Ekman-driven subtropical cells, imposed salinity anomalies may be rapidly mixed between regions.

Chapter 4 takes the passive tracer framework for salinity anomalies a step further and develops a Lagrangian methodology to directly propagate salinity anomalies along existing circulation pathways. We test a hypothesis that the salinity response can largely be captured by assuming a steady-state ocean circulation and propagating projected freshwater flux anomalies through an estimate of the current ocean circulation. A new Lagrangian accumulation methodology is developed for this experiment, which allows for detailed tracking of connectivity pathways, and a deeper understanding of how salinity anomalies propagate through the global circulation. We also explore the impact of mesoscale eddies on the salinity response by testing different velocity fields including resolved and parameterized eddies. With this technique, we focus specifically on the North Atlantic to study the salinity response in the deep water formation sites of the AMOC, which is an uncertain component of the climate system in CMIP5.

Chapter 5 diagnoses how the salinity changes in CMIP5 influence the AMOC, by extending the analysis to subsurface changes and investigating the propagation of surface anomalies in the deep limb of the AMOC. We find that salinity changes under water cycle intensification actually act to strengthen the overturning circulation, contrary to previous theories.

Chapter 6 provides a summary of the thesis work and directions for future research.

THIS PAGE INTENTIONALLY LEFT BLANK

Chapter 2

CMIP5 Coupled Model Projections of the Water Cycle and Salinity

A version of this work was published as: Levang, S. J. and Schmitt, R. W. (2015). Centennial Changes of the Global Water Cycle in CMIP5 Models. *Journal of Climate*, 28(16):6489–6502. DOI: 10.1175/JCLI-D-15-0143.1

2.1 Abstract

The global water cycle is predicted to intensify under various greenhouse gas emissions scenarios. Here we assess the nature and strength of the expected changes for the ocean in the coming century by examining the output of several CMIP5 model runs for the periods 1990 to 2000 and 2090 to 2100 and comparing them to a dataset built from modern observations. Key elements of the water cycle, such as the atmospheric vapor transport, the evaporation minus precipitation over the ocean and the surface salinity, show significant changes over the coming century. The intensification of the water cycle leads to increased salinity contrasts in the ocean, both within and between basins. Regional projections for several areas important to large-scale ocean circulation are presented, including the export of atmospheric moisture across the tropical Americas from Atlantic to Pacific, the freshwater gain of high latitude deep water formation sites, and the basin averaged evaporation minus precipitation with implications for interbasin mass transports.

2.2 Introduction

The movement of water between oceanic, atmospheric, and land reservoirs is a complex component of earth's climate collectively referred to as the "water cycle". These flows move not only water, but also heat throughout the climate system. While it is the small fraction of evaporation and precipitation that occurs over land which directly impacts human populations and industries, observational estimates indicate that 85% of the global evaporation and 77% of precipitation occur over the ocean (Durack, 2015; Schanze et al., 2010; Trenberth et al., 2007). This net evaporation over the oceans is crucial for driving the relatively small amount of precipitation over land (Gimeno et al., 2010, 2011; Ent and Savenije, 2013), and as such a full understanding of the water cycle requires a global perspective. Patterns of evaporation minus precipitation ($E-P$) also have cascading impacts on oceanic circulations via buoyancy and mass forcing, and on atmospheric circulation through latent heat release and cloud feedbacks (Allan, 2012).

The starting point for relating changes in global temperature to the water cycle is the increased mobility of water molecules at higher temperatures. According to the Clausius-Clapeyron (CC) relation for the saturation vapor pressure e_s of water (Held and Soden, 2006):

$$\frac{d\ ln(e_s)}{dT_s} = \frac{L_v}{RT_s^2} \approx 0.07\,\mathrm{K}^{-1} \tag{2.1}$$

So that water vapor content in the atmosphere increases by 7% per degree of warming at constant relative humidity for Earth's current mean temperature. $L_v = 2.5 \times 10^6\,\mathrm{J\,kg^{-1}}$) is the latent heat of vaporization, $R = 461\,\mathrm{J\,K^{-1}\,kg^{-1}}$ is the gas constant, and T_s is the near-surface air temperature. Current global climate models (GCMs) obey CC scaling quite closely for the increase in global atmospheric moisture W (Held and Soden, 2006; Allan et al., 2014).

The water cycle is made up of all transports and fluxes of freshwater, and therefore "intensification" of the water cycle is generally used to describe, in addition to globally increased W, an increase in total precipitation and evaporation, amplification of the existing $E-P$ pattern, and enhanced atmospheric vapor transport ($\mathbf{Q}$). There is robust theoretical (Chou and Neelin, 2004; Muller and O'Gorman, 2011), model (Held and Soden, 2006; Chou et al., 2009), and even emerging observational (Huntington, 2006; Durack et al., 2012) evi-

dence that the water cycle will intensify in the aforementioned ways in a warming climate. However, the strength of the water cycle is governed by more complex processes than CC scaling. While there is a positive correlation between global temperature and precipitation, the sensitivity is thought to be less than CC (Stephens and Ellis, 2008) due to energetic constraints governing tropospheric radiative cooling (O'Gorman et al., 2012; Allan et al., 2014). Analyses from the Coupled Model Intercomparison Project (CMIP) Phase 2 (Allen and Ingram, 2002), Phase 3 (Held and Soden, 2006), and Phase 5 (Allan et al., 2014; Hegerl et al., 2014) have shown the increase in global precipitation to be 2-3% K^{-1} with significant model scatter.

Detecting changes in the water cycle via observations of $E - P$ has proved challenging, as the small net flux is a difference between large and uncertain quantities (Huntington, 2006; Schmitt, 2008; Schanze et al., 2010; Josey et al., 2013). It has been suggested that a more reliable indicator of the water cycle is sea surface salinity (SSS), which is sensitive to changes in the surface fluxes. Evidence from 50 years of SSS observations combined with CMIP3 scaling by Durack et al. (2012) suggests that the sensitivity of SSS could be much higher than CC and also more than predicted by climate models, as much as 16 % K^{-1}. Ocean mixing and advection work to smooth out the spatial and temporal variability of surface water fluxes, and hence SSS is also an effective integrator of long-term changes in the water cycle (Durack et al., 2012). Analysis of observational data has already revealed robust trends in global salinity in line with projections of anthropogenic climate change (Boyer et al., 2005; Stott et al., 2008; Durack and Wijffels, 2010; Durack et al., 2012; Terray et al., 2011; Pierce et al., 2012). Preexisting interbasin salinity contrasts are driven by net imbalances in $E - P$ (Stommel, 1980; Zhou et al., 2000), and so intensification of the water cycle tends to increase these basin contrasts.

Given the complexity of the water cycle, inherent coupling between oceanic and atmospheric processes, and sparseness of oceanic observations, GCMs are a useful tool for predictive study of the water cycle. Current generation GCMs used in CMIP5 (Taylor et al., 2011) are generally effective at replicating global patterns of $E - P$ and atmospheric and oceanic transports of water. Liepert and Lo (2013) found that with several exceptions, CMIP5 models maintain a balanced atmospheric water cycle without long-term drift in global water content.

Several caveats should be noted regarding the representation of the water cycle in GCMs.

First, while model resolution has improved in recent generations, current grid sizes still require significant topographical smoothing. Therefore, steep mountain ranges such as the Andes are represented with reduced peak heights, and narrow oceanic through-flows like the Bering Strait and Strait of Gibraltar have greatly simplified geometry. A modeling study by Schmittner et al. (2010) demonstrated that alterations to global topography can substantially change water vapor fluxes, ocean circulation, and the climate system as a whole. The highest South American peak in models presented here ranges from 3916 to 4591 m, while the Andes reach an actual height of 6962 m. This discrepancy may result in excess moisture transport across ranges such as the Andes, as discussed by Richter and Xie (2010). To combat these problems, modelers sometimes enhance orography at the expense of increasing the mean height of continents, resulting in a dry bias of atmospheric vapor content over land (Gaffen et al., 1997). In general however, GCMs display a slightly overactive water cycle, with greater total precipitation and greater rainfall frequency than observations (Stephens et al., 2010; Tian et al., 2013; Demory et al., 2014).

Nearly all current GCMs have well documented issues with simulating tropical precipitation dynamics, particularly in the Pacific (Lin, 2007; Pincus et al., 2008; Collins et al., 2011; Brown et al., 2013; Flato et al., 2014; Li and Xie, 2013). A set of connected biases combine to produce an excessive cold tongue in the eastern Pacific, overly strong low-level trade winds, and an unrealistic double ITCZ flanking the equatorial Pacific (Lin, 2007; Hwang and Frierson, 2013).

While all GCMs solve water conservation equations and should ultimately produce an internally balanced water cycle, some CMIP3 and CMIP5 models display constant atmospheric moisture content despite having globally unbalanced evaporation and precipitation, suggesting an unphysical "ghost" source or sink of atmospheric moisture (Liepert and Previdi, 2012; Liepert and Lo, 2013). The ocean component of GCMs can also produce unrealistic freshwater balances, evidenced by a drift in global mean salinity (Durack et al., 2014). Therefore, water cycle consistency checks are important when analyzing GCM data.

2.3 Theory and Methods

2.3.1 Atmosphere

In a steady-state atmosphere, the vertically integrated water vapor budget can be written as a simple balance between horizontal transport divergence and the surface flux $E - P$ following (following Peixóto and Oort, 1983; Zaucker and Broecker, 1992; Cohen et al., 2000; Sohn et al., 2004; Richter and Xie, 2010):

$$\nabla \cdot \mathbf{Q} = E - P \tag{2.2}$$

$\mathbf{Q}$ is the vertically integrated horizontal water vapor transport, given by:

$$\mathbf{Q} = \frac{1}{g} \int_{surface}^{top} q\mathbf{v} \; dp \tag{2.3}$$

and q is the specific humidity, $\mathbf{v}$ the horizontal wind vector, p is pressure, and g the gravitational constant.

Over any area, water gained or lost by $E - P$ must equal the transport through the boundaries:

$$\oint (\mathbf{Q} \cdot \hat{\mathbf{n}}) \; dl = \oiint E - P \; dA \tag{2.4}$$

where dl is a line segment along the boundary, and dA is an element of surface area within the boundary. $\mathbf{Q}$ can be separated into mean and eddy components via Reynolds decomposition:

$$\mathbf{Q} = \overline{\mathbf{Q}} + \mathbf{Q}' \tag{2.5}$$

For the zonal transport, particularly in the tropics where winds are steadiest, $\mathbf{Q}'$ is small (Wang et al., 2012). However in the meridional flux, $\mathbf{Q}'$ and $\overline{\mathbf{Q}}$ are of similar magnitude. To fully capture the meridional transport then, the data used for this calculation must be sampled at higher resolution than typical time-scales of synoptic weather systems. In this study, 6-hourly model outputs have been used.

2.3.2 Ocean

In the ocean, any imbalance in the surface fluxes (evaporation, precipitation, runoff, and sea ice processes) induces a barotropic flow known as the Goldsbrough circulation (Goldsbrough, 1933; Huang and Schmitt, 1993; Huang, 2005). These circulations sometimes oppose the wind driven gyres, such as in the North Atlantic, where net evaporation drives a northward interior flow and a southward western boundary current (Huang and Schmitt, 1993). Applying steady state mass conservation (Wijffels et al., 1992; Stammer et al., 2003; Talley, 2008; Large and Yeager, 2009; Schanze et al., 2010):

$$\nabla \cdot \rho \mathbf{v} = E - P - R \tag{2.6}$$

and integrating through successive zonal sections, we can obtain the meridional transport in each basin dictated by the surface fluxes to within an integration constant T_b:

$$\iint E - P - R \; dx \; dy = \iint \rho \mathbf{v} \; dx \; dz + T_b \tag{2.7}$$

Where R is runoff and T_b is the interbasin transport, applied at the meridional boundaries of each basin. As discussed by Wijffels et al. (1992), the Bering Strait (BS) is a particularly useful point of reference, as flows within the Pacific and Atlantic are zonally bounded from this point until they reach the Pacific Indonesian Throughflow (PIT) and Southern Ocean. For ease of comparison to previous observational estimates (Wijffels et al., 1992; Schanze et al., 2010), the BS transport has been used along with the net $E - P - R$ over the Arctic to impose integration constants for the Atlantic and Pacific, and the effect of the PIT has been neglected.

In steady state, the global net precipitation over land exactly equals the runoff into the ocean. Therefore, a closed budget can be derived for the ocean climatology using only $E - P$ data, but the precise location of runoff sources will not be correctly represented, shifting the meridional transport curve (Dai and Trenberth, 2002). A calculation which utilizes river and ice fluxes gives the most accurate representation of ocean freshwater transports. In the meridional integrations presented here the wfo (water flux into ocean) model output has been used, which combines all freshwater fluxes into a single field on the native ocean grid.

2.3.3 Latent Heat Transport

Due to water's high latent heat of vaporization, the water cycle carries a significant amount of the poleward heat flux. The latent heat flux is usually calculated from the atmospheric moisture transport (Huang, 2005):

$$H_L = L_v * \mathbf{Q} \tag{2.8}$$

Where $\mathbf{Q}$ is a mass flux ($\mathrm{kg\,s^{-1}}$) of freshwater. The resulting heat flux associated with the meridional vapor transport is as large as 2.5 PW near 45°S or about half of the total energy transport there (Trenberth and Caron, 2001; Huang, 2005, also see Fig. 2-8). While this flux is often attributed to the atmospheric moisture transport, it is really a product of the coupled ocean-atmosphere water cycle, as the ocean must carry the compensating return flow of liquid water. Therefore, while the ocean mass transports induced by the surface flux $E - P - R$ are an order of magnitude smaller than the wind driven circulation, they are of great interest to the global energy budget.

2.3.4 Models and Calculation Specifics

For the projections presented here, all CMIP5 models available on a local server (Table 2.1) were used for global projections of temperature, vertically integrated water vapor, evaporation, precipitation, and ocean salinity using monthly means (Figs. 2-1, 2-2, 2-3, 2-4). A total of 6 models have been used for the atmospheric and oceanic budget and transport calculations (Figs. 2-7, 2-8, 2-9). The limited number of models utilized in the transport calculations is due to the large volume of data required when processing 6-hourly fields, which is necessary to adequately capture the eddy transports in the atmosphere (see Fig. 2-6). Only models found by Liepert and Lo (2013) to have realistically balanced water cycles were selected for the budget and transport calculations. Models with a range of horizontal grid sizes were intentionally chosen to explore the effect of topographical smoothing on the atmospheric transport. All multi-model means (MMM) use a single ensemble run (r1i1p1) from each model.

Ten year averages from the "Historical" (1990 to 2000) and "RCP8.5" (2090 to 2100) scenarios were processed to quantify centennial-scale changes in the water cycle under global warming. All projections described in the results section are taken to be MMM changes be-

tween these two time periods. RCP8.5 (Representative Concentration Pathway 8.5 $\mathrm{W\,m^{-2}}$) is a high emissions scenario intended to produce an additional radiative forcing of 8.5 $\mathrm{W\,m^{-2}}$ by the year 2100, although the effective forcing varies between models and was found by Forster et al. (2013) to be only 7.4 $\mathrm{W\,m^{-2}}$ in the MMM. RCP8.5 produces a rise in MMM surface air temperature of 4.0 °C for the 100 years analyzed. It is used here to represent the potential for changes in the water cycle but should not be interpreted as a quantitatively accurate forecast for the coming century. It should be noted that the CC scaling associated with this temperature rise would predict a 28% increase in surface specific humidity.

Additionally, a water budget has been calculated from state of the art observationally based products from the satellite era (1987-2014) as a comparison for the CMIP5 Historical simulations. The atmospheric moisture transport $\mathbf{Q}$ was calculated from ERA-Interim (Dee et al., 2011) reanalysis output, and the estimate of surface flux into the ocean $E - P - R$ was compiled from GPCP precipitation (Adler et al., 2003), OAFlux evaporation (Yu and Weller, 2007), and runoff estimates from Dai and Trenberth (2002) (see Schanze et al., 2010, for selection reasoning). This $E - P - R$ estimate for the ocean gives total $P = 12.6$ Sv, $E = 13.1$ Sv, and $R = 1.25$ Sv, with an imbalance of only 0.13 Sv (1 Sv = $1 \times 10^6\,\mathrm{m^3\,s^{-1}}$).

The $\mathbf{Q}$ calculation was performed using model outputs at 6-hourly time steps for wind and humidity, in order to fully capture the eddy transport. The outputs were processed in the native hybrid-sigma pressure coordinate, which conforms to topography at low altitudes. The horizontal output was interpolated onto a standardized $1^\circ \times 1^\circ$ grid for each model. ERA-I offers a direct monthly output of $\mathbf{Q}$.

Ocean freshwater fluxes for the meridional integration were taken from the combined $E - P - R$ flux into the ocean of each model and first integrated on the native ocean grid, in order to avoid introducing interpolation errors at point source river mouths.

2.4 Results and Projections

RCP8.5 produces a rise in global mean surface air temperature of 4.0 °C and an increase in atmospheric water content W of 32%, vs. the predicted 28% for CC scaling (Fig. 2-1). Model projections for $E - P$ are presented in Fig. 2-2. Total global evaporation (equal to global precipitation) increases from 17.3 Sv to 18.6 Sv in the multi-model 100-year projection, an 8% increase, or about $2\,\%\,\mathrm{K^{-1}}$. Best observational estimates based on satellite data

from GPCP (Trenberth et al., 2007) find global precipitation to be 15.4 Sv. The net water transport from ocean to land ($E - P$ over land, equivalent to R) increases by 12% from 1.17 Sv to 1.31 Sv. Total precipitation increases by 10% over land and just 6% over the ocean. A greater acceleration of the water cycle over land is expected due to slow thermal adjustment of the oceans (Dommenget, 2009) and subsequently greater warming over land in the 100-year period analyzed here.

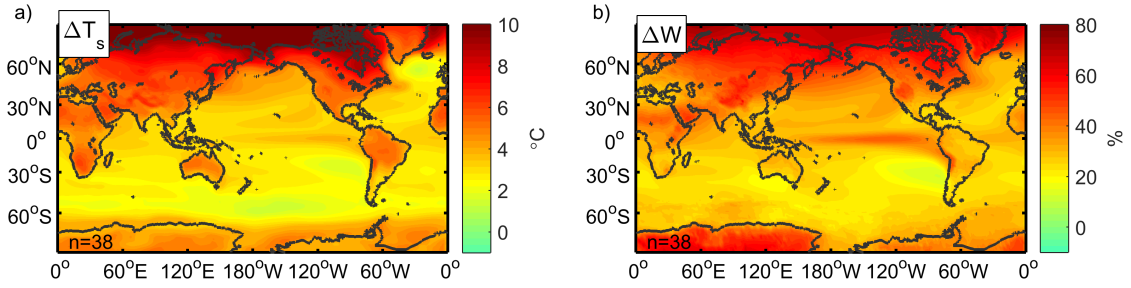

Figure 2-1: 100-year projection (RCP8.5 2090 to 2100 minus Historical 1990 to 2000) for (a) change in surface air temperature T_s and (b) percent increase in vertically integrated water vapor content W. Global average temperature change is 4.0°C. The warming closely matches the increase in water vapor content, with a pattern correlation of 0.86. The projections are an average of the 38 models listed in Table 2.1.

While evaporation and precipitation both increase globally, planetary-scale patterns of $E - P$ also show coherent changes. There is high model agreement (>90%) that ocean locations poleward of 45°N and 45°S will experience increased precipitation. The five subtropical ocean gyres display a decrease in precipitation albeit with weaker model agreement. There is high agreement for an increase in evaporation over almost areas of the ocean except the Southern Ocean and the subpolar North Atlantic, both of which show reduced warming relative to the global mean. Projections for land areas show a modest increase in net precipitation but with poor model agreement. The model average net precipitation increases significantly in the tropical rain belt of the Pacific and Indian Oceans but with large uncertainty among models. The increase in ITCZ precipitation is concentrated along the equator, due to a tightening of the ascending branch associated with cloud feedbacks (Su et al., 2017). Integrated over each basin, the Atlantic becomes 0.20 Sv more evaporative, the Pacific 0.16 Sv more precipitative, the Indian 0.08 Sv more evaporative, and the Arctic 0.05 Sv more precipitative.

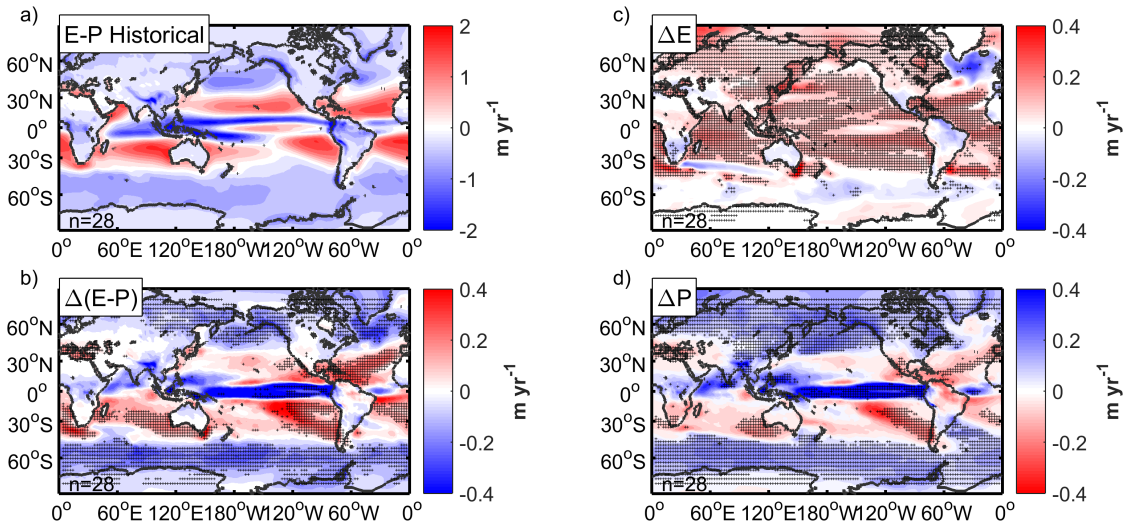

Figure 2-2: (a) $E - P$ ($\mathrm{m\,yr^{-1}}$) for the Historical period (1990 to 2000). (b-d) 100-year projection for change in $E - P$, P, and E ($\mathrm{m\,yr^{-1}}$), using RCP8.5 (2090 to 2100) and Historical (1990 to 2000) simulations. Areas with greater than 90% model agreement in the sign of the change are stippled. All panels are an average of the 28 models listed in Table 2.1.

SSS is primarily forced by the surface flux $E - P - R$, and hence would be expected to display similar changes. The meridional patterns of increased subtropical evaporation and increased tropical and high latitude precipitation are evident in the SSS projection presented in Fig. 2-3, but are dwarfed by a large zonal contrast between the subtropical Atlantic and Pacific. With the exception of modest salinification in the southern subtropical Pacific, all other areas of the Pacific display surface freshening. The weak signature in the northern subtropical Pacific may partly be a function of weakened trade winds and evaporation (Laîné et al., 2014), as well as advection of freshened water from the equatorial Pacific. In the Atlantic, all subtropical regions show surface salinification, as high as 0.8 psu. These basin trends are particularly clear in the zonal average (Fig. 2-4). When compared to a pure amplification of the existing pattern, the Pacific becomes fresher and the Atlantic saltier, at least between the latitudes of 40° N/S.

Following Durack et al. (2012), a MMM linear regression of zonal mean SSS change onto its modeled historical values gives a pattern amplification of $5.9\,\%\,\mathrm{K^{-1}}$, slightly lower than the values for CMIP3. The same calculation for $E - P$ gives a pattern amplification of $5.2\,\%\,\mathrm{K^{-1}}$, in line with previous values (Durack et al., 2012). The SSS regression is particularly sensitive to the use of individual model climatologies vs. MMM climatology, as performing the regression on the MMM smooths out covariances and gives only $3.1\,\%\,\mathrm{K^{-1}}$.

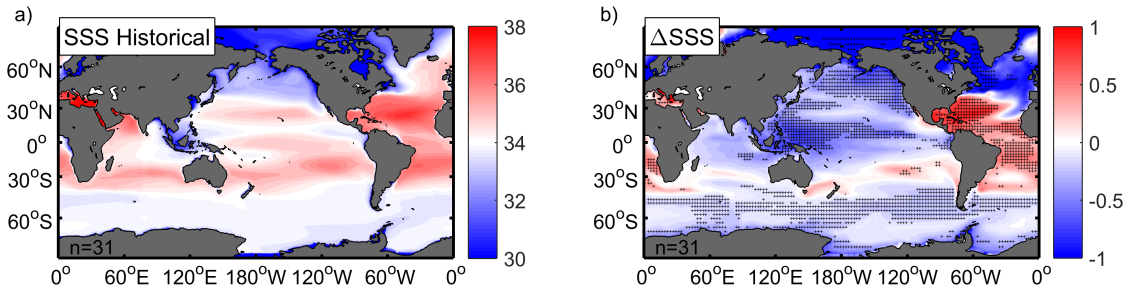

Figure 2-3: (a) Multi-model mean climatology for SSS. (b) Projection for 100-year change in sea surface salinity, using RCP8.5 (2090 to 2100) and Historical (1990 to 2000) simulations. Salinities are given in PSS-78 equivalent. Areas where more than 90% of models agree on the sign of the change are stippled. Both panels are an average of the 31 models listed in Table 2.1.

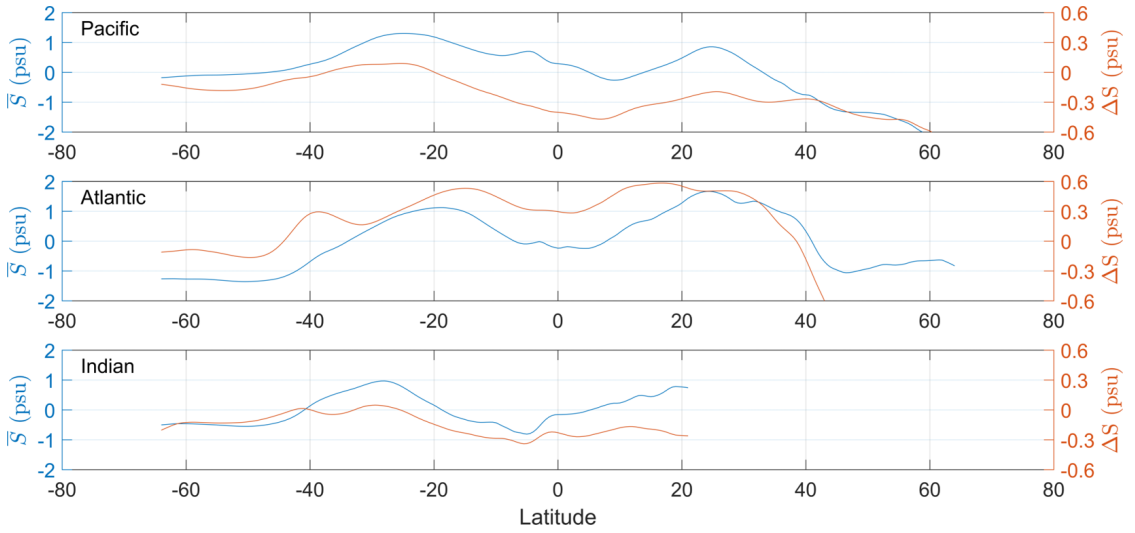

Figure 2-4: Zonal averages separated by basin of the historical mean salinity ($\overline{S}$) and the RCP8.5 salinity change ΔS. Between the latitudes of 40° N/S, the Pacific becomes fresher than a pure amplification of the existing pattern, and the Atlantic saltier.

While the projected $E - P$ changes do not at first glance display the zonal asymmetry described above, salinity is an effective spatial integrator of surface forcing as ocean currents and mixing tend to smear out smaller scale variability. It is therefore useful to assume a basin-wide perspective of the atmospheric transports and their associated freshwater fluxes into and out of the oceans. Fig. 2-5 summarizes this perspective, with drainage basins defined by topographical maxima. Low and high latitude basins are also divided at 30°N and 30°S. The transport from tropical Atlantic to Pacific has been broken into three components: South America (30°S to 8°N), Central America (8°N to 20°N), and Mexico (20°N to 30°N).

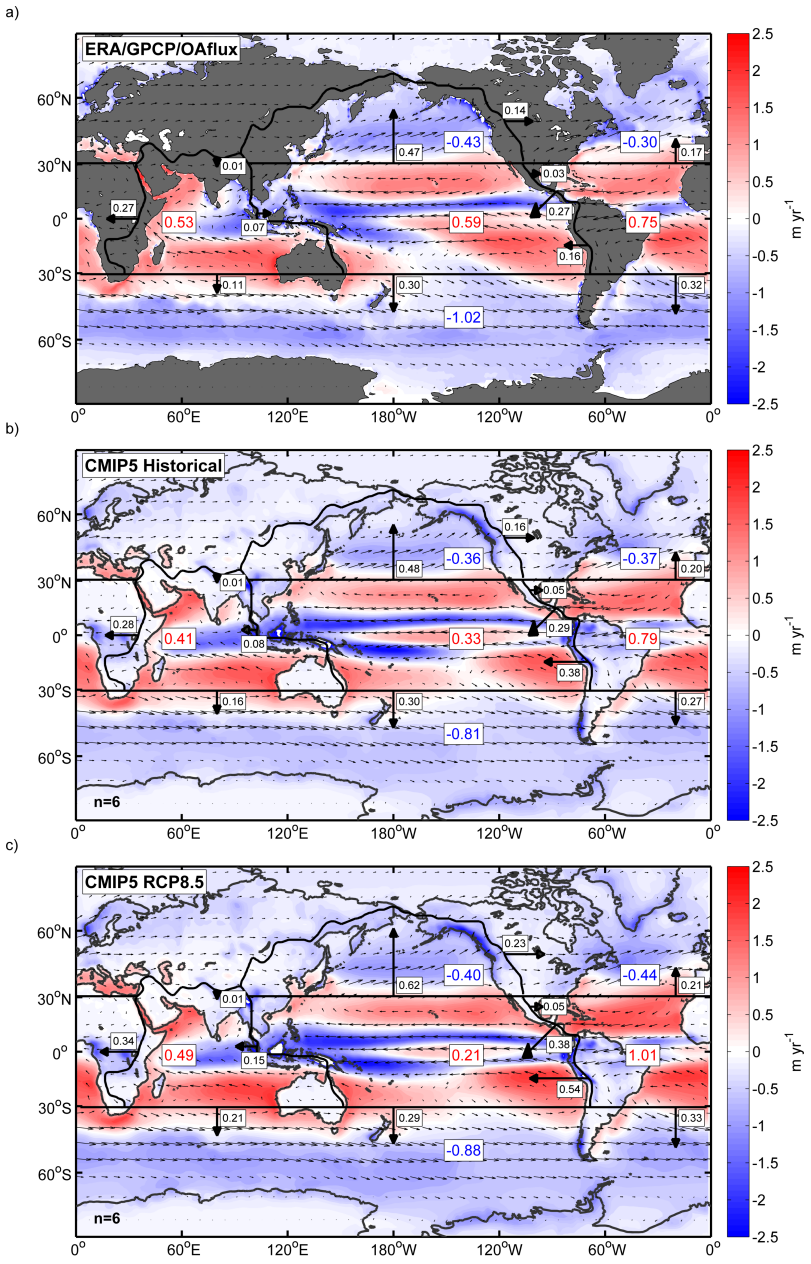

Figure 2-5: Summary of the atmospheric freshwater budget showing $\mathbf{Q}$ and $E - P$ for (a) ERA-I winds and humidity with GPCP/OAFlux fluxes 1979 to 2014, and multi-model means of the CIMP5 Historical 1990 to 2000 (b) and RCP8.5 2090 to 2100 (c) simulations. For the observational data set, $E - P - R$ into the ocean has been used rather than $E - P$ over combined land and ocean areas. The map has been divided (thick black lines) by topographical drainage basins between the Atlantic, Pacific, and Indian oceans, and into low and high latitude regions separated at 30°N/S, corresponding to the descending branches of the Hadley cells. Colored values are $E - P$ integrated over each region, with red indicating net evaporation and blue net precipitation (Sv). Filled contours are the global $E - P$ ($\mathrm{m\,yr^{-1}}$). Small arrows indicate the vertically integrated atmospheric moisture flux, and bold arrows show the fluxes across drainage divides in Sv. The CMIP5 transports are an average of the 6 models listed in Table 2.1.

The atmospheric water budget produced by the CMIP5 Historical simulations (Fig. 2-5b) shows many similarities to the observational estimate (Fig. 2-5a). Both capture the export of water vapor from low to high latitudes, zonal convergence in the Pacific and divergence in the Atlantic and Indian. The models and observations produce the opposite sign for the small net flux across the Maritime Continent. The largest discrepancies seen in the fluxes are across South America, with the CMIP5 models producing a much higher transport estimate there. There is also a significant discrepancy in the GPCP/OAFlux and ERA-I budget for the low-latitude Pacific with a residual of 0.28 Sv, making this region poorly constrained for comparison with models. An imbalance of 0.27 Sv is also present in the Southern Ocean region. There are small imbalances between the CMIP5 divergences and surface fluxes as well, but all are less than 0.1 Sv. These model imbalances are likely related to the regridding scheme used here, or the relatively short 10 year integration which may allow some reservoir storage.

The RCP8.5 projection for basin to basin transports reveals the larger scale pattern which explains the zonal SSS trend in Fig. 2-3. Relative to the historical scenario, RCP8.5 shows an increased westward transport by the trade winds at low latitudes, and an increased poleward transport from low to high latitudes which is driven primarily by the synoptic eddy field (Fig. 2-6). Although the zonal transport across all low-latitude divides increases, the preexisting differences in magnitude are amplified by such a pattern. Therefore the net evaporation in the low-latitudes gets larger in the Atlantic and smaller in the Pacific. Additionally, there is an increase in net precipitation for all extratropical regions.

Among the 6 models analyzed here, there is 100% agreement for the sign of the change in net $E-P-R$ for all basins except the tropical Indian Ocean (5/6 in agreement). There is similarly robust agreement for the changes in atmospheric transport across drainage divides, with most segments displaying 100% agreement in the sign of the change. The components with some model disagreement are the northward export out of the tropical Atlantic (4/6 in agreement), the southward export out of the tropical Pacific (4/6 in agreement), the tropical Pacific to tropical Indian (5/6 in agreement), and the transport from the Indian Ocean to Eurasia (3/6 in agreement).

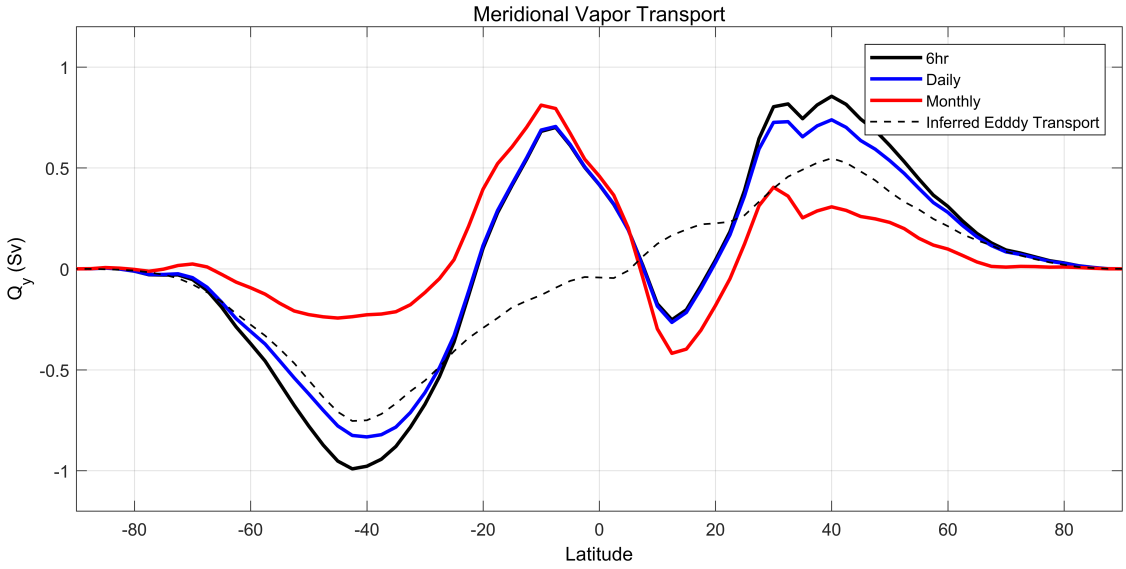

Figure 2-6: Zonally integrated meridional freshwater transport (Sv) in the atmosphere calculated using the integral in Eq. 2.3 from monthly (red), daily (blue), and 6-hourly (black) humidity and wind data, taken from the historical period of the GFDL-CM3 model. The inferred eddy transport (dashed) is taken to be the 6-hourly minus the monthly. In the mid-latitudes, synoptic eddy fluxes dominate the total, while the tropical transport is primarily accomplished through laminar flows, and the eddy transport slightly counteracts the equatorward flux.

The MMM of zonally averaged transports (Fig. 2-7) shows an increase in atmospheric freshwater fluxes everywhere. The inter-model spread is displayed for an idea of the model uncertainty in moisture transports. The change in the zonally integrated meridional transport (Fig. 2-8) is as large as 0.3 Sv near 10°S and 40°S which corresponds to nearly 0.7 PW of additional latent heat transport. The meridional ocean transports separated into basins (Fig. 2-9) show generally weaker southward transport through the Atlantic and weaker northward transport through the Pacific. All transport curves match qualitatively with the observational comparison.

2.5 Discussion

2.5.1 Zonal Atmospheric Transports

To first order, **Q** scales similarly to CC, which would be the expectation if warming caused no dynamical response in the circulation (Held and Soden, 2006). The global mean zonal transport Q_x increases 35%, and the meridional transport Q_y increases 30%, noting again that the increase in W is 32%. A robust consequence of this thermodynamic scaling is that

regional patterns of moisture convergence and divergence are amplified in a warming climate even without circulation changes. The pre-existing zonal pattern in the subtropics is a useful example. There is a large moisture transport across Central and South America relative to the transport across Africa and the Maritime Continent. If the increase in temperature and thus specific humidity is uniform, then a constant fractional increase of each interbasin transport causes an increased volume convergence in the Pacific.

A slight increase in the strength of the trades over South America causes the change in $\mathbf{Q}$ to be higher than CC scaling. Conversely, a slight decrease in the trades across Africa gives a lower scaling there. In the models analyzed here, there is not a significant correlation between horizontal resolution and transport over the Andes, although all display much greater transports than the ERA-I Reanalysis value of 0.16 Sv. Other reanalysis products show greater Andean transports closer to the CMIP5 values (Richter and Xie, 2010), particularly along the northern segment, so it is unclear how topographical smoothing affects this transport. Xu et al. (2005) showed that in a high resolution model, transport across Central America was insensitive to the fine structure of the orography, as intense jets around mountains or diffuse flow over smooth topography produced nearly the same transport.

There are a number of dynamical factors affecting tropical transports in a warming climate, although circulation changes are generally small compared to thermal affects (Held and Soden, 2006). A common feature of GCM warming simulations is a decrease in the Walker circulation (Vecchi et al., 2006; DiNezio et al., 2013; Ma and Xie, 2012). This is sometimes explained using the differential response of atmospheric water vapor ($7\,\%\,\mathrm{K}^{-1}$) and precipitation (2-3 $\%\,\mathrm{K}^{-1}$) to warming. Because the convective supply of water cannot exceed the loss of water from precipitation, the balance equations require a weakening of the upward mass flux and therefore the overturning circulation (Held and Soden, 2006; Ma et al., 2011). However, observational evidence for changes in the Walker circulation is inconclusive (Tokinaga et al., 2012).

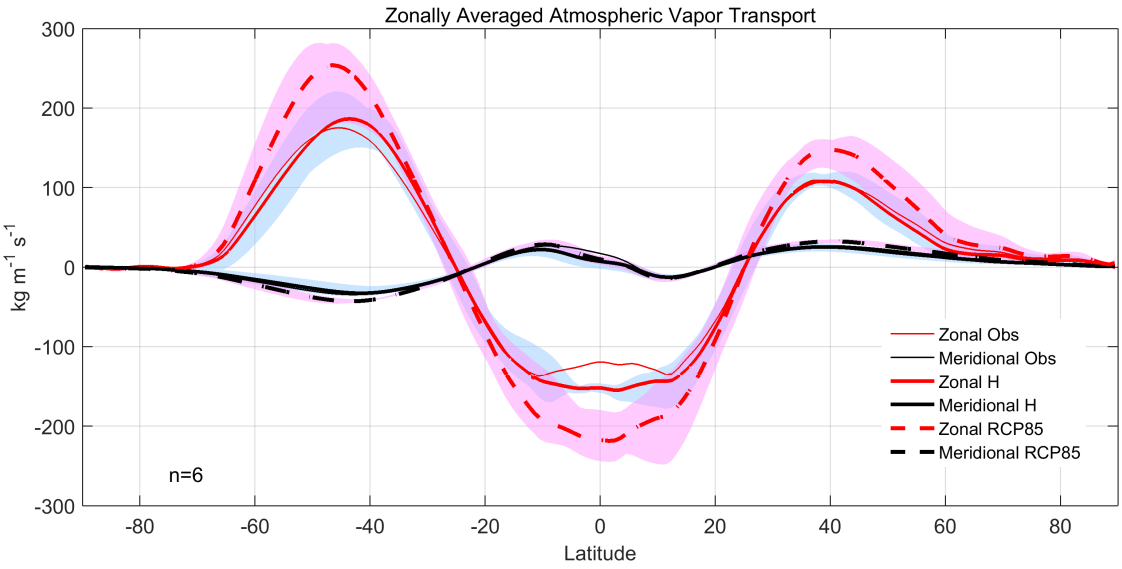

Figure 2-7: Zonally averaged meridional and zonal atmospheric vapor transport, for ERA-I reanalysis (thin solid), Historical (solid), and RCP8.5 (dashed) simulations. The transports are expressed as a flux density per meter of latitude with units of $\mathrm{kg\,m^{-1}\,s^{-1}}$. The zonal transports are an order of magnitude larger than the meridional ones. The CMIP5 transports are an average of the 6 models listed in Table 2.1.

Regional patterns of sea surface temperature (SST) increase may also play a role (Knutson and Manabe, 1995; Tokinaga et al., 2012). In the tropics, a distinct El Nino like warming mode is produced by CMIP5 models which can be seen in Fig. 2-1a (also see Cai et al., 2014). Warm SST in the eastern tropical Pacific induces anomalous low pressure there, and an increase in trade wind strength across South America follows.

The change in $\mathbf{Q}$ across the Maritime Continent (88%) is large in a relative sense, but remains small in terms of volume flux because the net transport of the seasonal monsoonal cycle is small. One argument regarding the monsoon circulation of the Indian basin predicts an increase in summer monsoon intensity due to the transient increase in land-sea temperature contrast under warming (Turner and Annamalai, 2012; Lee and Wang, 2014). Such an increase would bring additional moisture from the Pacific to the Indian during summer, but monsoon projections have large inter-model spread. The change in $\mathbf{Q}$ is also large (44%) for the extratropical transport across North America from Pacific to Atlantic, dominated by anomalous northeasterly transport over Alaska, but this is primarily a function of amplified Arctic warming and therefore larger CC scaling.

Based on these trends in interbasin transport, a general enhancement of the zonal pattern of $E - P$ and SSS is projected under anthropogenic warming. The Atlantic becomes more

evaporative and saline, while the Pacific becomes more precipitative and fresher. These trends will lead to halosteric effects on sea level, diminishing sea level rise in the Atlantic while enhancing it in the Pacific (Durack et al., 2014). Despite an increase in net evaporation over the Indian Ocean, a slight freshening is projected for all but the most western portions of the basin. This is consistent with the substantial advection of Pacific water westward through the PIT, water which is projected to freshen due to increased precipitation in the equatorial Pacific.

Increased moisture export from Atlantic to Pacific and subsequent salinification of Atlantic surface waters has previously been discussed as a positive feedback on North Atlantic Deep Water (NADW) formation and the meridional overturning circulation (Broecker et al., 1990; Zaucker et al., 1994; Lohmann, 2003; Richter and Xie, 2010). Increased freshening and warming of the northern Atlantic and Arctic surface water tends to increase static stability of the water column and decrease deep convection (Aagaard and Carmack, 1989; Hasumi, 2002; Hu and Buyanovsky, 2003). However, these simulations also confirm that warming increases surface salinities in the subtropical Atlantic, which could counteract the positive buoyancy forcing from increased freshwater input at higher latitudes.

2.5.2 Meridional Atmospheric Transports

The projected increase in meridional transport across 30°N and 30°S is somewhat less than CC scaling, and also shows large zonal variation. The synoptic eddy field plays a much greater role in determining meridional fluxes compared to zonal, and so the meridional transports may be more subject to dynamical changes and less directly tied to CC scaling. Poleward transport out of the north Pacific increases by 31%, while transport out of the North Atlantic shows nearly no change, as increases in W are offset by a weakening of the prevailing southwesterly transport there. In the Southern Hemisphere, the poleward transport out of the Atlantic and Indian are near CC scaling. Transport out of the South Pacific, however, shows almost no change. Here CC is counteracted by an equatorward anomaly along South America. Transport from the Indian Ocean to Eurasia is negligible in CMIP5 models.

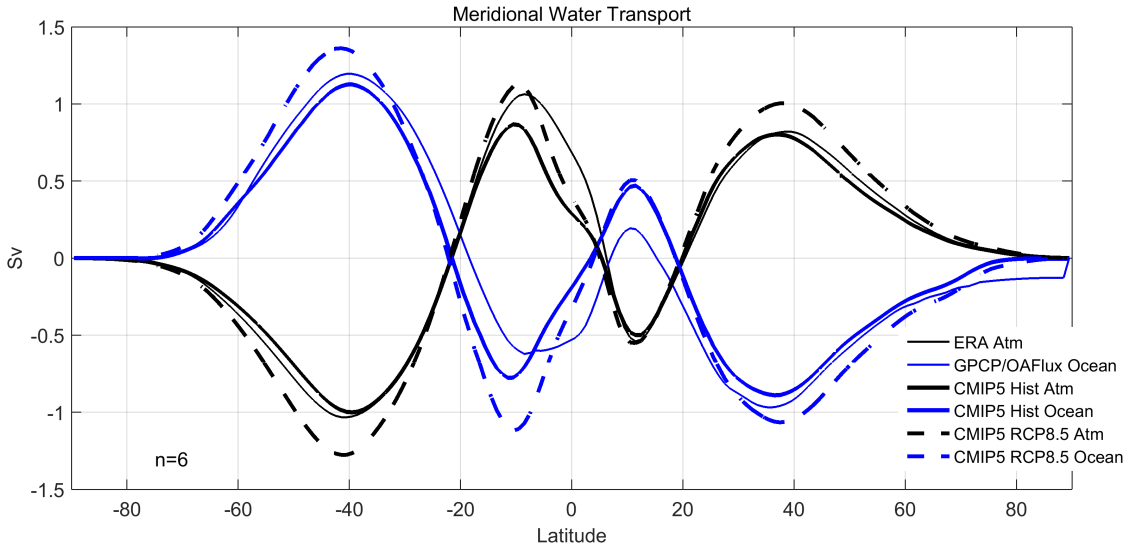

Figure 2-8: Zonally integrated meridional freshwater transport (Sv) in the atmosphere and the ocean, for observations (thin solid), Historical, (solid) and RCP8.5 (dashed) simulations. The atmospheric calculation uses the zonal integral of **Q** and the ocean curve is produced from the $E - P - R$ integral or wfo variable in CMIP5. The CMIP5 transports are an average of the 6 models listed in Table 1.

2.5.3 Ocean Throughflows and Transports

Bering Strait (BS) transport is understood to be a function of the sea surface height (SSH) gradient from Pacific to Atlantic, which some have suggested is maintained by atmospheric moisture export over Central and South America and associated $E - P$ fluxes (Latif et al., 2000; Schmitt, 2008). Despite projections for increasing disparity between Pacific and Atlantic $E - P$, the 6 models analyzed here show a decreasing BS flow, from 0.80 Sv to 0.68 Sv in the MMM, compared to observational estimates of 0.79 Sv (Schanze et al., 2010). While the Atlantic becomes more evaporative and would be expected to decrease in mean height from mass balance and halosteric effects, the Arctic experiences significant freshwater gain which increases SSH there. Wind stress has been used to explain seasonal variability in the BS transport (Coachman and Aagaard, 1988), as the mean wind field is southward and opposes the pressure driven ocean transport. Wind stress does not appear to explain the projections for BS transport here, as the change in mean wind is actually for weaker southerly circulation through the strait. A probable explanation for decreased BS flow is the thermosteric rise associated with amplified warming in the Arctic, reducing the more local Pacific to Arctic pressure gradient.

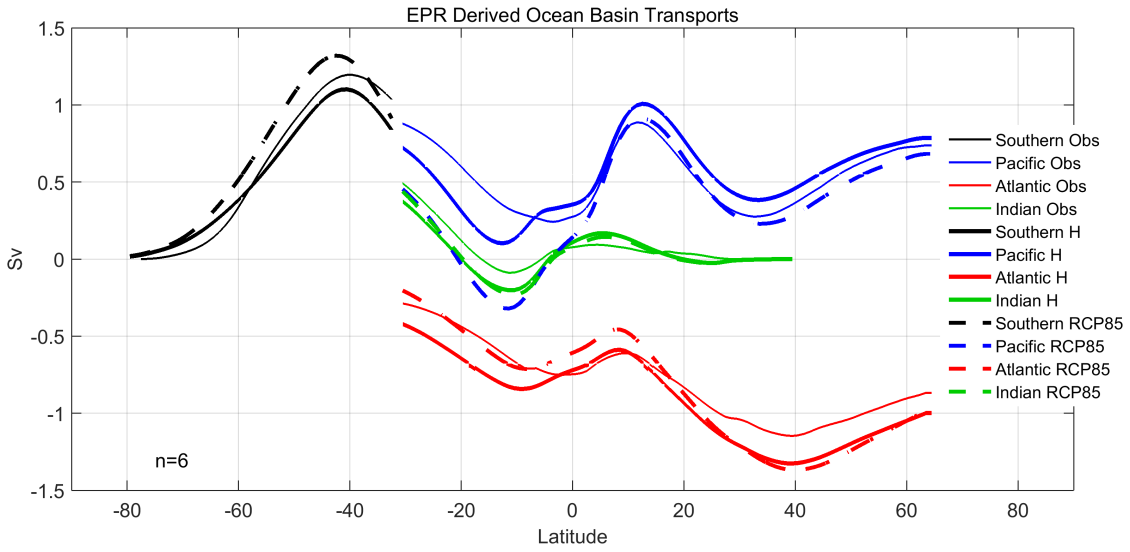

Figure 2-9: $E - P - R$ derived freshwater transports in each basin, using the Bering Strait flow as an integration constant for the Atlantic and Pacific. The observational curves are the integrated $E - P - R$ dataset, and the CMIP5 curves are an average of the wfo variable for the 6 models listed in Table 2.1. The net Arctic freshwater gain is added to the southward Atlantic flow at 65°N, 0.13 Sv for the observations, 0.20 Sv for the Historical simulation, and 0.29 Sv for RCP8.5.

Basin meridional transports for the historical simulations closely resemble those of observations (Baumgartner and Reichel, 1975; Wijffels et al., 1992; Dai and Trenberth, 2002; Schanze et al., 2010). The PIT transport has been neglected in Fig. 2-9 for simplicity, which induces a counterclockwise circulation around Australia (see Wijffels et al., 1992; Dai and Trenberth, 2002, for further discussion) and would significantly displace the Indian curve towards southward transport and the Pacific curve towards northward transport south of the PIT. The observational estimate presented here shows stronger northward transport in the Pacific and weaker southward transport in the Atlantic from approximately 10°N and all points southward relative to CMIP5. Due to the slight decrease in BS flow and increased precipitation in the tropical Pacific, the projected meridional flow in the Pacific becomes southward around the equator, unlike in the historical simulation which produces northward flow throughout the Pacific.

2.6 Conclusions

This chapter examines the estimated changes in the water cycle of relevance to ocean circulation from a multi-model ensemble of CMIP5 models for a high CO_2 emissions scenario

for the 21st century. Drainage basins are defined and net water fluxes calculated between them. There are large changes in interbasin transports and strengthening of the patterns of mid-latitude evaporation and high and low latitude precipitation. Substantial changes in ocean salinity are projected, with salty areas getting saltier and fresh areas fresher overall. Such changes have consequences for regional sea level rise and the strength of the meridional overturning circulation, and indicate the importance of sustained global salinity observations over the next century.

However, the spatial response of SSS and $E - P$ to warming in CMIP5 is far from identical. The ocean models of CMIP5 display significant mixing of anomalous freshwater signals between the tropics and subtropics, with a more isolated response in the subpolar regions. In particular, the North Atlantic subpolar gyre appears as a region with low model confidence in the salinity response. These results suggest that if the salinity field is to be used as a global "rain gauge" for the Earth's water cycle, the effects of ocean mixing and advection and large-scale interbasin patterns of moisture convergence must be considered in addition to the predicted amplification of the local surface forcing.

2.7 Chapter Acknowledgements

This research was supported by NASA grant: NNX12AF59GS03. The authors would like to thank all of the modeling groups involved in CMIP5, the World Climate Research Programme's Working Group on Coupled Modeling for coordinating the experiment, and those involved in the WHOI CMIP5 Community Storage Server supported by the Ocean Climate Change Institute. In addition, the creators of the observational datasets used here including the WHOI OAFlux Project, NASA GEWEX Global Precipitation Climatology Project, and the ECMWF ERA-Interim Reanalysis are acknowledged. Finally, the authors would like to thank two anonymous reviewers for their helpful comments.

2.8 Supplementary Material

Institute	Model	*tas*, *hus* (Fig. 2-1)	*so* (Fig. 2-3, 2-4)	*evspsbl*, *pr* (Fig. 2-2)	*ua*, *va*, *hus*, *evspsbl*, *pr* (Fig. 2-5), wfo (Fig. 2-7, 2-8, 2-9)
BCC	BCC-CSM1.1	x	x	x	
BCC	BCC-CSM1.1(m)	x	x		
BNU	BNU-ESM	x	x	x	
CCCMA	CanESM2	x	x	x	
CMCC	CMCC-CESM	x	x		
CMCC	CMCC-CM	x	x	x	
CMCC	CMCC-CMS	x	x		
CNRM-CERFACS	CNRM-CM5	x	x	x	
CSIRO-BOM	ACCESS1.0	x			
CSIRO-BOM	ACCESS1.3	x			
CSIRO-QCCCE	CSIRO-Mk3.6.0	x			
FIO	FIO-ESM	x	x		
ICHEC	EC-EARTH	x		x	
INM	INM-CM4	x	x	x	
IPSL	IPSL-CM5A-LR	x	x	x	x
IPSL	IPSL-CM5A-MR	x	x	x	x
IPSL	IPSL-CM5B-LR	x	x		
LASG-CESS	FGOALS-g2	x	x	x	
MIROC	MIROC-ESM	x	x	x	
MIROC	MIROC-ESM-CHEM	x	x	x	
MIROC	MIROC5	x	x	x	
MOHC	HadGEM2-CC	x	x	x	
MOHC	HadGEM2-ES	x	x	x	
MPI-M	MPI-ESM-LR	x	x	x	
MPI-M	MPI-ESM-MR	x	x	x	
MRI	MRI-CGCM3	x	x	x	x
NASA-GISS	GISS-E2-H	x	x	x	
NASA-GISS	GISS-E2-H-CC	x	x	x	
NASA-GISS	GISS-E2-R	x	x	x	
NASA-GISS	GISS-E2-R-CC	x	x	x	
NCAR	CCSM4	x		x	x
NCC	NorESM1-M	x	x	x	
NCC	NorESM1-ME	x	x	x	
NOAA-GFDL	GFDL-CM3	x	x	x	x
NOAA-GFDL	GFDL-ESM2G	x	x	x	
NOAA-GFDL	GFDL-ESM2M	x	x	x	
NSF-DOE-NCAR	CESM1(BGC)	x			
NSF-DOE-NCAR	CESM1(CAM5)	x			

Table 2.1: List of CMIP5 models used in Chapter 2 for the variables surface air temperature (*tas*), specific humidity (*hus*), salinity (*so*), evaporation (*evspsbl*), precipitation(*pr*), freshwater flux into the ocean (wfo), zonal wind (*ua*), and meridional wind (*va*). The models used in creating each figure are listed in the table. Further details for each model may be found in Flato et al. (2014).

THIS PAGE INTENTIONALLY LEFT BLANK

Chapter 3

Quasi-Steady-State Balances of Salinity and Temperature in the Global Ocean Mixed-Layer

3.1 Abstract

The mean fields of salinity (S) and temperature (T) in the upper ocean develop as a balance between forcing at the surface, which generates variance, and interior transports, which work to restore S and T towards homogeneity. Because the ocean is in constant motion, these tracer fields are influenced by non-local forcing and non-isotropic transports, meaning the steady-state fields do not perfectly match the pattern of surface forcing. Ocean transport is also key to understanding the response of S and T to forcing change, including that associated with climate change. A quantification of the steady-state S and T budgets in the surface mixed-layer (SML), calculated from both an ocean state estimate and directly from observations, is presented here. We use the budgets to contextualize coupled-model projections of salinity change, by analyzing the processes and pathways that are capable of transporting climate salinity anomalies within the ocean circulation. One hypothesis is that oceanic regions with strong lateral transports within the SML are likely to show the most influence from non-local forcing. The steady-state budgets suggest that lateral transport within the SML is dominant in the equatorial half of the subtropical gyres due to meridional Ekman and Sverdrup flows which transport waters across strong mean salinity gradients.

This argument is supported by CMIP5 simulations which show that changes in freshwater forcing are relatively well mixed within the subtropical gyres of each basin. In contrast, the subpolar gyres are dominated by vertical exchange with the thermocline below, and do not connect to the subtropical gyres via surface exchange. These distinctions have implications for the idea of an "ocean rain gauge".

3.2 Introduction

The time-averaged fields of salinity (S) and temperature (T) in the upper ocean are set by the exchange of freshwater and heat at the ocean surface, which act to generate variance, and interior transports in the ocean, which work to restore the tracer fields towards homogeneity (Schanze, 2013). In a relatively stable climate, these processes are quasi-balanced, and the mean salinity and temperature fields approach a steady state.

In a period of rapid climate change, the surface forcing of freshwater and heat is altered such that the tracer equations averaged over climate timescales are not balanced, leading to changes in temperature and salinity. Even without circulation changes, as the tracer fields begin to shift, ocean transports do as well by acting on altered gradients. If the climate stabilizes, then the surface forcing and ocean transports eventually come to a balanced state again.

If the ocean is not in a steady-state condition during a period of transient climate response, then how can a steady-state framework be used to understand the ocean's salinity response to climate change? While the salt budget is no longer balanced, even in a very strong forcing scenario the rates of salinity change in the ocean are a small residual (at least an order of magnitude smaller) in the annually-averaged budget when compared to surface fluxes and oceanic transports (i.e. Ponte and Vinogradova, 2016). The tendency is due to a small imbalance in the existing budget, but barring non-linear circulation changes, the oceanic transports of salt do not undergo $O(1)$ changes during the initial climate response. Therefore, a steady-state budget for the present-day climate continues to describe the primary balances found in the future climate for most regions. Therefore, we argue that the present-day steady-state budget is a useful tool for understanding the propagation of climate-induced anomalies through the ocean system.

Following this logic, here we analyze a steady-state salinity budget for the surface mixed-

layer (SML), in order to identify the dominant oceanic transport processes that maintain the surface salinity field. We use this information to infer major oceanic pathways for climate-induced salt anomalies, and hypothesize how these pathways may lead to dispersal of freshwater forcing anomalies into non-local regions of the ocean. In addition to the salt budget, we show results for a similar SML temperature budget in order to compare and contrast the dynamics of these two tracers.

The SML framework is chosen in this analysis because it is the part of the ocean that interacts directly with climate forcing, and where the strongest S and T changes develop. The SML is a ubiquitous layer of varying thickness found across the ocean surface. Wind driven mixing, and in some locations negative buoyancy fluxes, act to turbulently homogenize surface waters. A strong density gradient is found immediately below the SML, marking the transition into the ocean's thermocline. The SML provides a natural division in dynamics between the ocean's surface layer, which is in contact with the atmosphere, and the deeper stratified layers which are isolated from the atmosphere. A budget for a fixed-thickness layer which does not exceed the mixed-layer depth (MLD) is dominated by vertical mixing with the unstratified waters below, as seen in Ponte and Vinogradova (2016), while a fixed layer depth chosen to be below the SML blurs together the dynamics of these two dynamically distinct water masses.

There is a rich literature in using SML and other surface budgets to understand local salinity dynamics. Typically the budget has either been calculated at a single Eulerian point from mooring data (Cronin and McPhaden, 1998; Farrar et al., 2015), or for a generalized region using model output (Bryan and Bachman, 2014; Johnson et al., 2016; Qu et al., 2011; Busecke et al., 2017) or remote sensing observations (Johnson et al., 2002; Dong et al., 2009; Rao and Sivakumar, 2003; Busecke et al., 2014; Schmitt and Blair, 2015).

While these studies are useful for identifying local dynamics, addressing the salinity response to climate is a global problem and requires a broader perspective. A previous series of modeling studies (Ponte and Vinogradova, 2016; Vinogradova and Ponte, 2017) calculated a global salt budget using the Estimating the Circulation and Climate of the Ocean (ECCO) state estimate, but the analysis was focused on the upper 10 m surface layer of the model. This volume formulation is simple, but because the lower boundary is contained within the unstratified SML, the budget is dominated by the large turbulent vertical mixing term. Therefore, this budget formulation provides little information about

how surface freshwater fluxes are transported throughout the ocean beyond their initial homogenization within the SML.

Another effort to calculate a global surface salinity budget was carried out by Yu (2011) using a varying thickness SML framework and a combination of observational datasets. However, the observational terms analyzed in Yu (2011) only explain 40% of the global salinity variance, suggesting that there are $O(1)$ processes unresolved in the budget. Furthermore, this study analyzed seasonal anomaly generation rather than the steady-state balances which are necessary to understand the climate adjustment problem.

3.3 Data and Methods

To calculate a closed budget, we utilize the ECCO state estimate, which provides a data-assimilated estimate of ocean circulation which is fully conservative of mass and tracers. As a compliment to the ECCO-based budget, we also estimate the same terms using observational datasets, utilizing a mix of satellite and in-situ data. As the temporal and spatial resolution of existing observational datasets is only sufficient for resolving climatological fluxes, the budget terms based on transient eddy-like fluxes cannot be estimated accurately and it is not possible to derive a closed budget. However, the observational estimates serve as a comparative baseline for the closed ECCO budget, and the qualitative similarities between the two estimates add confidence to the results.

3.3.1 Observations

To develop a climatology of mixed-layer properties relevant to the calculation of temperature and salinity transports, a range of observational datasets are utilized, hereafter referred to as OBS. Individual profiles were extracted and analyzed from Argo floats and high-resolution shipboard conductivity temperature depth (CTD) casts archived in the World Ocean Database (WOD). Preexisting climatologies do not accurately represent the small vertical gradients within the mixed-layer that are important for calculating entrainment and vertical mixing terms, hence the need to construct an independent climatology based on properties calculated directly from profiles.

A total of 1,074,748 Argo profiles from the period 2000 to 2016, and 711,421 high-resolution WOD CTD casts from the period 1981 to 2016 were selected (see Fig. 3-1). Argo is

the primary contributor to open ocean coverage while shipboard profiles from WOD provide data on the continental shelves where Argo does not reach. The temporal inhomogeneity of the climatology is an acknowledged compromise to achieve increased spatial coverage. Quality control checks were used to remove profiles that did not sample the top 10 m or sufficiently deep to detect the mixed-layer base, and those containing large density overturns or contaminated near-surface salinity measurements. Profiles were also removed based on internal quality flags for Argo and WOD.

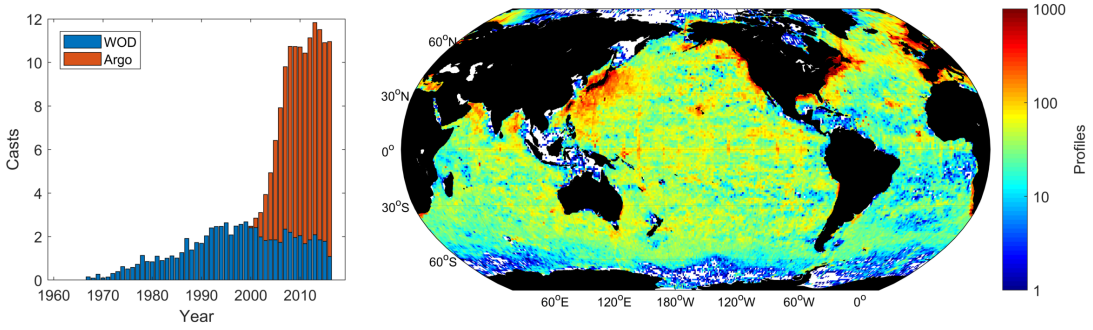

Figure 3-1: Spatial density of CTD and Argo casts used to develop the OBS climatology. The map (right) shows the number of casts per 1° grid cell over the period 1981 to 2016, plotted on a logarithmic color scale. WOD casts provide good spatial coverage over the continental shelves and at repeat transects while Argo profiles dominate in the open ocean. Histogram of casts over time (left), showing the increased data density of Argo beginning in the 2000's.

The full set of 1,786,169 profiles were processed for relevant mixed-layer properties, including thickness h, layer-averaged salinity S_a and temperature T_a, salinity S_{-h} and temperature T_{-h} at the base of the SML, and vertical gradients of salinity $\frac{\partial S}{\partial z}\big|_{-h}$ and temperature $\frac{\partial T}{\partial z}\big|_{-h}$ at the base of the SML. The vertical gradients are calculated from the nearest two data points on either side of h. Profiles are first linearly interpolated to a regular 2 m vertical spacing, and h is then determined by a threshold density criteria, specifically the shallowest measurement where $\rho_h > \rho_{10m} + 0.125\,\mathrm{kg\,m^{-3}}$. Other studies (de Boyer Montégut et al., 2004) have suggested a smaller density threshold such as $0.03\,\mathrm{kg\,m^{-3}}$ better matches the MLD based on visual analysis of profiles, but we choose a medium threshold here to avoid false identification of layers associated with diurnal warming or other transient features not representative of the monthly mean SML.

Each of the seven fields listed above were then objectively mapped using a conventional

optimal interpolation technique (Bretherton et al., 1976). Decorrelation spatial and temporal scales were chosen a priori as $L_x = 300$ km and $L_t = 45$ days, similar to the methodology used by Schmidtko et al. (2013). We choose not to use an existing SML climatology dataset such as the Monthly Isopycnal and Mixed-Layer Climatology (MIMOC) because these climatologies use relatively coarse depth bins of 10 m or more, and properties such as vertical gradients at the base of the SML are can be more accurately calculated directly from raw profiles.

For evaporation (E) and precipitation (P), we use the Objectively Analyzed Air-Sea Fluxes for the Global Oceans (OAFlux; Yu and Weller, 2007) and the Global Precipitation Climatology Project (GPCP; Adler et al., 2003) products, respectively. We also add a river runoff term from the dataset of Dai and Trenberth (2002).

We obtain a SML velocity using geostrophic velocities ($\mathbf{u_g}$) provided by the Archiving, Validation and Interpretation of Satellite Oceanographic Data (AVISO, 2018), Ekman velocities ($\mathbf{u_{Ek}}$) calculated from the Scatterometer Climatology of Ocean Winds (SCOW; Risien and Chelton, 2008), and the drifter climatology of Lumpkin and Johnson (2013) for equatorial velocity values.

For the heat flux terms in a complimentary temperature budget we use the Coordinated Ocean Research Experiments (CORE) version 2 (Large and Yeager, 2009). CORE.v2 fluxes are based on satellite observations for the radiative components and National Centers for Environmental Protection (NCEP) reanalysis fields for the derived turbulent components. Slight adjustments are made to the derived quantities to better fit alternative but sparse observational products, and to balance the global heat budget within $2\,\mathrm{W\,m^{-2}}$. The uncorrected fluxes have a global imbalance of $30\,\mathrm{W\,m^{-2}}$, and similarly large imbalances are found in other net heat flux products such as OAflux. For ease of comparison with ECCO, shortwave absorption in the CORE.v2 net heat flux was calculated using the same empirical double exponential function, with the fraction of radiation reaching a depth z as $Q_{SWP} = 0.62 \cdot e^{\frac{-h}{0.6}} + 0.38 \cdot e^{\frac{-h}{20}}$. Therefore, some portion of the shortwave heating penetrates beyond the MLD in a shallow SML and does not contribute to mixed-layer heating.

A full list of datasets and the time periods over which the climatologies were constructed can be found in Table 3.1. Because of the differing length of the observational records, there is some temporal inhomogeneity between the datasets. The climatology generally covers the period 1981 to 2016. We do not include WOD casts before the year 1981, when the OAflux and GPCP products become available.

3.3.2 ECCO

ECCO is an ongoing inverse modelling project which aims to produce a physically consistent state estimate of the ocean constrained by observations. The release used here is ECCO.v4.r3 (Forget et al., 2015). ECCO utilizes the MITgcm solved on a lat-lon cap grid consisting of five faces which include the Arctic, and has horizontal resolution of approximately 1° and 50 vertical levels. The model configuration includes a non-linear free surface using the z^* coordinate (Adcroft and Campin, 2004) and real freshwater flux (RFWF) surface boundary condition, the Gent and Mcwilliams (GM; 1990) eddy parameterization, the Redi (1982) scheme for isopycnal mixing of tracers, and the Gaspar et al. (GGL; 1990) turbulence closure for diapycnal mixing. The solution is initialized and forced by surface fluxes calculated from ERA-Interim reanalysis fields over the period 1992-2011. Using an adjoint model, the ocean solution is optimized to fit observations from satellite altimetry, hydrographic profiles, and sea-surface temperature. Further details can be found in Forget et al. (2015).

ECCO utilizes the physically consistent RFWF condition at the free surface, where the surface vertical velocity is specified as $w|_{z^*=0} = E-P$ with no artificial flux of salt. A related approximation, used in other numerical models and often for interpreting observations, is to represent the dilution and concentration effect of $E - P$ through a virtual salt flux (VSF) and a linear free surface, where $w|_{z^*=0} = 0$ and the salt flux is given by $F_s|_{z=0} = S(E - P)$. For numerical modeling, this formulation presents some challenges in that using the local salinity in the VSF causes a global salinity drift due to the positive correlation between $E-P$ and S. Alternatively, a constant reference salinity S_0 may be used, but this underestimates the salt flux in salty regions and overestimates it in fresh ones, where salinities may even reach unphysical negative values in places like river outflows.

3.3.3 Budget Framework

To assess relative contributions of the various advection, mixing, and surface flux processes to the steady state upper ocean salinity budget, we take a similar approach to previous studies (Moisan and Niiler, 1998; Cronin and McPhaden, 1998; Johnson et al., 2002; Yu, 2011; Farrar et al., 2015).

The standard conservation equation for salt takes the form:

$$\frac{\partial S}{\partial t} + \nabla \cdot (\mathbf{u}S) = \nabla \cdot F \tag{3.1}$$

where the first term is the Eulerian rate of change, the second is the advective flux, and $\mathbf{F}$ can represent any other external or internal fluxes. Using the near incompressibility of seawater ($\nabla \cdot \mathbf{u} = 0$), the advective term can be rewritten:

$$\nabla \cdot (\mathbf{u}S) = \mathbf{u} \cdot \nabla S + S\nabla \cdot \mathbf{u} \approx \mathbf{u} \cdot \nabla S \tag{3.2}$$

While surface freshwater fluxes do add and remove mass from the control volume, this effect is small and can generally be neglected. Instead, the concentration and dilution effects on salinity can be written as a virtual salt flux into the volume (Beron-Vera et al., 1999; Farrar et al., 2015):

$$\left.\frac{\partial \mathbf{F}}{\partial z}\right|_{z=0} = S_0(E - P) \tag{3.3}$$

A mean reference salinity S_0 is used because absolute variations in salinity are generally small. The net freshwater flux also includes runoff and sea-ice terms, but the notation $E-P$ is used here as a shorthand for all surface freshwater fluxes. Next, Eq. 3.1 is integrated over the layer of interest, where we take $-h$ to be the MLD as defined by a density threshold of $\rho_h > \rho_{10m} + 0.125\,\mathrm{kg\,m^{-3}}$:

$$\int_{-h}^{0} \left(\frac{\partial S}{\partial t} + \mathbf{u} \cdot \nabla S - S_0(E - P) = 0 \right) dz \tag{3.4}$$

The 3-dimensional velocity $\mathbf{u}$ can be separated into different components, including a constant horizontal component averaged across the layer $\mathbf{u_a}$, a horizontal component that deviates from the vertical average describing the velocity shear $\hat{\mathbf{u}}$, the horizontal velocity at the base of the layer $\mathbf{u_{-h}}$, and a vertical velocity at the base of the layer w_{-h}. A similar definition is applied to the salinity field to obtain S_a and S_{-h} (Fig. 3-2).

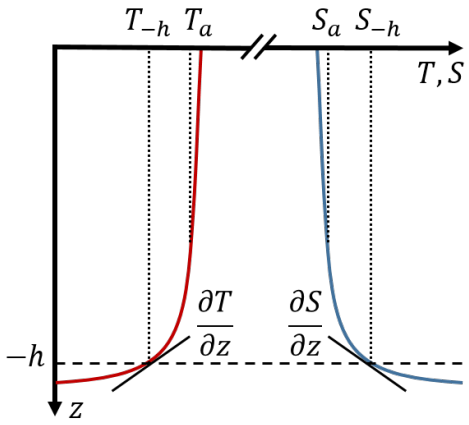

Figure 3-2: Schematic of temperature and salinity profiles within the SML. The SML is well-mixed, but as a function of the density threshold definition, it does not have uniform S and T. S_a and T_a represent the layer-averaged values and S_{-h} and T_{-h} are the values at the layer base $z = -h$. Because there is a sudden increase in stratification at the bottom of the SML, there are significant gradients $\frac{\partial S}{\partial z}$ and $\frac{\partial T}{\partial z}$ at $z = -h$

The application of this decomposition is described in full detail by Moisan and Niiler (1998), but briefly summarized, the advective terms can rewritten as:

$$\begin{aligned}\int_{-h}^{0} \nabla \cdot (\mathbf{u}S)\, dz =& \nabla \cdot \int_{-h}^{0} \mathbf{u}S\, dz - \mathbf{u_{-h}} \cdot S_{-h} \nabla h + \nabla S_a \cdot \int_{-h}^{0} \mathbf{u}\, dz \\ &+ S_a \nabla \cdot \int_{-h}^{0} \mathbf{u}\, dz - \nabla \cdot \mathbf{u_a} \int_{-h}^{0} S\, dz + w_{-h} \cdot (S_a - S_{-h})\end{aligned} \tag{3.5}$$

Using the fact that there is no advective salt flux out the top of the layer ($w_0 = 0$ in the linear free-surface approximation), rewriting the advective terms using $\hat{\mathbf{u}}$ and $\mathbf{u_{-h}}$, and applying Eq. 3.5 to Eq. 3.4, gives:

$$h\frac{\partial S_a}{\partial t} + h\mathbf{u_a} \cdot \nabla S_a + \nabla \cdot \left(\int_{-h}^{0} \hat{\mathbf{u}}\hat{S}\, dz \right) + (S_a - S_{-h}) \cdot \left(\frac{\partial h}{\partial t} + \mathbf{u_{-h}} \cdot \nabla h + w_{-h} \right) - S_a(E - P) = 0 \tag{3.6}$$

where the terms from left to right represent salt storage, advection by the vertically averaged velocities, anomalous vertical advection, entrainment, and surface fluxes. Dividing through by h gives each term as a salinity change per unit time in the control volume:

$$\frac{\partial S_a}{\partial t}+\mathbf{u_a}\cdot\nabla S_a+\frac{1}{h}\nabla\cdot\left(\int_{-h}^{0}\hat{\mathbf{u}}\hat{S}\;dz\right)+\frac{1}{h}(S_a-S_{-h})\cdot\left(\frac{\partial h}{\partial t}+\mathbf{u_{-h}}\cdot\nabla h+w_{-h}\right)-\frac{S_a}{h}(E-P)=0 \tag{3.7}$$

Although common practice, a Heaviside function is not applied to the entrainment term here, because detrainment does in fact change the mixed-layer salinity (see Kim et al., 2006). This is due to the fact that the "mixed-layer" is never truly mixed, and small temperature and salinity gradients do exist between $z = 0$ and $z = -h$. For example, with a negative vertical salinity gradient, detrainment removes relatively salty water from the base of the layer and freshens the SML. In the case that $S_a = S_{-h}$, as in a fully mixed layer, this treatment would correctly indicate that detrainment does not alter the salinity of the layer.

For the temperature budgets, the oceanic transport terms are identical but act on temperature gradients, and the surface flux term is given by $\frac{Q_{net}}{hc_p\rho}$ where Q_{net} is the sum of shortwave (minus the penetrative flux), longwave, latent, and sensible heat fluxes at the ocean surface and $c_p = 3994\ \mathrm{J\,kg^{-1}\,K^{-1}}$ is the specific heat of seawater.

3.3.4 Observational Calculations

Next, we apply a Reynolds decomposition where, for example $\overline{S_a}$ is the monthly climatological average salinity of the layer and S_a' is the deviation from that average value, such that $S_a = \overline{S_a} + S_a'$:

$$\begin{aligned}&\frac{\partial(\overline{S_a}+S')}{\partial t}+(\overline{\mathbf{u_a}}+\mathbf{u_a'})\cdot\nabla(\overline{S_a}+S_a')+\frac{1}{(\overline{h}+h')}\nabla\cdot\left[\int_{-h}^{0}(\overline{\hat{\mathbf{u}}}+\hat{\mathbf{u}}')\cdot(\overline{\hat{S}}+\hat{S}')\;dz\right]\\&+\left[\frac{(\overline{S_a-S_{-h}})+(S_a-S_{-h})'}{(\overline{h}+h')}\right]\cdot\left[\frac{\partial(\overline{h}+h)}{\partial t}+(\overline{\mathbf{u_{-h}}}+\mathbf{u'_{-h}})\cdot\nabla(\overline{h}+h')+(\overline{w_{-h}}-w'_{-h})\right]\\&-\left[\frac{\overline{S_a}+S_a'}{\overline{h}+h'}\right]\left[(\overline{E-P})+(E-P)'\right]=0\end{aligned} \tag{3.8}$$

Finally, we are interested in a steady-state version of the budget. To obtain the steady-state terms, we temporally average each term in Eq. 3.8. As mentioned, the tendency term even in a period of significant climate change is orders of magnitude smaller than the oceanic transports and surface fluxes. With the limited available data, the only terms that can be estimated from existing observations are those based on a monthly climatology. We

neglect the third term in Eq. 3.7, which represents the advection of gradients within the SML due to velocity shear and cannot be estimated from surface-only velocity data. For the entrainment term, we assume that the Ekman depth is above the MLD and take the velocity at the base of the layer to be $\mathbf{u_{-h}} = \mathbf{u_g^{-h}}$. This assumption is reasonable everywhere except for very shallow SMLs in the tropics, and the associated term is generally small (Moisan and Niiler, 1998). Averaging in time leaves only the "bar-bar" and "prime-prime" terms. Since we cannot adequately estimate the prime terms, many processes must be lumped into a budget residual. It is possible to represent the terms $\mathbf{u'_a} \cdot \nabla\overline{S_a}$ and $w'_{-h} \cdot (\overline{S_a - S_{-h}})$ as a turbulent flux acting on mean gradients (i.e. Schmitt and Blair, 2015). This leaves a final equation of estimable terms as:

$$\begin{aligned}\frac{\partial S}{\partial t} = \frac{\overline{S_a}}{\overline{h}}(\overline{E-P}) - \overline{\mathbf{u_a}} \cdot \nabla\overline{S_a} - \left(\frac{\overline{S_a - S_{-h}}}{h}\right) \cdot \left(\frac{\partial \overline{h}}{\partial t} + \overline{\mathbf{u_g^{-h}}} \cdot \nabla\overline{h} + \overline{w_{Ek}}\right) \\ + \nabla \cdot (\kappa_H \nabla\overline{S_a}) + \kappa_V \left.\frac{\partial \overline{S}}{\partial z}\right|_{-h} + res\end{aligned} \tag{3.9}$$

$$TEND = SFLUX + ADV + ENT + HMIX + VMIX + RES \tag{3.10}$$

We do not attempt to estimate the small $TEND$ term from the relatively short and noisy observational dataset and simply assume it is zero. This equation can be estimated in a finite difference framework using the OBS dataset.

To estimate the average SML velocity $\mathbf{u_a}$, we use a combination of the geostrophic velocity $\mathbf{u_g}$ from AVISO altimetry data, and an Ekman transport $\mathbf{u_{Ek}}$ estimated from the wind climatology SCOW, where:

$$\mathbf{u_{Ek}^a} = \frac{\tau_\mathbf{w} \times \hat{z}}{f\rho h} \tag{3.11}$$

is an Ekman velocity calculated from the total Ekman transport due to a wind stress $\tau_\mathbf{w}$ divided evenly into the layer of thickness h. The finite extent of the Ekman layer is an important distinction that prohibits the use of an existing velocity climatology such as the Ocean Surface Current Analysis Real-time (OSCAR) product, which provides an estimated mean velocity across the top 30 m layer. This is because in a deep SML, the Ekman velocity decays exponentially following a scale depth of $h_{Ek} = \sqrt{\frac{2\kappa_v}{f}}$ which is typically $\approx 10 - 50$ m, and using a velocity based on an average of the upper 30 m would greatly

overestimate the average $\mathbf{u_{Ek}}$ across a deep SML. $\mathbf{u_{Ek}}$ is not calculated within 10° of the equator where f becomes small. These values are instead replaced with those from the drifter climatology. This drifter velocity cannot be used everywhere in the variable depth SML framework because drifters measure the velocity at 15 m, and would again overestimate $\mathbf{u_{Ek}}$ in deep SMLs. However, the use of drifter velocities is a reasonable approximation near the equator where the SML is shallow.

The geostrophic velocity term used here is a combination of the geostrophically balanced surface velocity ($\mathbf{u_g^s}$) acquired from satellite altimetry plus a thermal wind term which specifies the vertical shear due to lateral density gradients in the SML climatology:

$$\mathbf{u_g}(z) = \mathbf{u_g^s} - \int_{-h}^{0} \frac{g\hat{\mathbf{k}}}{f\rho_0} \times \nabla\rho \; dz \tag{3.12}$$

The shear due to thermal wind is generally second-order but is included here for completeness. The average geostrophic velocity within the SML is obtained by vertically averaging this profile over the layer:

$$\mathbf{u_g^a} = \mathbf{u_g^s} - \frac{h}{2} \cdot \frac{g\hat{\mathbf{k}}}{f\rho_0} \times \nabla\rho \tag{3.13}$$

The vertical velocity at the base of the SML is estimated as the Ekman pumping rate:

$$w_{ek} = \frac{\nabla \times \tau_{\mathbf{w}}}{\rho f} \tag{3.14}$$

The mixing terms cannot be accurately estimated from data, but we use a simple diffusive parameterization based on the mean tracer gradients to get an idea of their sign and magnitude. In the estimates presented here, we set $\kappa_h = 2000\,\mathrm{m^2\,s^{-1}}$ and $\kappa_v = 2 \times 10^{-5}\,\mathrm{m^2\,s^{-1}}$. An alternative would be to include the mixing terms in the residual, but for the purposes of this analysis the diffusive parameterization is illustrative.

Because the advection and horizontal mixing terms depend on the salinity gradients, significant noise is introduced into the field through this derivative and the transport is highly sensitive to the alignment of velocity and tracer gradient features. Therefore, a square boxcar filter of 5° width is applied to the advective terms in order to remove excessive small-scale noise.

3.3.5 ECCO Calculations

Calculating a budget within the ECCO framework is simpler, because the terms can be measured exactly at the faces of the model's native C-grid. The model output conforms naturally to a finite volume formulation of Eq. 3.1 to calculate the tendency in each cell due to the various terms. The instantaneous tendency in a given cell is simply the sum of the fluxes into it:

$$\frac{\partial S_{i,j,k}}{\partial t} = F^x_{i-\frac{1}{2},j,k} - F^x_{i+\frac{1}{2},j,k} + F^y_{i,j-\frac{1}{2},k} + F^y_{i,j+\frac{1}{2},k} + F^z_{i,j,k-\frac{1}{2}} + F^z_{i,j,k+\frac{1}{2}} \tag{3.15}$$

The tendency within the mixed-layer is obtained by vertically summing the horizontal fluxes down to the MLD and adding the surface flux at the top of the cell plus the advective and diffusive fluxes out the bottom face. The ECCO outputs include averaged fluxes at each face for the surface salt flux, advection, vertical mixing, horizontal mixing, and the GM advection.

The MLD is taken to be a discontinuous step function calculated at each grid cell rather than a smoothly sloping surface in order to take advantage of the exact flux fields which are calculated at each face. Therefore, advection along the sloped SML base is described by both the vertical and lateral velocities, and we combine these fluxes into a single advection term. Net advection across the SML base is small and primarily due to Ekman pumping, so we do not try to separate it into a distinct vertical advection term here. Following this choice, the Ekman pumping term is also added into the advection term in the observation budget (hereafter referred to as OBS) rather than to the entrainment term.

Because of the time-varying layer depth formulation, there is an entrainment term at the bottom of the layer which we calculate using the closure formula of Kim et al. (2006):

$$ENT = \alpha \frac{\Delta h}{H} \cdot (S^1_{t-1} - S^2_t) \tag{3.16}$$

where Δh is the thickness of the layer to be entrained or detrained, H is the larger thickness of the SML between the current and previous month, S^1_{t-1} is the salinity of the thinner layer at the last timestep, and S^2_{t-1} is the salinity of the layer at the last timestep to be entrained or detrained. Because the ECCO outputs are based on monthly averages

rather than instantaneous values at the end of the months, the ENT cannot be calculated exactly and introduces a small residual, but does not affect the main results presented here.

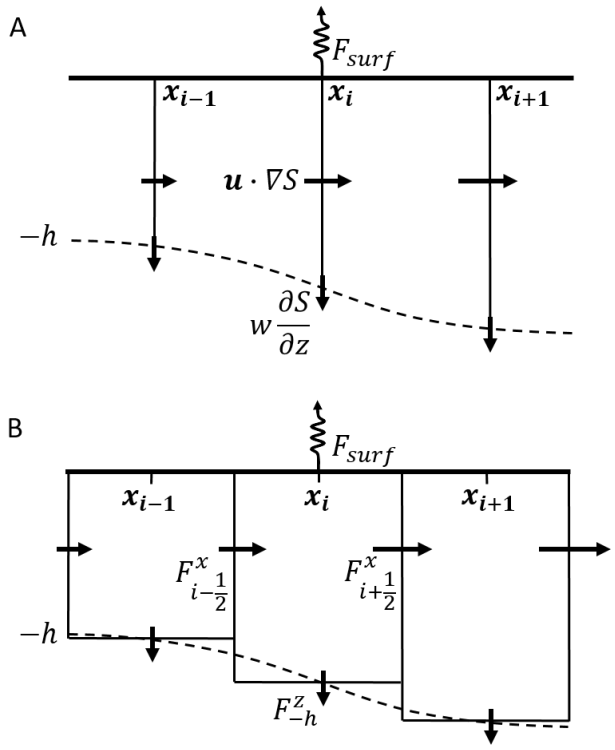

Figure 3-3: Schematic of the SML budget framework. The control volume is a spatially and temporally varying surface layer of depth h. (A) The finite difference formulation used for OBS, where the divergence of fluxes is estimated at a discrete grid of longitude and latitude points. (B) The finite volume approach used for ECCO, where the salinity tendencies in the control volume are estimated directly from the fluxes entering and exiting the sides of the model's grid cells.

Interpreting the ECCO output in terms of the VSF formulation requires a simple adjustment to the advective flux. Without the imposed surface vertical velocity of the RFWF, the divergence term $\nabla \cdot \mathbf{u_{rfwf}}$ used in calculating the advective flux must be rewritten as (following Vinogradova and Ponte, 2017):

$$\nabla \cdot \mathbf{u_{vsf}} - (E - P) \tag{3.17}$$

The initial advective flux is calculated as

$$ADV_{rfwf} = \nabla \cdot (\mathbf{u}S) = S \cdot \nabla \cdot \mathbf{u} + \mathbf{u} \cdot \nabla S \tag{3.18}$$

so the new advective flux becomes:

$$ADV_{vsf} = ADV_{rfwf} - S(E - P) \tag{3.19}$$

3.4 Budget Results

An appropriate starting point in assessing the budget calculations is to compare several fundamental properties of the SML between the ECCO and OBS datasets. Both have qualitatively similar seasonal variations in MLD (Fig. 3-4, lower), although the ECCO MLD is 6% shallower than OBS in the global annual average. ECCO has a slightly deeper SML in the subtropics, particularly in winter, and a shallower SML near 10°N and 10°S which increases the surface forcing tendency there from the ITCZ. The SML of ECCO is 0.11 psu fresher than OBS in the global average (Fig. 3-5), but the salinity patterns are qualitatively very similar. This is in agreement with the MIMOC climatology which is also saltier than the ECCO SML (not shown here).

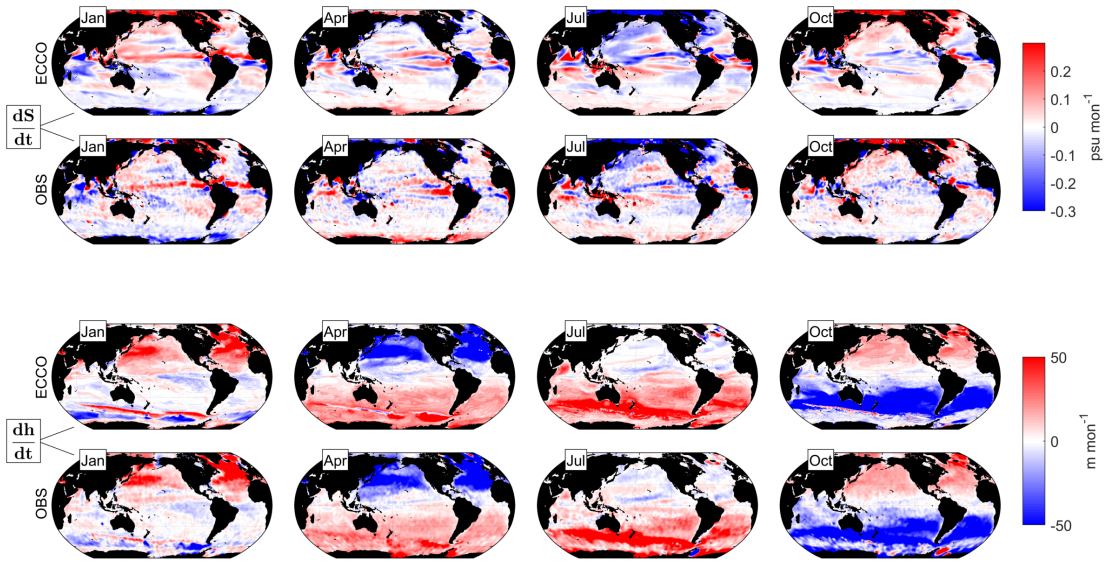

Figure 3-4: Snapshot monthly comparison of ECCO and OBS for the terms $\frac{\partial S}{\partial t}$ (upper) and $\frac{\partial h}{\partial t}$ (lower). Maps are plotted for the months of January, April, July, and October. The seasonal cycle of SML properties is comparable between the two datasets.

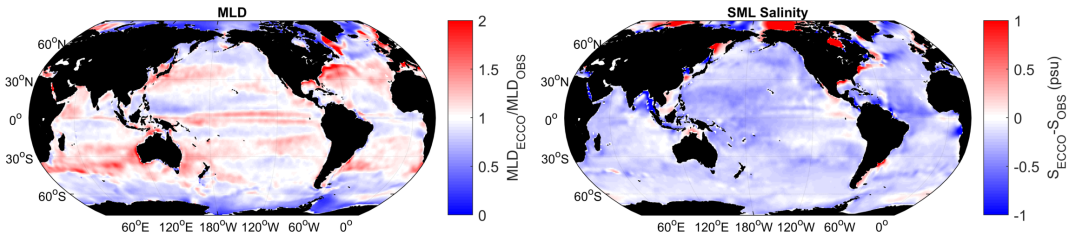

Figure 3-5: Comparison of SML properties between ECCO and OBS, showing the ratio of the annual average MLD $\frac{h_{ecco}}{h_{obs}}$ (left) and the difference in annual average SML salinity $S_{ecco} - S_{obs}$ (right). ECCO has a slightly shallower and fresher SML than OBS on average.

The magnitude of the salinity gradient is key in determining the advective and mixing fluxes. Fig. 3-6 shows the lateral and vertical salinity gradients for the SML in ECCO and OBS, which are also very similar.

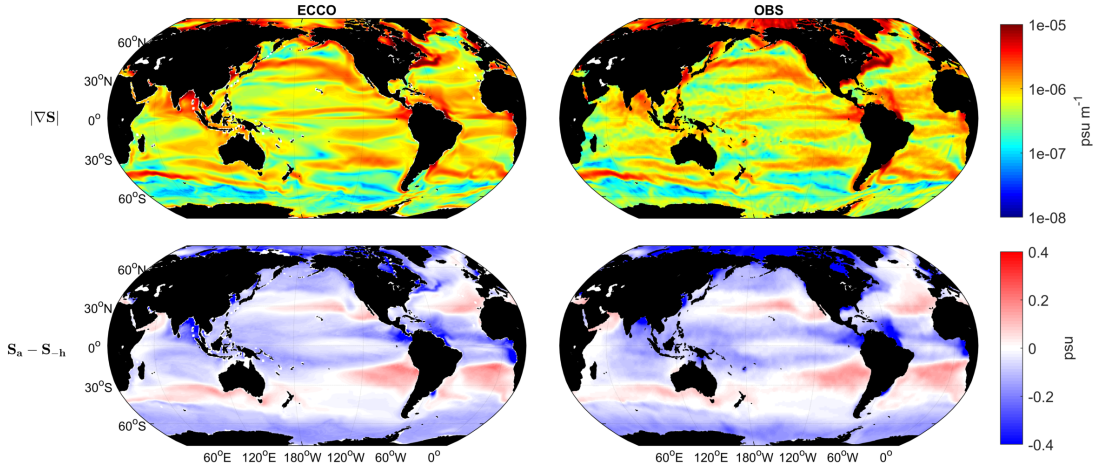

Figure 3-6: Magnitude of the annual average horizontal salinity gradient ∇S (upper) and the annual average vertical salinity difference $S_a - S_{-h}$ between the SML average and the SML base (lower). ECCO is shown on the left, and OBS on the right.

Fig. 3-7 shows the strength of the major budget terms described in Eq. 3.9 for ECCO. As the ECCO budget is closed exactly, the bottom right panel shows the salinity tendency over the model period. As expected, the tendency is nearly two orders of magnitude smaller everywhere than the largest flux terms.

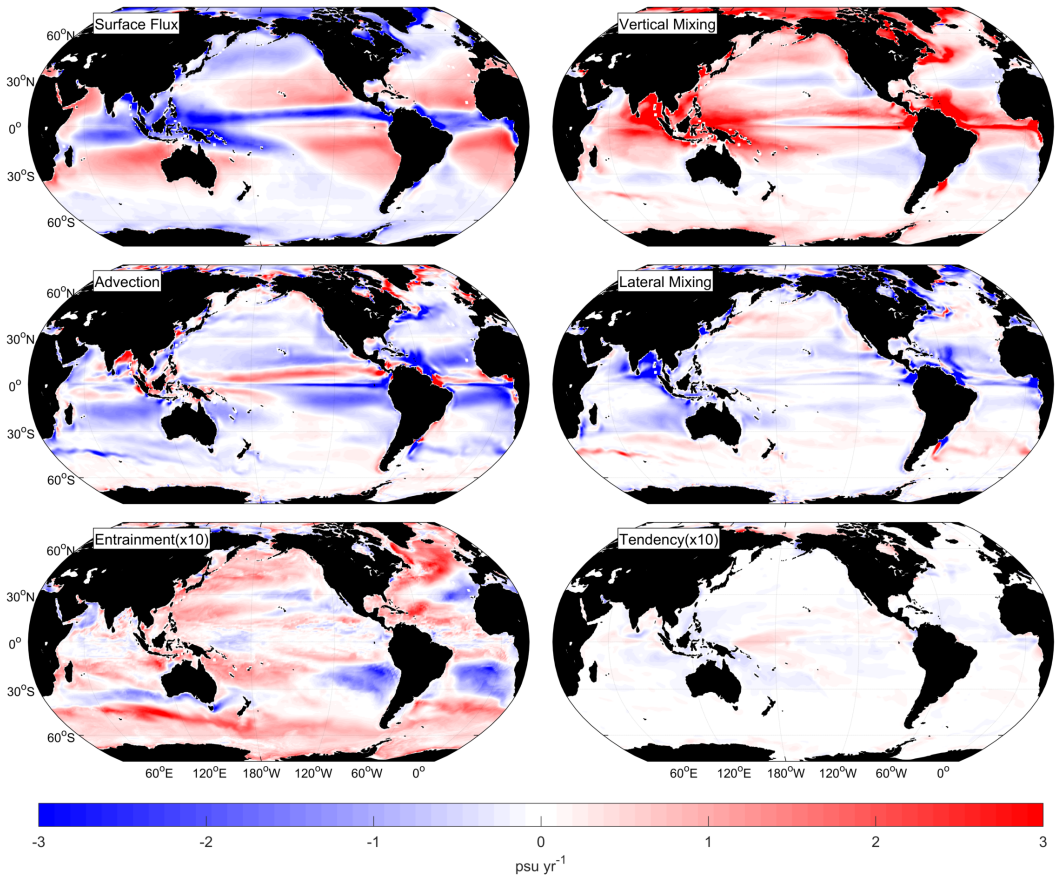

Figure 3-7: Summary of the SML salinity budget calculated in ECCO, showing the terms as described in Eq. 3.9 as $SFLUX$, $VMIX$, ADV, $HMIX$, and ENT. The lower right panel shows the $TEND$ with no RES since the budget closes. Maps are plotted as forcing tendency in the SML with units $\mathrm{psu\,yr^{-1}}$. As ENT and $TEND$ are significantly smaller than other terms, these have been multiplied by a factor of 10.

The budget shows a relatively even contribution from vertical mixing and advection, with one of these terms working as the primary opposition to surface forcing in most regions. Lateral mixing and entrainment are generally second order but significant in specific locations. The lateral mixing produces a substantial transport of freshwater from the equator into the subtropical gyres in agreement with Busecke et al. (2017), and some transport of salty water from the subtropics into the subpolar regions.

Fig. 3-8 shows the comparable budget terms calculated from OBS. Qualitatively, the terms are in broad agreement with those from ECCO. Advective transports are large around the ITCZ, mirroring the freshwater forcing there. Vertical mixing and entrainment both act to freshen the subtropical gyres and salinify the subpolar gyres, while lateral mixing is most

significant in frontal zones. Due to uncertainties in the advection term and the very crude treatment of the mixing terms, which play an order one role in the ECCO budget, the OBS budget is left with a large residual in most regions. To reduce the residual, a useful next step would be to utilize spatially varying mixing coefficient estimates based on various global estimates of eddy diffusivities (i.e. Zhurbas et al., 2014; Abernathey and Marshall, 2013). This is because energetic oceanic regions, such as the western boundary current extensions, undergo more mixing than quiescent regions. The constant diffusivity used here underestimates mixing in energetic regions and overestimates it in quiescent ones.

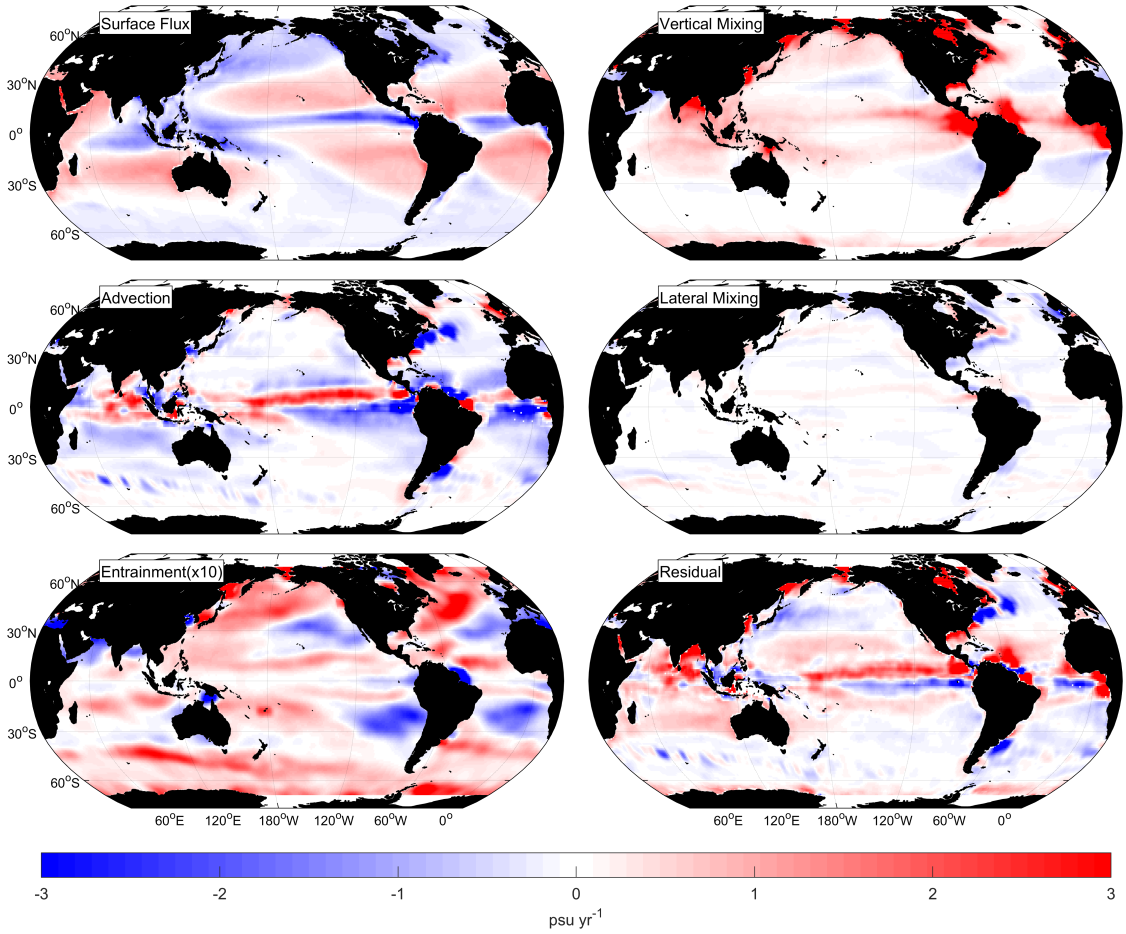

Figure 3-8: Same as Fig. 3-7 but for the OBS dataset. Since the OBS budget does not close, the lower right panel shows a residual term rather than a tendency over the period. *ENT* has been multiplied by a factor of 10.

The advective transport can be separated into its Ekman and geostrophic components (Fig. 3-9). This decomposition reveals broad regions where one type of flow dominates in the salt transport. In the tropics, Ekman currents are strong and perpendicular to den-

sity gradients and have the largest salt transport. At higher latitudes, Ekman transports are weaker and the SML is deeper, so that the geostrophic flow of the gyres is the leading advective transport. While geostrophic currents in the western boundaries and Antarctic Circumpolar Current (ACC) are fast, these flows are generally aligned with the tracer gradients, producing little salt transport. The Ekman transport is nearly perpendicular to these meridional density gradients, and therefore its salt transport often exceeds that from geostrophic currents despite the weaker flow. It is also worth noting that in many regions, the Ekman and geostrophic transports oppose one another. On the equatorward sides of the subtropical gyres for example, poleward Ekman flow opposed the equatorward Sverdrup flow.

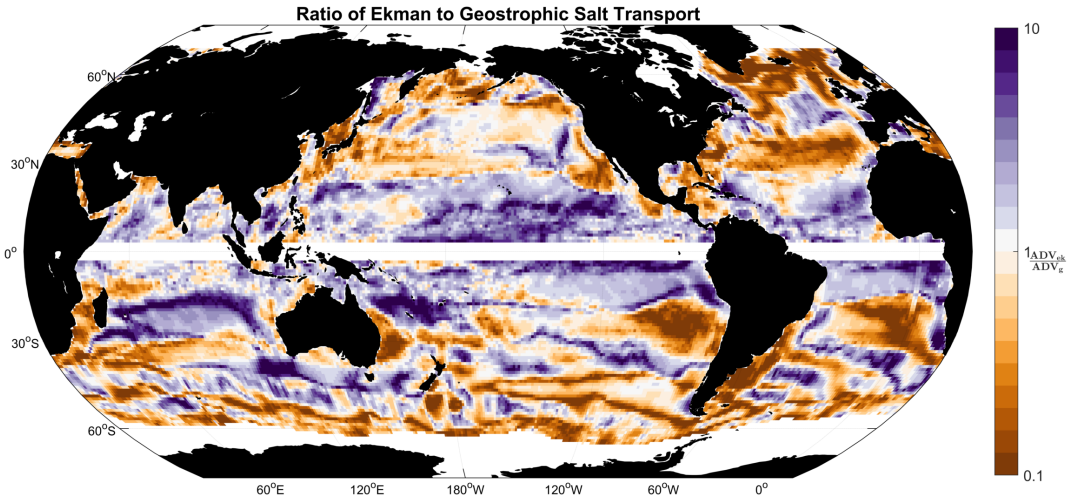

Figure 3-9: Ratio of the magnitude of Ekman to geostrophic salt transports calculated from the observations as $\frac{\mathbf{u_{Ek}}\cdot\nabla S}{\mathbf{u_g}\cdot\nabla S}$, shown on a log scale. Ekman transport is larger in the tropics where the SML is shallow and Ekman velocities are large, while geostrophic transport is generally larger at higher latitudes.

In both ECCO and OBS, the entrainment term is a generally an order of magnitude smaller than the dominant balance, but can be regionally important. While entrainment is quite significant in the seasonal cycle, $\overline{\frac{dh}{dt}} = 0$ averaged over the annual cycle, such that the entrainment term is second-order in the annual mean.

The large-scale effects of entrainment are often considered through the theory of "Stommel's Demon" (Stommel, 1979; Williams et al., 1995), which describes the annual average effect of the seasonal cycle of MLD on interior waters. Without a background flow, the

cyclically shoaling and deepening mixed-layer would simply reabsorb the same waters from the seasonal pycnocline each year, with no net change. Stommel's insight was that with a background flow, water detrained from the SML will have moved horizontally at a later time. Detrained parcels in the subtropics, for example, will have been displaced equatorward (where the SML is shallower) via Sverdrup flow and downward via Ekman pumping. This causes a subset of detrained water (specifically late winter water) to irreversibly enter the permanent pycnocline during a period of effective detrainment.

The effect of entrainment on the SML itself has received less attention, and we consider mechanisms at play here. A simple application of Stommel's Demon would suggest that through effective removal of late winter water only, when the subtropical SML is at its freshest, entrainment would increase the salinity of the subtropical SML in the annual average. However in the budget calculated here, entrainment has a freshening effect across much of the eastern subtropical gyres. One difference between Stommel's theory and the SML dynamics analyzed here, is that Stommel considered bulk effects over interior isopycnals rather than a point-wise budget.

Because the annual average of $\frac{\partial h}{\partial t}$ is zero, a nonzero steady-state entrainment term must arise from a Reynolds average in the seasonal cycle, i.e.:

$$\overline{\left(\frac{S_a - S_{-h}}{h}\right)' \frac{\partial h}{\partial t}'} \tag{3.20}$$

Locations with a negative salinity tendency due to this term must entrain relatively fresh water and detrain relatively salty water. One possible mechanism for this seasonal correlation is lateral transports, similar to the dynamics underlying Stommel's mechanism. The meridional salinity gradient between the subtropical and subpolar gyres is negative, so that entrained and detrained waters may have different salinities due to the large-scale Sverdrup flow. These mechanisms deserve further study, but the role of entrainment is small in the budgets calculated here.

3.5 Dominant Processes

The SML budget derived here helps to identify several distinct dynamical regions in terms of their steady-state salinity balances. Using the budgets calculated above, we further consolidate the balance into 3 terms:

$$\begin{aligned} HOR &= ADV + HMIX \\ VER &= VMIX + ENT \\ SURF &= E - P \end{aligned} \tag{3.21}$$

Using this simplification, the two terms with leading magnitude are used to designate a dominant balance in the SML. This simplifies the SML into regions where the surface flux is either dominantly balanced by lateral transports or vertical transports, as well as regions where the surface forcing is weak and the two ocean terms are leading order. Fig. 3-10 plots this dominant balance using the ECCO budget. The magnitude of each of the three terms is remapped onto the range $(0, 1)$ by calculating a fraction with the magnitude of the largest term in the denominator, i.e.:

$$\begin{aligned} HOR_{frac} &= \frac{|HOR|}{max(|HOR|, |VER|, |SURF|)} \\ VER_{frac} &= \frac{|VER|}{max(|HOR|, |VER|, |SURF|)} \\ SURF_{frac} &= \frac{|SURF|}{max(|HOR|, |VER|, |SURF|)} \end{aligned} \tag{3.22}$$

This decomposition is further consolidated by plotting the two leading terms to obtain a dominant balance, and a clear geographic pattern emerges. Where local extrema of the salinity field exist, including the ITCZ and the subtropical gyre centers, lateral transports are weak because the horizontal gradient of salinity is small. Instead, vertical transports between the SML and the thermocline balance the surface forcing. The subpolar gyres and Southern Ocean also display this balance. Here, layer-averaged velocities tend to be weaker both because the Ekman transport is inversely proportional to f, and because the SML is deeper due to weak thermal stratification.

Another category of dynamics occurs where lateral transports are large and primarily balance the surface forcing. These regions are mostly confined to the subtropical latitudes of approximately 10° to 25°, where Ekman transports are strongest and the SML is relatively shallow. Here, subtropical evaporation is countered by a poleward transport of freshwater from the ITCZ, as part of the upper limb of the shallow overturning which occurs in the subtropical cells (STCs). Below the SML, the lower limb of the STC completes the circulation,

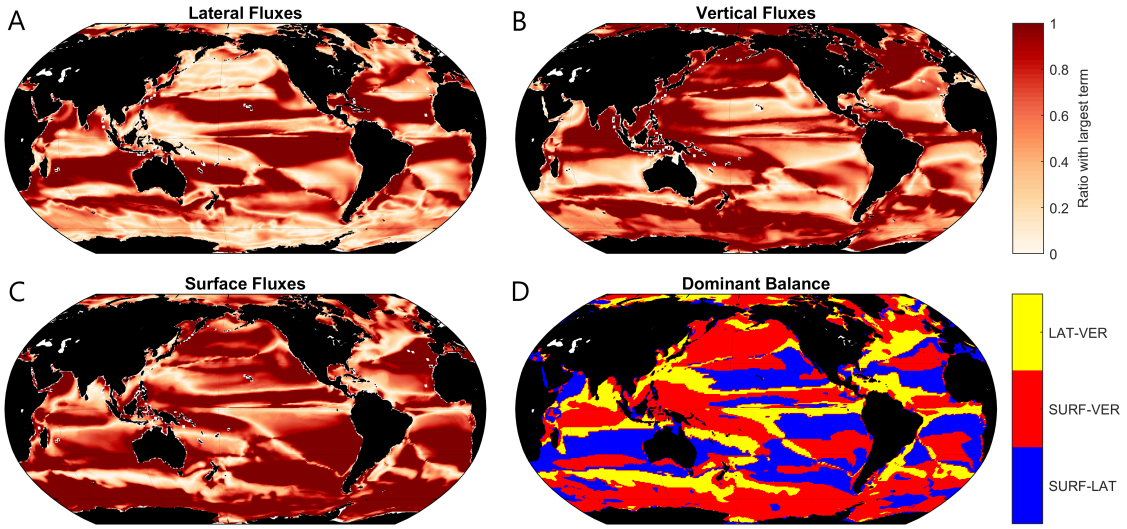

Figure 3-10: (A-C) Magnitude of the three salinity budget terms $LAT, VER, SURF$ divided by the magnitude of the largest term, as in Eq. 3.22. (D) Dominant balances in the SML salinity budget, calculated as the two leading terms by magnitude using the 3-term decomposition of Eq. 3.21.

carrying salty water which is fluxed through the SML in the gyre centers back towards the equator, where it provides the necessary salt to balance precipitation there. Each subtropical gyre center shows roughly this same dynamical balance, but there are subtle differences between them (Gordon et al., 2015). A primary balance between lateral fluxes and surface forcing is also seen near most coastal regions, where river input is carried away via lateral advection.

A third dynamical category occurs where the dominant balance is purely oceanic, with lateral salt transports within the SML counteracted by vertical transports through the SML base. Generally, this balance is found in locations that lie between the primary regimes of the water cycle (i.e. between the tropics and subtropics or between the subtropics and high latitudes) where the net freshwater flux is near zero. A primary oceanic balance is also found in the western boundary currents and ACC, where advective transports are particularly strong. One region of interest is the Gulf Stream and North Atlantic Current, where a large swath of ocean-only balance covers the intergyre boundary and into the subpolar gyre. Here the oceanic transports exceed the relatively weak surface flux, with significant contributions from both the mean advection and the parameterized eddy fluxes.

For another perspective, Fig. 3-11 shows the zonally integrated salinity tendency due to each term in Eq. 3.9. A zonal integral smooths over the effects of boundary currents and

coastal processes to show the average tendency at each latitude. This perspective makes it clear that strong vertical mixing balances freshwater forcing near the equator and at high latitudes, and that a combination of lateral advection and mixing balances net evaporation in the subtropics.

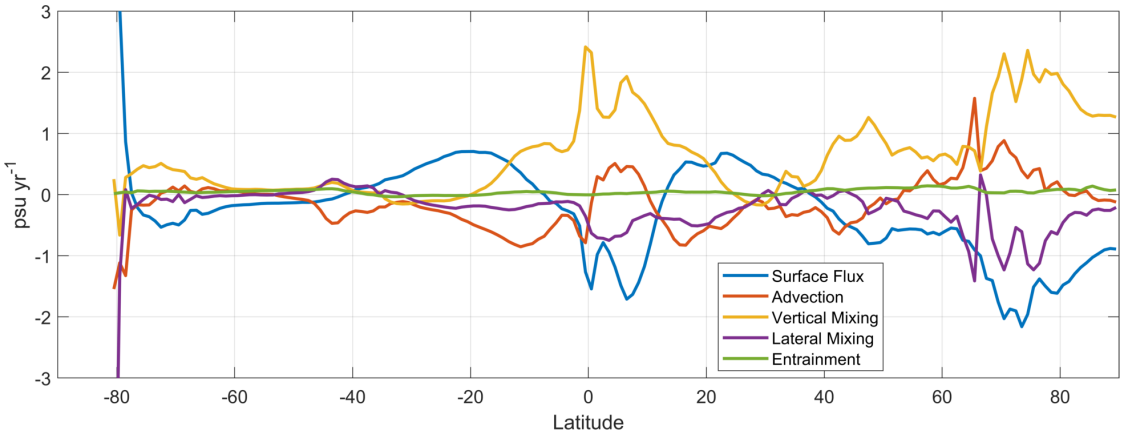

Figure 3-11: Zonal integral of the ECCO SML salinity budget showing the terms described by Eq. 3.9. The integration is calculated by volume to account for zonal variations in the MLD.

3.5.1 Comparison to Heat Budget

To better contextualize these balances, we can compare to an identical decomposition of heat fluxes. Temperature is advected by exactly the same circulation as salt, meaning that differences in the steady balances must be a result of either the surface forcing or gradients within the temperature field. Fig. 3-12 shows the 3-term decomposition for temperature as shown above for salt. Again, the subtropical gyres and subpolar gyres appear as regions where surface forcing is primarily balanced by vertical transport. The subtropical latitudes also show strong lateral heat transports, as heat is advected away from the equator and given up to the atmosphere.

In contrast to salinity, there is only a narrow region centered on the equator where vertical transports of heat exceed the lateral transports. While lateral temperature gradients are relatively weak in the tropics, vertical gradients are even weaker because the SML is primarily salt-stratified across much of the tropics.

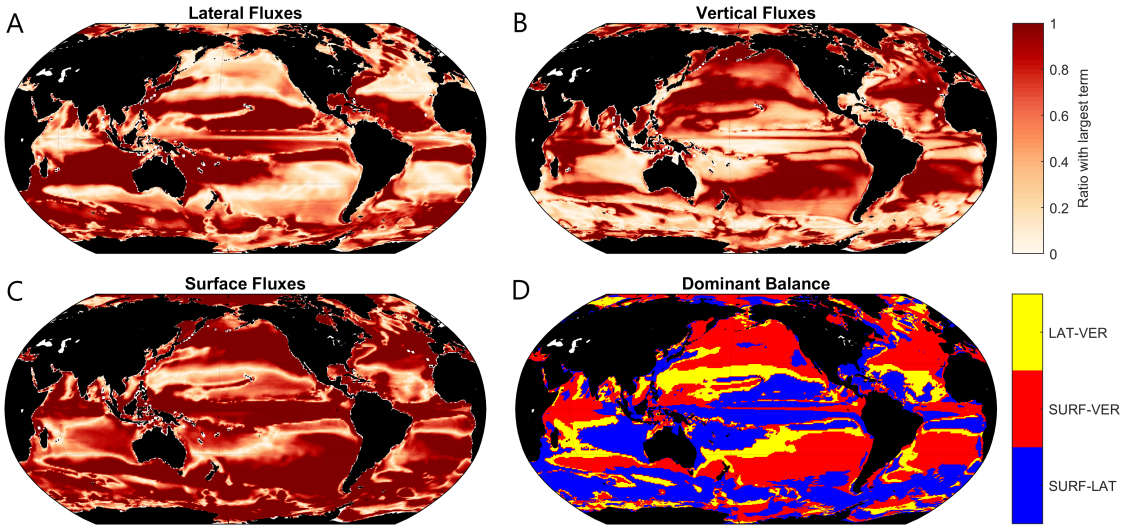

Figure 3-12: (A-C) Magnitude of the three temperature budget terms $LAT, VER, SURF$ divided by the magnitude of the largest term, as in Eq. 3.22. (D) Dominant balances in the SML temperature budget, calculated as the two leading terms by magnitude using the 3-term decomposition of Eq. 3.21.

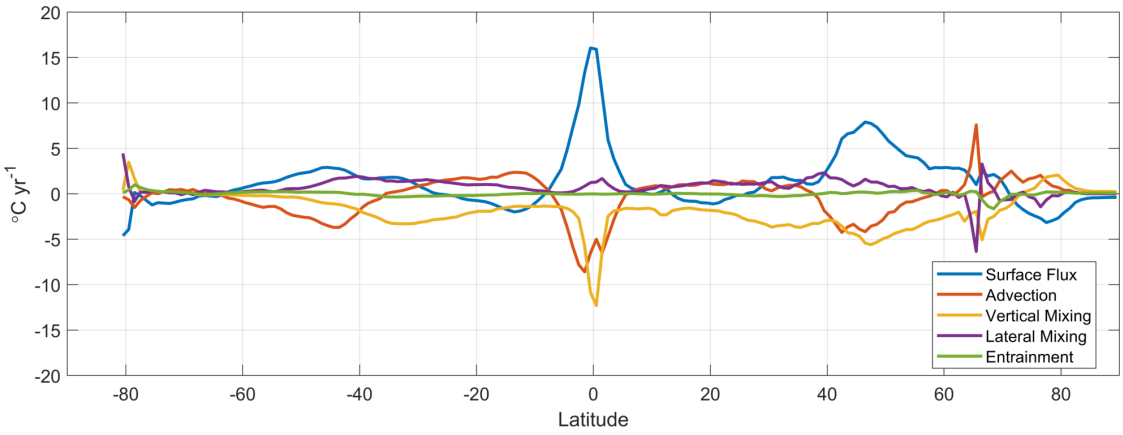

Figure 3-13: Zonal integral of the ECCO SML temperature budget showing the terms described by Eq. 3.9. The integration is calculated by volume to account for zonal variations in the MLD.

Additionally in the Southern Ocean, surface heat fluxes are largely balanced by lateral heat transport which is opposite to the salinity dynamics. The Southern Ocean is a region of ocean heat uptake, as sloping isopycnals of cold water outcrop at the surface and interact with the atmosphere via sensible heat gain. This provides a positive buoyancy flux, as does net freshwater input over the region. However, despite positive surface buoyancy flux, the Southern Ocean has very weak vertical stratification. Because of the non-linear equation of state and the cold temperatures of the region, the Southern Ocean is primarily salt-stratified.

While temperature gradients can be significant at the base of the SML, they reverse sign throughout the seasonal cycle, with cold water overlying warm through the winter and spring months. This leads to a small value for the annually averaged vertical fluxes into the layer, and a dominance of lateral transports.

3.6 Seasonal Balances

To further contrast the dynamics of salinity and temperature, we provide a brief analysis of the seasonal cycle. Fig. 3-14 shows a seasonal budget averaged over the ECCO record for different locations in the North Atlantic. Since the steady-state budgets were calculated using only climatological data, the seasonal budget is calculated identically, but without the final step of averaging over the monthly record.

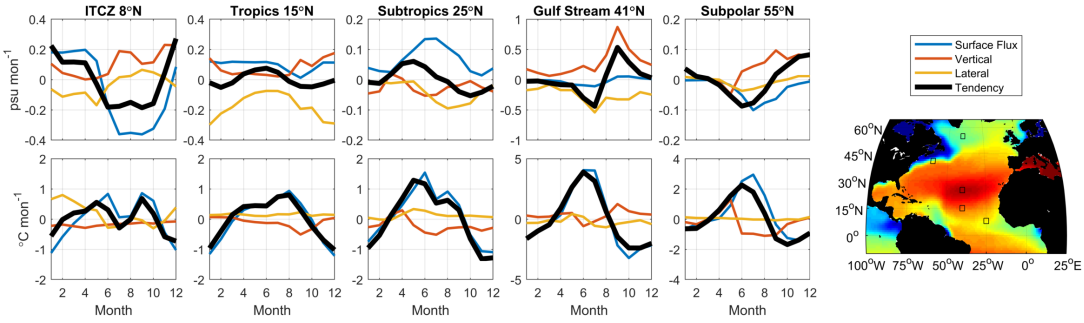

Figure 3-14: Seasonal S (upper) and T (lower) budgets calculated at 5 locations in the North Atlantic, as shown on the inset map. In the S budget, $SURF$ is significantly balanced by ocean processes at all locations, while in the T budget, $SURF$ is largely unbalanced and $TEND$ closely follows the seasonal cycle of heat fluxes.

Of the regions chosen, the ITCZ and Gulf Stream have the largest seasonal salinity cycle with tendencies as large as $0.5\,\mathrm{psu\,mon^{-1}}$ in the Gulf Stream and $0.2\,\mathrm{psu\,mon^{-1}}$ in the ITCZ (Fig. 3-14). Even in these regions with a strong seasonal cycle, the surface forcing is at least partially balanced by ocean transports at all times. While the seasonal cycle is strong in the Gulf Stream (and other western boundary currents), this is not a result of changes in surface forcing as the net $E-P$ is weak throughout the season. Instead, the salinity changes are due to a large increase in vertical mixing of salt across the SML base during fall.

The weak role of surface forcing in the seasonal salinity cycle is in contrast to the seasonal cycle of temperature, where the tendency term is an almost completely uncompensated

response to the surface forcing in most locations. This points to a fundamental difference in the seasonal dynamics between salt and heat, where the freshwater flux is partially balanced by ocean transports through the year, while ocean dynamics are second order when compared to heat fluxes in the temperature budget.

3.7 Climate Signal Pathways

The steady-state budget presented here provides context for how salt is transported between different regimes of the global water cycle. The rainy tropics and dry subtropics are connected by the shallow STCs, which carry freshwater poleward at the surface and return salty water via the subsurface branch to be upwelled at the equator. In contrast, the rainy subpolar gyres are effectively disconnected from the dry subtropics, with no direct advective surface pathway. Instead, rainfall in the subpolar regions must be balanced by upwelling of salty water from the thermocline.

This distinction provides a simple explanation for the multi-model mean salinity response seen in CMIP5. Within the subtropical latitudes, efficient lateral transport of climate-induced salinity anomalies leads to a well-mixed signal in these regions. Therefore, the freshwater forcing anomaly integrated over the entire subtropical gyre is crucial for determining the response at these latitudes, and not only the local forcing. In the Atlantic, despite increased rainfall in the ITCZ, the forcing integrated over the gyres gives a large positive $\Delta(E-P)$ term, and this signal is mixed into the ITCZ. In the Pacific, the net $\Delta(E-P)$ is small integrated over the tropics and subtropics, as the increase in ITCZ P is nearly equal to the increase in E across the subtropics (see Fig. 4-3). This explains why the Pacific subtropical gyres show a weak salinity increase.

The isolation of the subpolar regions also helps to explain the freshening response of the Atlantic subpolar gyre (SPG) seen in most models. While the integrated $\Delta(E-P) > 0$ for the Atlantic as a whole, $\Delta(E-P)$ is strongly negative for the SPG. Because the surface connection between subtropical and subpolar regions is weak, the salinification of the subtropical Atlantic does not generally reach the SPG. However, this is not the case for all models, as some do show salinified subtropical water reaching the SPG in significant quantities. Additionally, the budget presented here indicates that the intergyre boundary is a region dominated by ocean salt transports with a particularly strong mixing salt flux

seen in ECCO. This suggests that the details of ocean mixing processes may be critical for intergyre salt transport, and to the climate salinity response of the SPG. This idea is explored in more detail in Chapter 4.

3.8 Conclusions

This study presents a steady-state salinity budget for the present-day climate based on the ECCO state estimate and observational datasets. While other authors have made use of salinity budgets before, this work presents the first steady-state global budget using a SML control volume, which isolates the portion of the ocean that interacts directly with the atmosphere. The budget helps to distinguish between distinct regions of ocean salt transport dynamics. Namely, we find a region of tropical and subtropical latitudes where the surface ocean is well-connected via lateral transports within the shallow subtropical cells, and a subpolar and high-latitude region where freshwater input must be balanced by salt transported upward from deeper thermocline waters.

This decomposition of salt transports provides insight into the processes acting to control the climate salinity response, as we argue that the dynamics presented here are still applicable in a moderate climate change scenario because the salt tendency term remains small. To understand any non-local effects on the salinity field, we focus on connectivity between different regimes of the water cycle (precipitative or evaporative). The Eulerian budget perspective is useful to coarsely diagnose these transport pathways, but connectivity is much better diagnosed from a Lagrangian perspective, and we take this approach in Chapter 4.

3.9 Chapter Acknowledgements

This work was supported by NASA Headquarters under the NASA Earth and Space Science Fellowship Program award 80NSSC17K0372. The authors would like to thank the creators of all datasets used here, including ECCO, WOD, GPCP, OAFlux, CORE, AVISO, SCOW, and GDP.

3.10 Supplementary Material

While some aspects of the temperature budget are briefly presented in Chapter 3.5.1, additional figures are included here for the sake of completeness. Overall, the temperature budget shows relatively equal contributions from advection and vertical mixing as the terms which primarily counteract the local surface heat flux (Fig. 3-15), similar to the salinity budget. Lateral mixing also makes a significant contribution between the subtropical and subpolar gyres, with a second-order role for entrainment. The OBS budget does not close, but shows a qualitative similarity to the ECCO terms (Fig. 3-16). There is also good agreement in the representation of the strength and location of temperature gradients between ECCO and OBS, in addition to other properties described in Chapter 3.4.

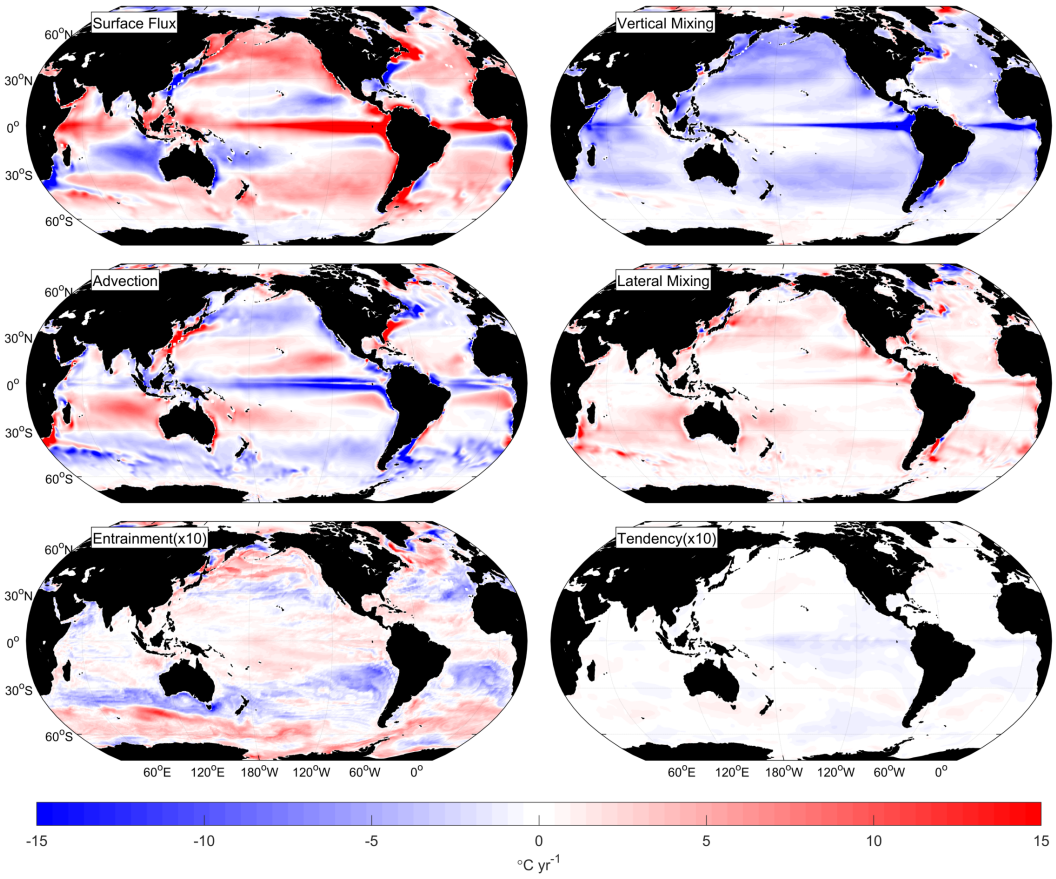

Figure 3-15: Summary of the SML temperature budget calculated in ECCO, showing the terms as described in Eq. 3.9 as $SFLUX$, $VMIX$, ADV, $HMIX$, and ENT. The last term shows the $TEND$ rather than RES since the budget closes. Maps are plotted as forcing tendency in the SML with units $^{\circ}\mathrm{C\,yr^{-1}}$. As ENT and $TEND$ are significantly smaller than other terms, these have been multiplied by a factor of 10.

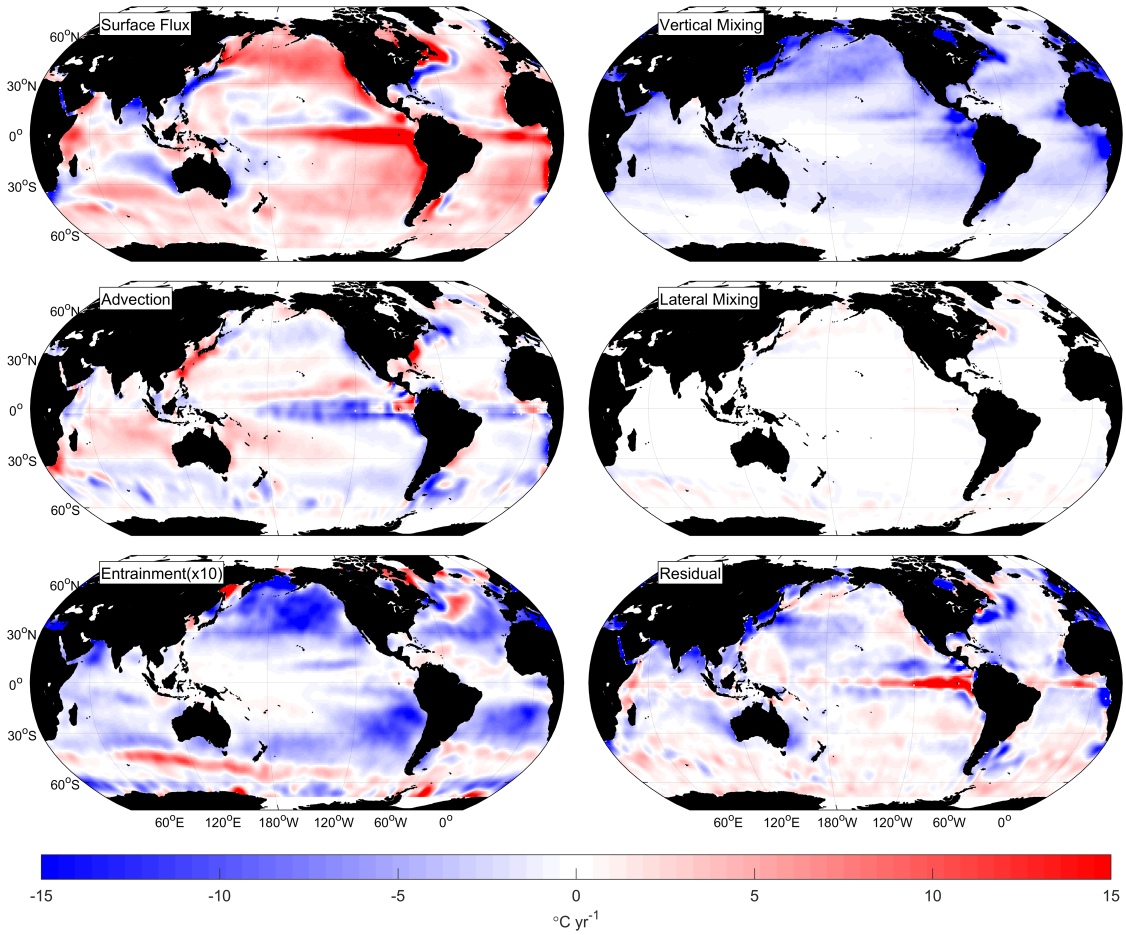

Figure 3-16: Same as Fig. 3-15 but for the OBS dataset. Since the OBS budget does not close, the lower right panel shows a residual term rather than a tendency over the period. ENT has been multiplied by a factor of 10

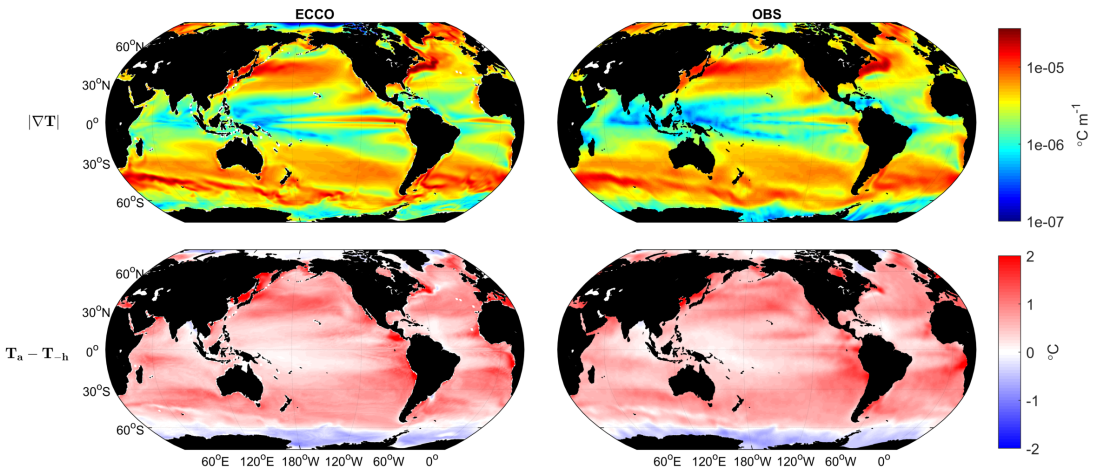

Figure 3-17: Magnitude of the annual average horizontal temperature gradient ∇T (upper) and the annual average vertical temperature difference $T_a - T_{-h}$ between the SML average and the SML base (lower). ECCO is shown on the left, and OBS on the right.

Dataset	**Variable**	**Time Period**
WOD (World Ocean Database)	S, T	1981-2016
Argo	S, T	2000-2016
AVISO (Archiving, Validation and Interpretation of Satellite Oceanographic Data)	$\mathbf{u_g}$	1993-2016
SCOW (Scatteromter Climatology of Ocean Winds)	$\mathbf{u_{Ek}}$	1999-2009
GDP (Global Drifter Program)	$\mathbf{u_{dr}}$	1979-2016
GPCP (Global Precipitation Measurement Program)	P	1981-2016
OAFlux (Objectively Analyzed Air-Sea Fluxes for the Global Oceans)	E	1981-2016
Dai Runoff	R	various-2016
CORE v2.0 (Coordinated Ocean Research Experiments)	Q_{net}	1984-2006

Table 3.1: List of datasets used to construct the OBS budget in Chapter 3, and the time periods from which the climatology was constructed. Due to varying record lengths of each dataset, some temporal inhomogeneity exists between each variable.

Chapter 4

Salinity Exchange Pathways Diagnosed from Particle Tracking

4.1 Abstract

Regional connectivity is important to the global climate salinity response because salinity anomalies are undamped by atmospheric fluxes and may therefore be advected over long distances by ocean circulation. This results in non-local influences on the salinity response. Here we use two types of Lagrangian particle tracking experiments to investigate these pathways. The first uses forward trajectories and broadly defined hydrologic regions to obtain estimates of the average transport timescales between water cycle regimes. The second uses reverse trajectories and a freshwater accumulation method to generate detailed estimates of remote influences in the salinity response. Additionally, we compare velocity fields with both resolved and parameterized eddies to understand the impact of eddy stirring on intergyre exchange.

4.2 Introduction

As shown in Chapter 2, the salinity response to climate warming does not only reflect local freshwater flux anomalies. The patterns of change are also influenced by remote freshwater forcing, because salinity anomalies are not damped by atmospheric fluxes and can persist along circulation pathways.

An interesting aspect of the salinity response seen in CMIP5 is that freshwater flux trends

of different sign become relatively well mixed within the subtropical latitudes ($\Delta E - P > 0$ in the subtropics and $\Delta E - P < 0$ in the tropics). Between the subpolar gyres (SPG) and subtropical gyres (STG), there is strong contrast in the salinity change (particularly in the Atlantic, see Fig. 2-3), indicating a transport barrier. We hypothesize in Chapter 3 that surface Ekman transport acts to quickly disperse additional freshwater input in the ITCZ and return anomalously salty water from the subtropics via the subsurface return branch of the shallow subtropical cell, effectively mixing these signals. In contrast, the subpolar gyre is isolated from the subtropics by the intergyre boundary.

However, a subset of CMIP5 models show a positive salinity change across much of the subpolar North Atlantic despite increased local freshwater input. This can only be due to the transport of salty water poleward from the subtropical gyre, pointing to a potential difference in advective intergyre transport between the models. A similar trend of Atlantic SPG salinification is seen in the observational estimate of Durack et al. (2012). These uncertainties motivate a need to better understand the pathway history of surface water masses, and to identify mechanisms and rates of intergyre exchange.

Observational quantification of Lagrangian pathways over decadal and longer timescales are limited. Surface drifters in the Atlantic show very weak exchange between the STG and SPG (Brambilla and Talley, 2006), because the true pathways of intergyre exchange are three-dimensional (Burkholder and Lozier, 2011; Foukal and Lozier, 2016), requiring observations of subsurface flows. Here we explore these pathways using a series of particle tracking experiments in ocean models.

4.3 Methods

Rather than attempting to assess the subtle differences in advective exchange between individual CMIP5 models, we seek to understand general properties of the circulation that affect oceanic exchange. For this reason, we step back from coupled simulations and consider a simplified version of the problem, which is to take the ocean circulation as constant and investigate how freshwater flux anomalies propagate through it. This approach is reasonable so long as other climate factors such as winds and temperature do not have $O(1)$ changes on the circulations, and so long as the accumulated salt anomalies do not become large enough to significantly change circulations themselves. These criteria are generally valid for

present-day centennial climate projections, except for perhaps in the AMOC where there is a possibility for 50% or greater change over the coming century, in which case the analysis is valid until the non-linear advective feedbacks of the AMOC become significant.

4.3.1 Data Sources

For a "best guess" at the present-ocean circulation, we take velocity fields from two modern data-assimilated ocean models, namely the Simple Ocean Data Assimilation (SODA) Version 3.4.1 (Carton et al., 2018) and Estimating the Circulation and Climate of the Ocean (ECCO) Version 4.3 (Forget et al., 2015). These velocity fields are used to produce large ensembles of trajectories used in the experiments here.

ECCO assimilates a wide range of in-situ and satellite measurements using the MITgcm over the period 1992-2016. It is run on an Arakawa C-grid in lat-lon cap geometry with nominal 1° horizontal resolution and 50 vertical levels. ECCO uses the GM parameterization for mesoscale eddies, the GGL (Gaspar et al., 1990) mixed-layer closure, and the Redi (1982) scheme for isopycnal diffusion. ECCO is similar in resolution and parameterizations to most CMIP5 models. We use the rectilinear 0.5° interpolated velocity fields for producing trajectories.

SODA also assimilates many in-situ and satellite measurements, and the version 3.4.1 used here incorporates atmospheric forcing from the ERA-Interim reanalysis for the period 1981-2015. It is run on the GFDL MOM2.5 ocean model (Delworth et al., 2011), which utilizes a tripolar Arakawa B-grid with 0.25° horizontal resolution at the equator, increasing to 0.1° at the poles, and 50 vertical levels. We use the native B-grid output for trajectories south of 65° N, and interpolate the tripolar fields to a rectangular grid north of this point.

SODA does not utilize any mesoscale eddy parameterization such as GM, but uses the sub-mesoscale closure of Fox-Kemper et al. (2011) and the KPP (Large et al., 1994) vertical mixing scheme. SODA also does not apply any background lateral or vertical diffusion. SODA can be considered eddy-permitting nearly everywhere. The increased resolution at high latitude allows for grid spacing near half the 1st baroclinic Rossby radius of deformation, which is required to represent classical mesoscale eddies. The underlying MOM2.5 ocean model has realistic patterns of enhanced eddy kinetic energy in the deep tropics, western boundary currents, and frontal zones, but is somewhat less energetic everywhere when compared to altimeter observations or higher resolution configurations of MOM (Delworth

et al., 2011). Additionally, we use a monthly climatology of the SODA model as a field with no representation of eddies at all, since transient features are filtered out by taking a temporal mean of the velocity fields.

Trajectories are produced from 5-day averaged SODA velocities. Averaging timescales up to 9 days have been found to produce accurate trajectories within a mesoscale flow (Qin et al., 2014). ECCO trajectories are produced from 30-day averaged velocities, which is sufficient because the coarse resolution flow contains much less transient variability on sub-monthly timescales.

We also use output from the RCP8.5 scenario of the CMIP5 ensemble over the period 2006 to 2100 to obtain a multi-model mean anomalous freshwater flux trend to apply to the trajectories as a passive salinity tracer, taken from the CMIP5 variable wfo (water flux into ocean). For the basin-integrated freshwater forcing tendencies shown in Fig. 4-3, we use the CMIP5 variables *evspbl* and *pr*, using fluxes over ocean and land areas divided by drainage basins (as in Chapter 2) to avoid errors due to regridding of the river flux inputs. All CMIP5 values are given as a multi-model mean of the models listed in Table 4.1. For the basin-wide forcing tendencies, the error bars are given as the standard deviation between models.

4.3.2 Particle Advection Scheme

Trajectories are generated with an offline advection model utilizing the Runge-Kutta 4th order (RK4) time-stepping scheme. The local velocity for each particle is determined through a trilinear interpolation of the three-dimensional velocity fields in space and a linear interpolation between each time-step of the model output. Particle positions are calculated at 1-hour time steps and stored every 5 days. The particle tracking software used here was built from scratch to obtain fast computation time for the 100-year trajectories required in this analysis by making use of GPU parallelization. The tracking algorithms were tested favorably against existing software packages such as PARCELS (Lange and van Sebille, 2017).

Several processes that are effectively sub-grid scale or otherwise parameterized in an Eulerian model must be handled within the offline advection scheme in addition to the standard model velocity outputs in order to obtain realistic particle behavior.

The first of these is vertical motion within the SML. In the Eulerian frame, the energetic

stirring and vertical transport of tracers within the SML is parameterized by KPP or other closure schemes. To represent this transport in terms of Lagrangian particles, we apply a simple displacement of the particle positions at regular intervals whenever the particle is found to be within the SML defined by a density criterion of $\rho_z - \rho_0 > 0.03\,\mathrm{kg\,m^{-3}}$, which generates a random walk for particles within the SML. The interval for displacements is chosen to be once per day, which limits vertical motions even in deep SMLs to $O(0.1\,\mathrm{m\,s^{-1}})$ which have been observed in convective plumes (Lavender et al., 2002), but allows for frequent motions within the SML on the timescale of resolved mesoscale features. This scheme does not provide any diapycnal transport of particles across the SML base.

Another issue associated with sub-grid motions is the treatment of particles within the boundary cells of the model. If particles cross the boundary cells, they become stranded outside the domain. To avoid stranding, we apply a no normal flow boundary condition when a particle reaches the edge of the domain, such that particles will continue to move along the cell boundary if there is a non-zero velocity component in the remaining dimensions.

The ECCO model uses the GM scheme to parameterize the effects of mesoscale eddies as an advective residual-mean velocity. To capture this behavior in trajectories, the additional GM velocity term is simply added to the Eulerian velocities during particle advection, mimicking the transport of tracers in the Eulerian model.

Other sub-grid mixing parametrizations, such as the isopycnal Redi (1982) scheme, do not have a direct advective analog that can be applied to trajectories. A common procedure is to apply an additional stochastic velocity to create particle spreading which mimics the tracer diffusion of these terms. We use a first-order Markov model (van Sebille et al., 2018), which applies a random velocity at each time step as $u_{diff} = \sqrt{\frac{\kappa_{Redi}}{\Delta t}}$, where κ_{Redi} is a diffusivity and Δt is the advective timestep. We vary the diffusivity to test the effects of isopycnal stirring strength.

In order to sample the annual and interannual variability of the flow fields used, particles are launched monthly over a period of 5 years. Launch locations are randomly generated within 1° grid cells. The number of particles used in the global salinity accumulation experiments is 1.5×10^6.

Because the ECCO and SODA outputs used here only extend for 25 to 35 years, longer trajectories must be looped through the model output multiple times. This is a common technique for particle tracking over long timescales and other authors have found limited

impact on bulk results (van Sebille et al., 2018). For 100-year trajectories, the looping induces 2 to 3 discontinuities in the velocity fields. These velocity jumps may induce erroneous spreading across the flow regimes of interest. For example, a subtropical particle following a northwards Gulf Stream meander may suddenly appear on the poleward side of the subtropical front as the velocity field switches. To test the importance of this effect, we compare the SODA run with 2 discontinuities to one in which the model output years are randomly rearranged, so that the velocity field has a jump every year (100 total). Even for this large number of discontinuities, we find that the subtropical to subpolar exchange timescale decreases by only 10% and conclude that a small number of loops has a minimal effect on the analysis.

4.3.3 Transport Timescales

To understand the exchange of freshwater signals between different hydrologic regimes, we launch an ensemble of 1.0×10^6 particles evenly distributed across the global ocean surface layer at 5 m depth. We analyze exchange by defining broad regions corresponding to the sign of freshwater forcing change under water cycle intensification, and measure the average transit properties of all particles launched in each region. For the subtropical regions, we take the poleward edge to be the intergyre boundary, defined as a surface of constant mean dynamic topography within the model outputs (as in Zou and Lozier, 2016), for which streamlines immediately equatorward (poleward) of the contour recirculate in the STG (SPG). We choose this definition rather than the $E-P=0$ contour (which lies slightly equatorward of the intergyre boundary) because many subtropical particles will repeatedly cross the $E-P=0$ line but then recirculate into the STG. The tropical regions which see increased net precipitation do not have an obvious dividing contour based on circulation, so we choose a simple latitude band of 5°S to 10°N to represent the waters freshened by increased ITCZ rainfall under water cycle intensification.

A cumulative transport function is produced by identifying the first instance when a particle crosses into a region other than its origin and remains there for at least two months. The residence time requirement eliminates false crossings where particles continue to follow geostrophic streamlines which recirculate at the intergyre boundary, but temporarily cross the fixed boundary line due to transient meanders. Once a particle has met this threshold, it does not add to the transport if it crosses the boundary again.

4.3.4 Trajectory Histories and Accumulation of Salinity Anomalies

To quantify the influence of regional connections on salinity changes, we calculate an average forcing history for a large ensemble of reverse trajectories. Because a water parcel is directly affected by surface fluxes only when it is within the SML, we define a metric $\alpha_{l,t}$ which produces a map of the relative geographic influence for water parcels from a particular launch location l and for trajectories of length t:

$$\alpha_{l,t}(x,y) = \left\langle \int_0^t \frac{H(z)}{h}\, dt \right\rangle \tag{4.1}$$

where $H(z)$ is a Heaviside function which is nonzero only when the particle depth z is within the SML, h is the SML depth, the integral is over all trajectories, and the brackets indicate that $\alpha_{l,t}$ is normalized so that the global integral sums to one. The influence is inversely proportional to h because a given surface flux has a weaker effect on tracers when distributed through a deeper mixed layer.

To relate FWF anomalies to salinity change, we accumulate the salinity anomaly as a passive tracer along trajectories. In our model, a water parcel is affected by anomalous FWF any time it is within the SML, with the anomaly evenly distributed across the thickness of the layer. Parcels accumulate forcing along the length of their trajectories with no decay, such that the net salinity change for a particle launched at location l and for trajectories of length t can be calculated as:

$$\Delta S_{l,t} = \oint \frac{S_0 \cdot \Delta FWF(x,y,t) \cdot H(z)}{h}\, dt \tag{4.2}$$

where S_0 is a reference salinity of 35 psu, ΔFWF is an expected freshwater flux anomaly for the particle location, h and $H(z)$ are the same as above, and the integral is calculated along individual particle trajectories. This quantity can then be binned over an ensemble of trajectories to estimate a salinity change everywhere that represents the many possible paths of constituent particles.

In order to compare the Lagrangian passive tracer method to coupled model results from CMIP5, we take ΔFWF to be the multi-model mean change in the variable wfo from RCP8.5 and apply this field to the trajectories. We produce a monthly trend anomaly map by fitting a linear regression to each of the twelve months for 28 models and averaging the models together. We take the anomaly to be zero in the year 2000 and fit a trend

to the period 2006 to 2100. The actual time-dependent forcing change across the models is well approximated by a linear function. Using this methodology, the salinity anomalies accumulated near the beginning of the 100-year trajectories (where particles are generally far away from the launch site) are weak, and the anomaly strength increases toward the end of the trajectories (where particles are close to their launch site).

The passive tracer framework makes several assumptions, namely 1) that salinity anomalies do not generally feedback on circulation or surface fluxes, so that the trajectories may be decoupled from salinity changes, and 2) that particles maintain their accumulated salinity anomalies indefinitely. Previous studies have tested passive tracer methods using a stable circulation in Eulerian models to track temperature change signals, which show good performance, for example, in predicting the propagation of present-day anthropogenic temperature (Marshall et al., 2015), and in attributing ongoing cooling in the deep Pacific to surface heat loss during the Little Ice Age (Gebbie and Huybers, 2019). Because salinity does not directly feedback on surface freshwater fluxes, it is likely a better passive tracer than temperature which does feedback on heat fluxes. The assumed stationary of the circulation is a limitation of this method, and the AMOC in particular is likely to undergo large $O(1)$ changes over the 21st century. Regarding the second assumption, our Lagrangian model does allow for subduction and reemergence of anomalies, but does not account for dissipation of those anomalies in the interior. Because of the large scale coherence of the forcing pattern in space and time, we expect the interior dissipation of anomalies to be less important than for smaller scale anomalies, such as those forced by interannual climate variability (Dickson et al., 1988). But given that some of the anomalies will mix with adjacent subsurface layers which do not reemerge, the results can be considered an upper bound on the importance of remote influences.

4.4 Results

4.4.1 Exchange Timescales Between Tropical, Subtropical, and Subpolar Regions

An important measure of the intergyre circulation is the time taken for a typical subtropical parcel to reach the SPG. Fig. 4-1 shows an experiment where particles are launched evenly at the surface across the latitudes of the Intertropical Convergence Zone (ITCZ, 5°S-10°N)

and the northern STG (10°N to the intergyre boundary) in both the Atlantic and the Pacific. The center panels indicate the cumulative transit time for northern STG particles to reach the SPG, and the right panels shows the time for ITCZ particles to reach either northern or southern STGs.

We calculate the time τ_{50} at which a majority (50%) of particles have cumulatively transited from the origin to the destination region. The transit times show that ITCZ waters spread rapidly into the subtropics, with $\tau_{50} < 1\,\text{yr}$ for all experiments in both Atlantic and Pacific. This timescale is insensitive to eddy representations, as the circulation is dominated by the Ekman-driven subtropical cell.

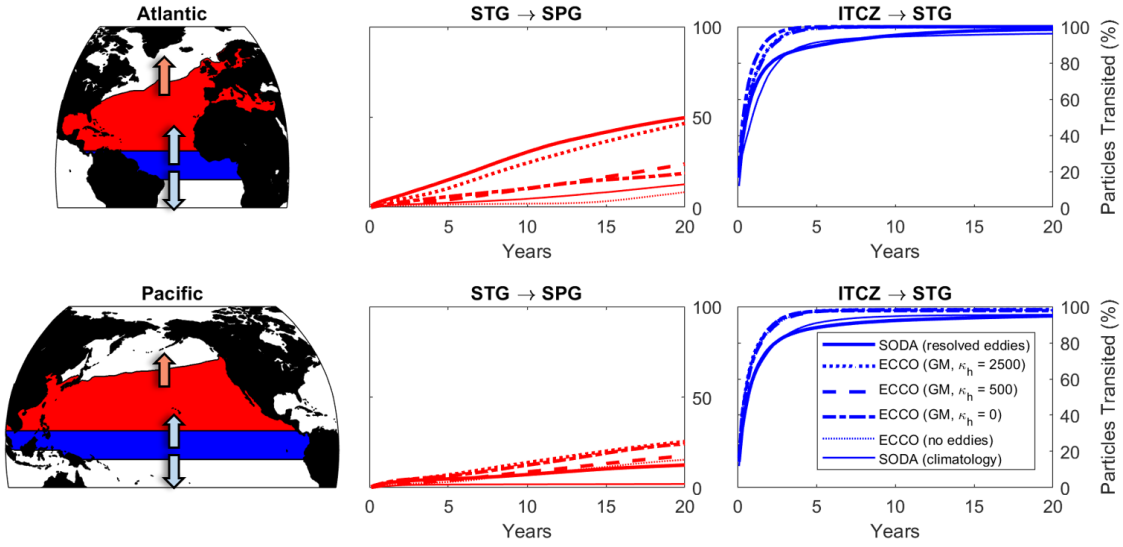

Figure 4-1: Particle tracking experiment depicted in (A), where 4×10^5 particles are evenly launched across the subtropical gyre (red) and ITCZ (blue) regions (as defined in the text) and advected forwards in time. We calculate the cumulative transit function (as a percent of the total particles launched) for (B) subtropical parcels to spread northwards into the subpolar gyre and for (C) ITCZ parcels to spread into either northern or southern subtropical gyres, with trajectories calculated using different eddy representations. The ITCZ spreading time is insensitive to eddy representations, while the STG spreading is highly dependent on eddy stirring.

The subtropical to subpolar exchange is much slower. In the Pacific, $\tau_{50} > 100\,\text{yrs}$ for all experiments. The exchange is negligible without eddy stirring, because there is nearly no mean meridional circulation across the intergyre boundary in the Pacific. For the Atlantic, using the non-eddying climatology version SODA, where particles only cross the gyre boundary via steady circulations, $\tau_{50} = 83\,\text{yrs}$. For the ECCO model without any eddy representations, the result is similar with $\tau_{50} = 74\,\text{yrs}$. Including the ECCO GM

velocities reduces the timescale only slightly to $\tau_{50} = 71\,\text{yrs}$. In the eddying SODA model, $\tau_{50} = 20\,\text{yrs}$, which again suggests that eddy stirring increases intergyre exchange.

To test this, we apply an additional stochastic velocity term $\mathbf{u_s}$ to particles advected in ECCO. This velocity approximates the effects of the Redi scheme in the Lagrangian frame (van Sebille et al., 2018). We calculate the exchange timescale for trajectories with both the GM velocities and a weak diffusivity ($\kappa_{Redi} = 500\,\text{m}^2\,\text{s}^{-1}$) or a strong diffusivity ($\kappa_{Redi} = 2500\,\text{m}^2\,\text{s}^{-1}$), which gives $\tau_{50} = 44\,\text{yrs}$ and $\tau_{50} = 22\,\text{yrs}$ respectively. With a large enough diffusivity, the simple random walk model can approximate the intergyre spreading effect of resolved mesoscale eddies.

These results indicate that the speed of intergyre exchange is highly dependent on the isopycnal stirring effect of eddies and only weakly affected by the residual mean circulation represented by GM. The Eulerian mean circulation of the AMOC sets a baseline exchange timescale of $O(100\,\text{yrs})$ for STG waters to reach the SPG. The isopycnal diffusion of eddies, which allows waters to cross divergent streamlines at the intergyre boundary, can reduce this exchange timescale to $O(20\,\text{yrs})$. The Pacific SPG has much weaker connectivity due to the lack of an overturning circulation (see Fig. 4-8)

4.4.2 Pathway History and Freshwater Accumulation

Fig. 4-2 summarizes the freshwater flux and salinity changes in CMIP5, and the results of accumulating the CMIP5 freshwater flux anomalies along 100 years of reverse trajectories launched globally in SODA. The summed salinity change is calculated along each trajectory of an ensemble of 1.0×10^6 particles released evenly across the ocean surface, and then averaged by launch location into 2° bins.

The results show a striking similarity to the surface salinity changes in CMIP5. As in the coupled models, large freshwater input across the Pacific ITCZ is well distributed into the northern and southern Pacific STGs, balancing the impact of local evaporation. Similarly, in the Atlantic ITCZ the weaker increase in freshwater input there is overwhelmed by connectivity with the STGs which become much more evaporative, and the Atlantic ITCZ becomes saltier. In the experiment shown here, which uses the eddying SODA velocities, the Atlantic SPG shows much weaker freshening or increased salinites relative to CMIP5.

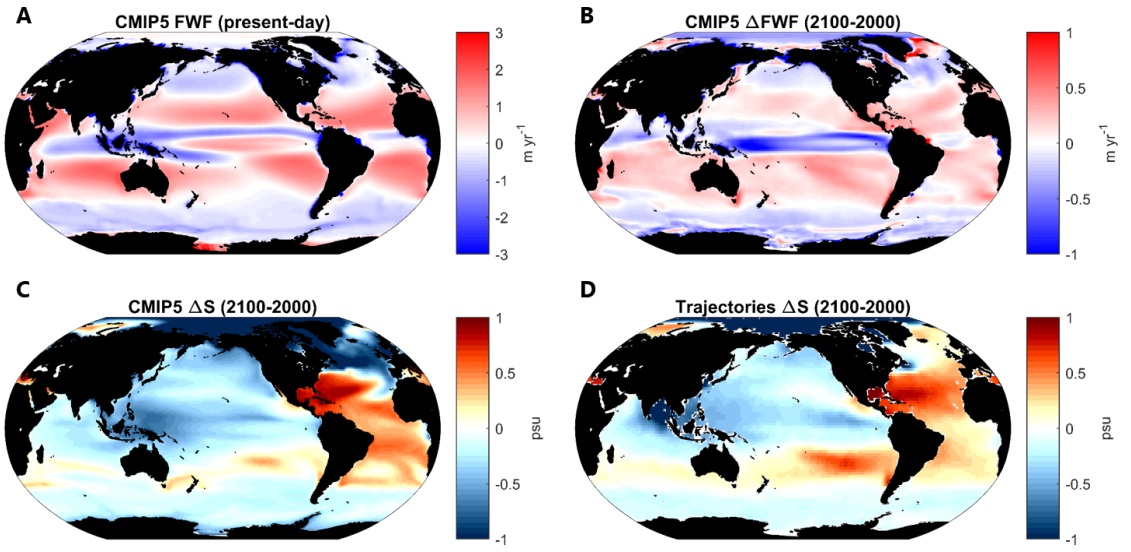

Figure 4-2: (A) Present-day FWF ($\mathrm{m\,yr^{-1}}$, positive defined as out of the ocean) for the years 1990 to 2000 based on an ensemble mean of 28 CMIP5 historical runs, (B) 100-year change (2100 to 2000) in FWF for the RCP8.5 scenario, (C) 100-year change in surface salinity (psu) from the RCP8.5 scenario of the same 28 CMIP5 models, and (D) accumulated salinity changes along present-day circulation pathways, by applying ΔFWF from CMIP5 to 1.5×10^6 reverse trajectories produced from SODA. The passive tracer technique closely matches the coupled models everywhere except in the Atlantic subpolar gyre, as explained in the text.

4.4.3 Competing Forcings in the North Atlantic

In this section, we focus on the accumulation of salinity anomalies in the North Atlantic for several reasons. One is that the North Atlantic is a region with of large-magnitude salinity changes in CMIP5, with approximately 1 psu freshening for the SPG and 1 psu salinification for the STG in the multi-model mean of RCP8.5. This makes for strongly contrasting signals across the intergyre boundary, whereas in the Pacific the contrast is much weaker because a large increase in ITCZ freshwater input dilutes the salinification signal in the subtropics. Despite the large magnitude of the changes, there is poor agreement between models on the sign of the change in the SPG, particularly on the eastern side. The other motivation is the role of mean salinity in preconditioning subpolar surface waters for deep convection in the AMOC, which is thought to be an important reason why deep overturning occurs in the North Atlantic but not the North Pacific (Ferreira et al., 2018).

Across CMIP5 models, greenhouse gas forcing causes an amplification of atmospheric moisture transports from the Atlantic to the Pacific (Richter and Xie, 2010; Levang and

Schmitt, 2015), with an additional $0.33 \pm 0.08\,\mathrm{Sv}$ ($1 \times 10^6\,\mathrm{m^3\,s^{-1}}$) exported across the subtropical and tropical latitudes (Levang and Schmitt, 2015). In the subpolar and Arctic regions, the Atlantic drainage basin sees an additional $0.15 \pm 0.03\,\mathrm{Sv}$ import of freshwater via the atmosphere (Fig. 4-3). The net freshwater loss from the Atlantic (north of the Southern Ocean) is $0.18 \pm 0.08\,\mathrm{Sv}$.

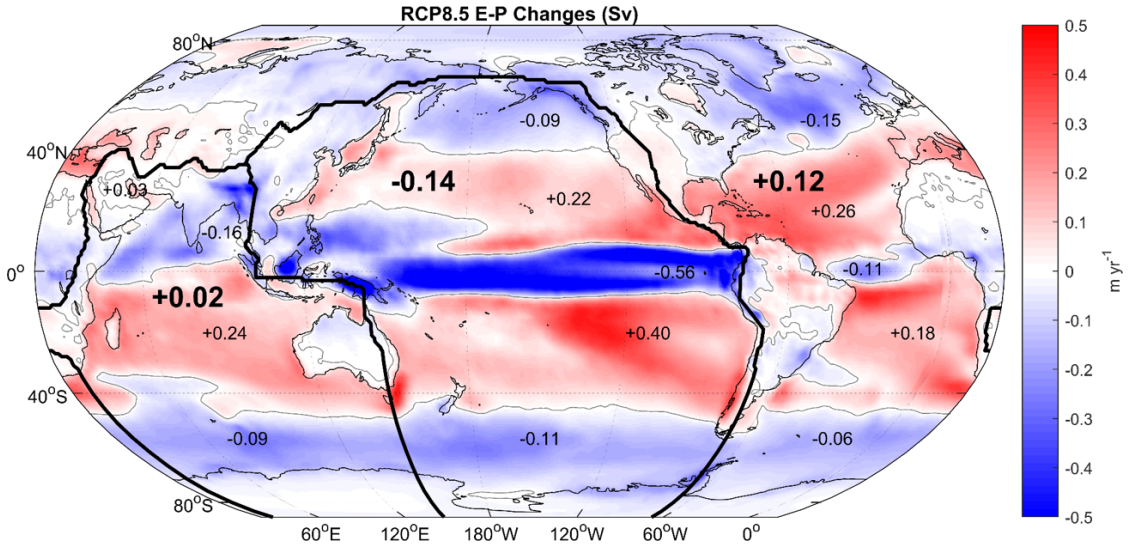

Figure 4-3: 100-year RCP8.5 changes in evaporation minus precipitation ($E - P$), plotted in color as $\mathrm{m\,yr^{-1}}$. Integrated values are also given in Sv ($1 \times 10^6\,\mathrm{m^3\,s^{-1}}$) for changes in each of the three ocean basins (large font) as delineated by drainage divides (thick black lines). Further values are provided (small font) for sub-regions as delineated by the zero contours of change (thin black lines).

The atmospheric response sets up a competition between local freshwater input to the SPG and broad-scale freshwater loss from the Atlantic basin as a whole. The influence of the latter depends on the propagation timescale of subtropical waters to the SPG. In the Atlantic, the mean northward upper-level flow of the AMOC works to drive a steady transport from the STG to the SPG. The intergyre boundary is also a region with high mesoscale energy due to the meandering North Atlantic Current (Zhurbas et al., 2014). Hence, transient eddy flows also drive significant exchange across this interface (Bower, 1991), as seen in Chapter 4.4.1.

Although CMIP5 models do not contain active ice sheet dynamics, several studies have used outputs from CMIP5 in downscaled regional ice models, and estimated Greenland meltwater fluxes to be 0.01 Sv to 0.05 Sv for the end of the 21st century (Vizcaíno et al., 2013; Lenaerts et al., 2015; Yoshimori and Abe-Ouchi, 2011). Hence, the expected freshwater

forcing from atmospheric fluxes and river runoff exceeds that from glacial melt by at least a factor of 3, although meltwater fluxes may be better localized to freshen deep convection sites. Since glacial melt is not resolved in the CMIP5 experiment, we do not include it here.

4.4.4 Salt Transport in the Subpolar North Atlantic

Fig. 4-4 shows the reverse trajectory accumulation experiment in the North Atlantic carried out for both the eddying SODA model and the SODA climatology with eddies removed. The accumulation of freshwater anomalies is plotted at different timesteps moving backwards from the year 2100 to show the role of remote influences over time. The trajectory technique captures the response of the STG and Arctic well when compared to CMIP5, but does underestimate the freshening of the SPG, even without eddies. This is in part due to the lack of salt-advection feedback, which reduces the northward flux of salt into the SPG in the coupled models. The trajectories may also underestimate the spreading of runoff input from coastlines, as it is difficult to precisely locate river sources when interpolating the FWF fields from CMIP5 onto other model grids.

For recent history of surface parcels (2 years) local freshening dominates the SPG, except for a small region of higher salinities in the Nordic Seas which are due to retreating sea ice margins and decreased sea ice melt. When the trajectories are traced backwards over decadal and longer timescales, the integrated forcing of the eddying and non-eddying models diverges for the SPG (see Fig. 4-4D). With eddy stirring included, many of the parcels traced backwards from the SPG have crossed the intergyre boundary from the STG and accumulated the higher evaporation there. This effect results in 0.3 psu higher salinities in the SPG by the year 2100 between the runs with and without eddies. The majority of the forcing is absorbed over the last 50 years, both because the forcing is treated as a linear trend which goes to zero at the end of the reverse trajectories, and because particles are less likely to be found in the SML as they are traced back in time.

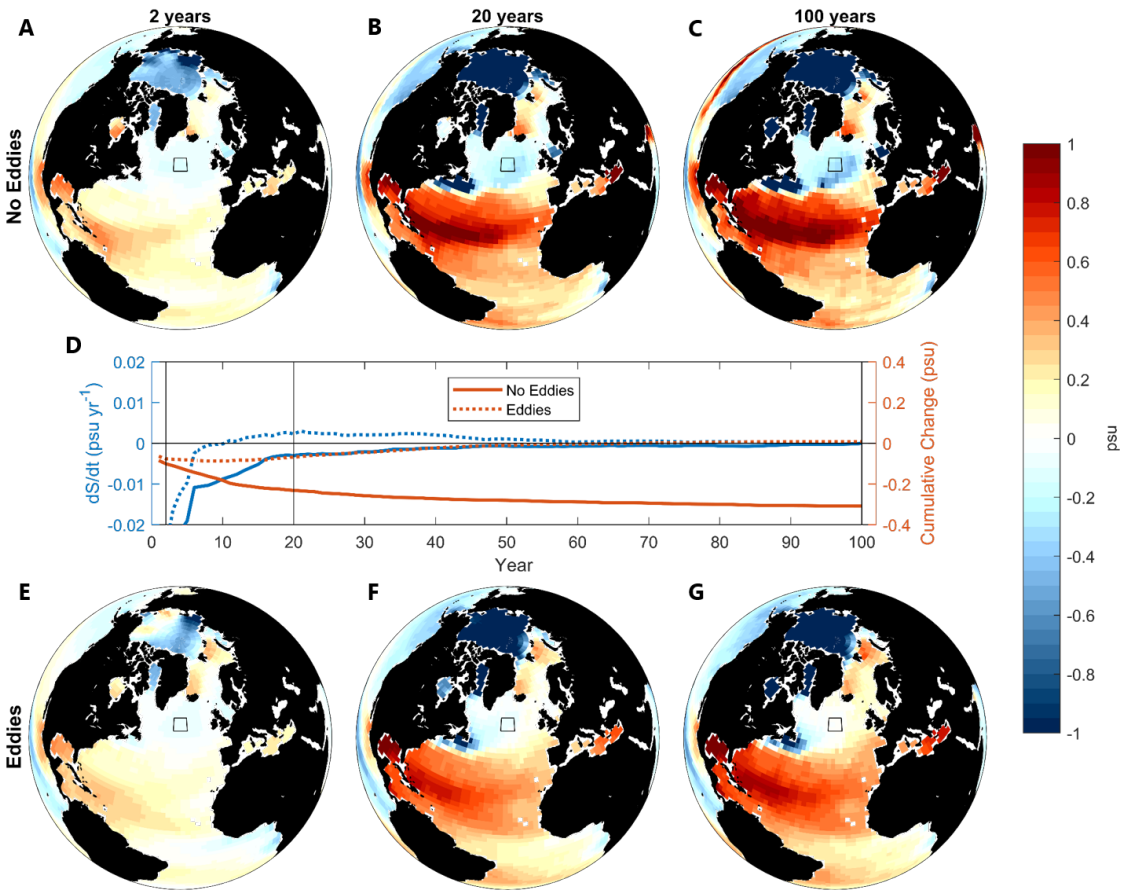

Figure 4-4: Maps of salinity change in the North Atlantic, produced by integrating the CMIP5 FWF forcing backwards along trajectories from the year 2100. Maps are calculated for forcing absorbed over (A,E) the final 2 years (2098 to 2100) of the trajectories, (B,F) 20 years (2080 to 2100), or (C,G) for 100 years (2000 to 2100). The upper maps use the SODA climatology without eddies, and the lower use the eddying SODA model. (D) Detailed plot of the salinity forcing absorbed by parcels traced back from a subpolar region near 40°W 55°N (black box), including the cumulative integral of the forcing (red lines) and the instantaneous rate of change at each year (blue lines). Vertical black lines denote the times at which the maps (A-C, E-G) were produced. For recent history of surface parcels (2 years) local freshening dominates in the subpolar gyre, but when eddy stirring in included, subpolar parcels begin to feel the influence of subtropical salinification within a decade. For 2000 to 2100, the salinity change in the SPG is 0.3 psu saltier with eddies than without.

We also use reverse trajectories to investigate in detail the pathway history of surface waters in the deep water formation (DWF) sites. Fig. 4-5 shows the geographic influence of surface forcing on particles launched in the Labrador Sea and the Nordic Seas using the metric $\alpha_{l,t}$ described in Eq. 4.1, traced backwards for 100 years. These locations were chosen as the maxima of March SML depth in SODA, where the strongest deep convection occurs. It is clear that eddies greatly enhance the connectivity between the deep convection sites and

the subtropical Atlantic. In the eddying flow 51% of particle surface history occurs south of the SPG for the Labrador Sea waters, while this is only 9% in the non-eddying flow. The maps show that the Labrador Sea is generally better connected to the subtropical Atlantic than the Nordic Sea, which is fed more at the surface by Arctic waters.

Fig. 4-5 was produced by launching 60,000 particles in 1° boxes centered on 53°W, 58°N and 1°W, 75°N, the locations of maximum winter SML depth in the SODA model. The metric $\alpha_{l,t}(x, y)$ is calculated in 1° bins by summing together all trajectories for each launch location and normalizing.

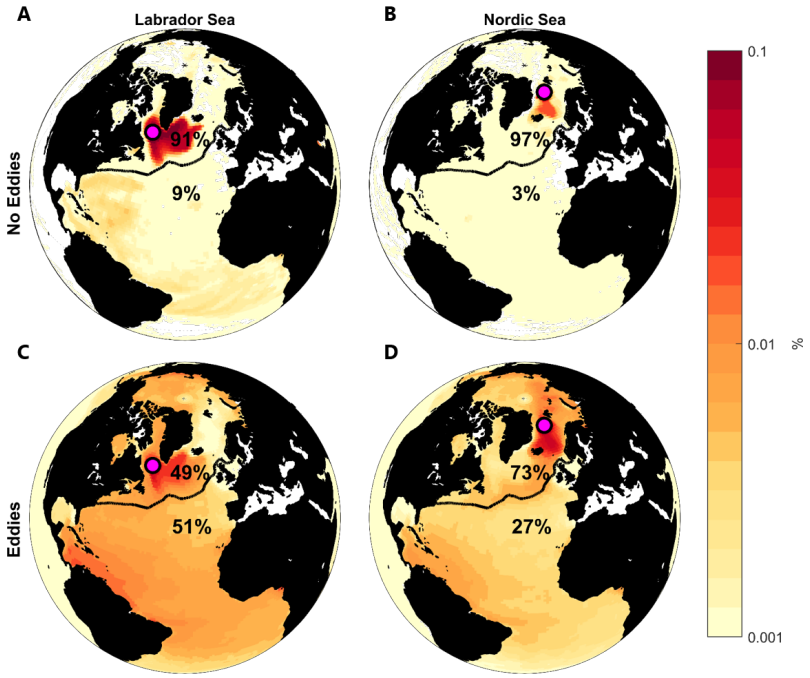

Figure 4-5: Maps of the 100-year surface history α_{100} (see Methods) from 6×10^4 reverse trajectories for two launches sites in the North Atlantic. The locations (pink markers) were chosen in the Labrador Sea (A,C), and the Nordic Sea (B,D) as local maxima of wintertime mixed-layer depth, where the majority of deep convection and DWF occurs in SODA. Results are shown for the SODA climatology (A,B) and the eddying SODA model (C,D). The black line represents a continuous mean dynamic topography contour which divides the subtropical and subpolar gyres. The summed total influence from north (south) of this line is printed above (below) it. Eddies increase the relative influence of the subtropical Atlantic.

4.4.5 The Role of Isopycnal Mixing in the CMIP5 Salinity Response

Particle tracking experiments show that strong isopycnal mixing, either in the form of resolved eddies or a large Redi mixing term, works to carry salty subtropical water into the SPG in the climate warming response. In CMIP5, 17% of models analyzed here (5/28) show

a region of increased salinity within the SPG, particularly on the eastern side of the basin where subtropical water follows the NAC.

To investigate the hypothesis that isopycnal mixing at the intergyre boundary affects the SPG salinity response, Fig. 4-6 shows a comparison between isopycnal mixing coefficients in individual CMIP5 models and their subpolar salinity change. Mixing coefficients were extracted from the many publications describing individual model configurations as referenced in Flato et al. (2014). Mixing schemes with spatially varying coefficients are shown as a range, and where geographic maps were provided, the values are estimated by eye for the region of the North Atlantic intergyre boundary. Of the 5 models with the least freshening in this region, 4 of them have large κ_{Redi} in the range of 1000 to 4000 $\mathrm{m^2\,s^{-1}}$. All other models have $\kappa_{Redi} < 1200\,\mathrm{m^2\,s^{-1}}$ and display significant freshening in the eastern subpolar region.

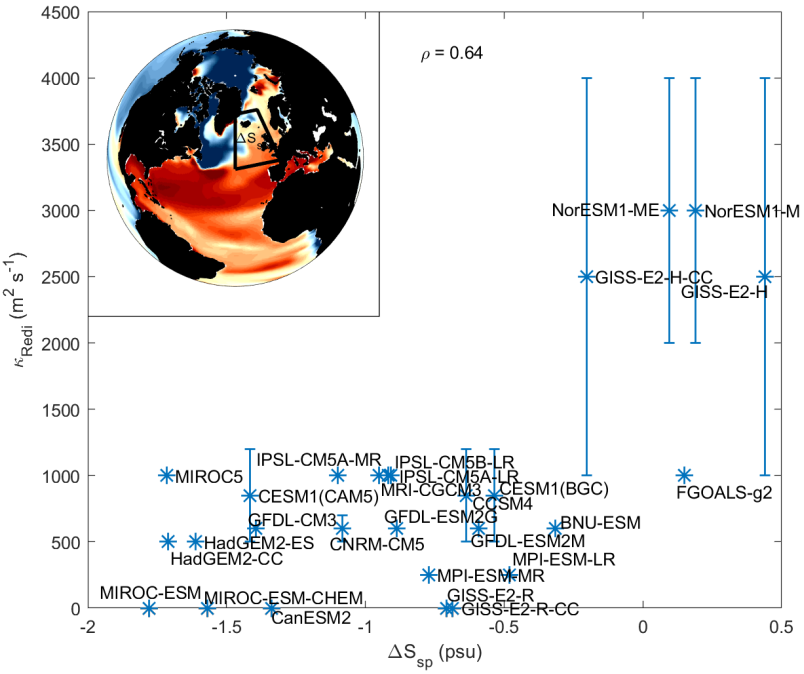

Figure 4-6: Scatter plot showing the isopycnal mixing strength κ_{Redi} versus the eastern subpolar SSS change ΔS_{sp} for 27 CMIP5 models. κ_{Redi} was estimated as available from model papers cited in Flato et al. (2014) and given as a range for spatially varying mixing schemes. The correlation coefficient is $\rho = 0.64$. The inset map shows the region over which the salinity change was calculated, and the change in one model (NorESM1-M) to illustrate the typical spatial pattern seen in the models that show subpolar salinification.

The comparison is difficult, as model resolution, numerical diffusion, and other issues also affect total isopycnal diffusion. The plot shows large scatter, as there are of course many

other factors influencing SPG salinity, such as the mean AMOC transport and details of the atmospheric water cycle response. However, stronger diffusion is significantly correlated with less freshening ($\rho = 0.64$), and the general relationship agrees with particle tracking results, where a mixing coefficient of $\kappa_{Redi} \approx 2500\,\mathrm{m^2\,s^{-1}}$ is necessary in the coarse ECCO flow to match the transport timescale of resolved eddies in SODA.

4.5 Implications for Deep Convection in the North Atlantic

The salinity response in the Atlantic SPG is of particular interest because of its effect on surface density in the DWF regions of the AMOC. Past literature suggests that deep convection in the SPG may be influenced by freshwater input to the DWF regions (i.e. Stouffer et al., 2006), which increases the buoyancy of surface waters and inhibits vertical mixing.

Under the classical water cycle intensification pattern imposed by climate warming, the SPG sees increased net precipitation while the STG sees increased net evaporation. In this scenario, we propose that eddy-driven salt transport can act to mitigate the buoyancy increase of SPG waters due to haline effects. By accelerating the intergyre transport of anomalously salty subtropical waters into the SPG, this lessens the effect of local freshwater input. Given the range of mixing parameterizations used in CMIP5 ocean models, this mechanism likely produces some of the uncertainty between model salinity responses.

4.6 Conclusions

Our results demonstrate that the advective transport timescale between different regimes of the global water cycle is key to understanding the climate salinity response. When the timescale of forcing change is slow relative to the exchange timescale, ocean circulation is able to mix together different regional forcing. Across the tropics and subtropics, the circulation is indeed very fast relative to present-day climate change, and the local salinity anomalies forced by water cycle intensification become mixed across these regions.

Between the subtropical and subpolar regions, the exchange timescale is much slower and largely driven by eddy stirring (Fig. 4-7), especially in the Pacific where no mean overturning circulation connects the gyres. In the Atlantic, we find that an eddying circulation transports a majority of subtropical surface waters to the SPG within 20 years, which may be considered

fast relative to centennial climate change. In a non-eddying flow, this timescale is a factor of 4 larger, which is slow relative to climate change. Therefore, we expect less mixing of the subtropical and subpolar salinity signals when eddy stirring is weak. Although the data are noisy due to other influences, we find some support in the CMIP5 experiment that models with stronger isopycnal mixing show less freshening in the Atlantic SPG due to this mechanism.

In the weak isopycnal mixing case where the intergyre exchange timescale is $O(100yrs)$, the salt advection feedback of the AMOC may activate well before any significant amount of salty subtropical water penetrates the SPG. In the strong mixing case, the intergyre salt exchange may counteract freshening in the SPG and help to support DWF.

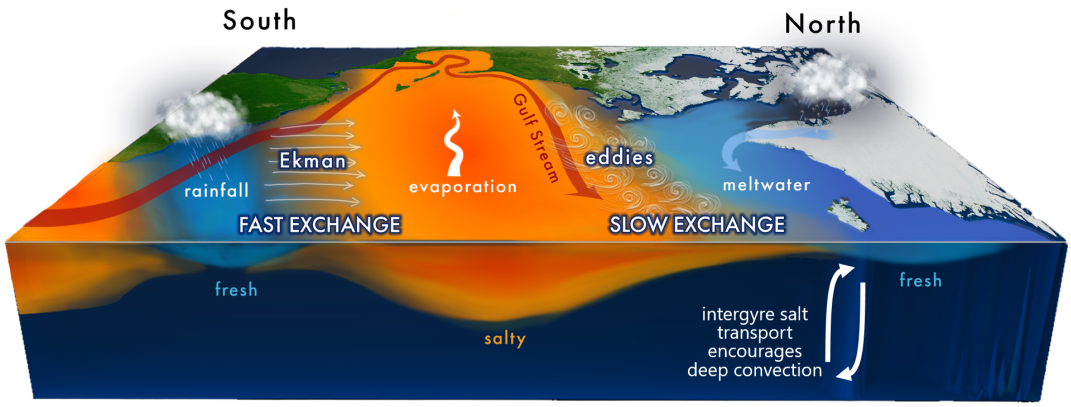

Figure 4-7: Amplification of the global water cycle under atmospheric warming increases net evaporation in the subtropics and increases net precipitation in the tropics and high latitudes (where meltwater input also increases). Locally, these fluxes induce a regular pattern of surface salinity anomalies which then propagate along ocean circulation pathways. The tropics communicate rapidly with the subtropical gyre via the shallow Ekman driven cells, while exchange between the subtropical and subpolar gyres is weaker. In a high resolution model, this transport is predominantly eddy-driven, with a majority of subtropical parcels transiting to the subpolar gyre on decadal timescales. This counters the impact of local freshening, potentially reducing the weakening of deep convection.

We reiterate that the trajectory accumulation method used here has limitations, as it ignores salt-advection feedbacks, interior mixing, and other nuances of the coupled simulations. Hence, salinity response maps shown in this study should not be taken as accurate projections for the coupled climate system. Rather, we use the technique to demonstrate that:

- treating salt as a passive tracer captures the first order dynamics of the 100-year

coupled response for most regions,

- intergyre exchange carries anomalously salty water northwards into the SPG under water cycle intensification,
- this exchange is greatly enhanced by the isopycnal diffusion of mesoscale eddies, which has widely varying strength in the coarse CMIP5 models, and
- evaporation in the STG has the potential to balance out a significant portion (0.3 psu in the experiments here) of local freshening in the SPG and AMOC deep convection sites under present-day warming scenarios.

These results also have important implications for numerical ocean model development. Different eddy mixing rates at the intergyre boundary can produce divergent climate responses in oceanic tracer fields when the forcing signal differs between the gyres, as it is for salinity. Here, the along isopycnal Redi term is shown to be particularly important in the North Atlantic. Many CMIP5-generation models use a simple constant Redi mixing rate between 500-1000 $m^2\,s^{-1}$. Observationally based estimates show that while these values may be appropriate for more quiescent regions such as the subtropical gyre centers, isopycnal mixing rates at the energetic intergyre boundary may be several orders of magnitude higher (Zhurbas et al., 2014; Abernathey and Marshall, 2013). Capturing this spatial variability of mixing in model parameterizations is evidently important to aspects of the climate response.

4.7 Chapter Acknowledgements

We acknowledge the World Climate Research Programme's Working Group on Coupled Modelling, which is responsible for CMIP, and we thank the climate modeling groups (listed in Table 4.1 of this paper) for producing and making available their model output. We also thank the creators of the SODA and ECCO reanalysis products. This work was supported by NASA Headquarters under the NASA Earth and Space Science Fellowship Program award 80NSSC17K0372. The SODA outputs used here can be accessed at http://www.atmos.umd.edu/∼ocean/, and the ECCO outputs at https://ecco.jpl.nasa.gov/. Data from the CMIP5 ensemble is available at https://esgf-node.llnl.gov/projects/esgf-llnl/. The particle tracking code used for these experiments can be found at https://github.com/slevang/particle-tracking.

4.8 Supplementary Material

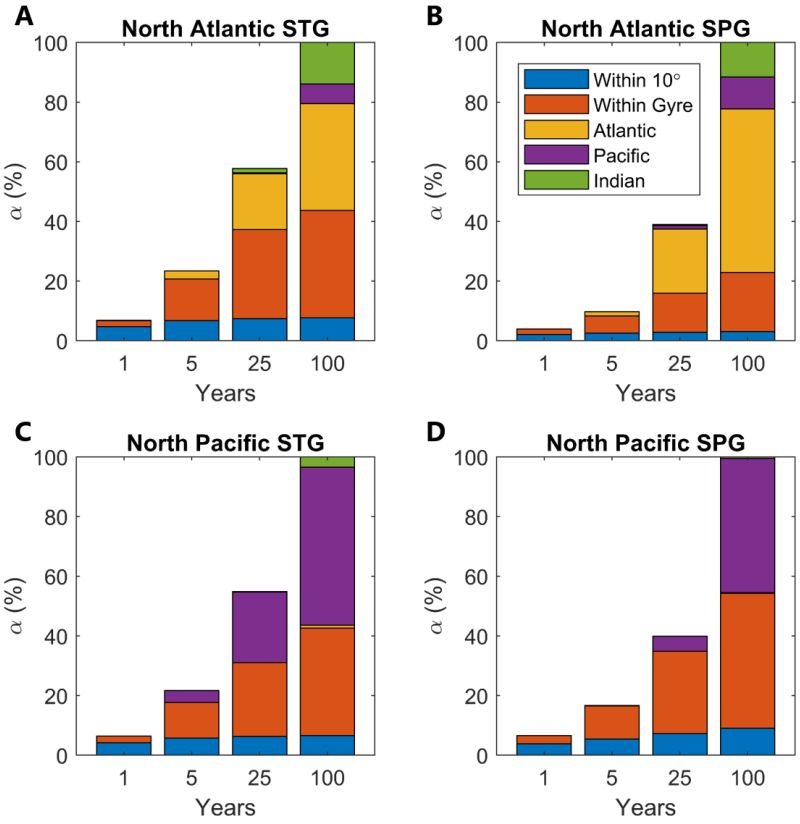

Figure 4-8: Breakdown of the surface history metric $\alpha_{t,l}$ in the eddying SODA model for waters traced from the (A) subtropical North Atlantic (40°W, 25°N), (B) subpolar North Atlantic (30°W, 60°N), (C) subtropical North Pacific (180°W, 25°N), and (D) subpolar North Pacific (180°W, 50°N). The breakdown of surface history is shown at $t = 1$, 5, 25, and 100 yrs, and integrated over regions including a 10° box surrounding the launch site, the remainder of the launch gyre, and the remainder of the three ocean basins (Atlantic, Pacific, Indian). It can be seen that the subpolar Atlantic surface develops significant connectivity with the rest of the Atlantic on decadal timescales, and connectivity with the other ocean basins on sub-centennial timescales. The subpolar Pacific is slower to develop connectivity with the rest of the Pacific, and has almost no connectivity to other ocean basins on centennial timescales. The enhanced connectivity of the Atlantic is due to the northwards surface flow of the AMOC.

Institute	Model	CMIP5 variables: evspsbl, pr, wfo
BCC	BCC_CSM1.1	X
BNU	BNU-ESM	X
CCCma	CanESM2	X
CMCC	CMCC-CM	X
CNRM–CERFACS	CNRM-CM5	X
ICHEC	EC-EARTH	X
INM	INM-CM4	X
IPSL	IPSL-CM5A-MR	X
CESS	FGOALS-g2	X
JAMSTEC	MIROC-ESM	x
JAMSTEC	MIROC-ESM-CHEM	X
JAMSTEC	MIROC5	X
MOHC	HadGEM2-CC	X
MOHC	HadGEM2-ES	X
MPI_M	MPI-ESM-LR	
MPI-M	MPI-ESM-MR	X
MRI	MRI-CGCM3	X
NASA GISS	GISS-E2-H	X
NASA GISS	GISS-E2-H-CC	X
NASA GISS	GISS-E2-R	X
NASA GISS	GISS-E2-R-CC	X
NCAR	CCSM4	X
NCC	NorESM1-M	X
NCC	NorESM1-ME	X
NOAA/GFDL	GFDL CM3	X
NOAA/GFDL	GFDL-ESM2G	X
NOAA/GFDL	GFDL-ESM2M	X
NSF–DOE–NCAR	CESM1(BGC)	X
NSF–DOE–NCAR	CESM1(CAM5)	X

Table 4.1: List of CMIP5 models used in Chapter 4 for the variables evaporation ($evspsbl$), precipitation (pr), and freshwater flux into the ocean (wfo). The models used in creating each figure are listed in the table. Further details for each model may be found in Flato et al. (2014).

THIS PAGE INTENTIONALLY LEFT BLANK

Chapter 5

The Role of Salinity in the AMOC Response to Warming

5.1 Abstract

The salinity structure of the Atlantic is important to the density gradients that drive the Atlantic Meridional Overturning Circulation (AMOC). This raises questions about how salinity changes due to water cycle intensification will affect the AMOC in a warming scenario. It has frequently been suggested that freshening of subpolar surface waters can weaken the AMOC by introducing positive buoyancy anomalies to the downwelling branch. However, these theories are often supported by an antiquated conception of an AMOC which is physically driven by deep convection.

Here we decompose the density changes in CMIP5 models into temperature and salinity components. In the warming scenario, these signals are forced at the surface and propagate into the deep limb of the circulation on decadal timescales. The AMOC is largely geostrophic on these timescales, and we analyze the circulation changes as a function of the thermal wind relationship.

This analysis reveals that in the subtropics, where the AMOC is strongest, weakening of the overturning is largely driven by warming in the deep layer along the western margin. In this same location, salinity changes are in fact slightly positive. This is a surprising result if waters in the Deep Western Boundary Current are thought to have subpolar surface origins, where the CMIP5 models freshen. However, a more thorough investigation of the subpo-

lar changes reveals positive salinity anomalies in the intermediate-depth waters, suggesting subtropical influences, and the depth-averaged profile has near zero salinity change. In the upper ocean, salty anomalies due to increased subtropical evaporation largely cancel the buoyancy changes due to warming. These results indicate that subtropical salinification is the main contribution of the water cycle to AMOC changes, rather than subpolar freshening, and that the salinity changes overall work to stabilize the AMOC against warming-induced weakening.

5.2 Introduction

Freshwater forcing has often been implicated in changes to North Atlantic deep water formation, both in paleoclimate records (Dansgaard et al., 1993; Broecker, 1994) and climate models (Stouffer et al., 2006). Sufficient freshwater input to the subpolar gyre (SPG) stratifies the ocean surface and inhibits deep convection, which is thought to induce changes in the overturning circulation throughout the Atlantic basin. The frequent invocation of this mechanism in general oceanographic literature stems from a persistent viewpoint of the AMOC as a "conveyor belt" (Broecker, 1991) driven by the "push" (Visbeck, 2007) of sinking dense waters at the surface. This perspective originated in early box models of the meridional circulation (i.e. Stommel, 1961) which described the overturning according to meridional density gradients. However, recent work has painted a more complex picture of the AMOC, where the energy for overturning is provided by tidal mixing and wind-driven upwelling in the Southern Ocean (Kuhlbrodt et al., 2007), and the connectivity between convection in the SPG and the overturning streamfunction further south in the basin is more tenuous (Lozier, 2010).

Although deep convection in the SPG does not mechanically drive the overturning cell, changes in surface properties of the SPG can still influence the broader AMOC through propagation in the deep limb. Observational (Molinari et al., 1998) and modelling (Sévellec and Fedorov, 2016) studies have identified connectivity between the SPG surface and the interior subtropics via the Deep Western Boundary Current (DWBC) which peaks at approximately 10 year timescales at 26°N. These buoyancy anomalies propagate southward along the DWBC, and because the AMOC is approximately in geostrophic balance on decadal timescales (Buckley and Marshall, 2016), temperature and salinity anomalies alter zonal

density gradients that drive the flow.

Using this perspective, we investigate the buoyancy anomalies induced by climate trends in the CMIP5 RCP8.5 experiment. Unlike in simple "hosing" experiments (Stouffer et al., 2006, i.e.), realistic warming scenarios are forced by complex coupled changes in both heat and freshwater fluxes. In these scenarios, the AMOC is projected to weaken, but the changes have large uncertainties (Reintges et al., 2017). To investigate these dynamics, we quantify the role of buoyancy anomalies due to both salinity (S) and temperature (T) changes, and the relative importance of water mass changes in the upper and lower limbs of the AMOC.

5.3 Salinity, Temperature, and AMOC Changes in CMIP5

To begin, we decompose 100-year global surface density changes in RCP8.5 by computing the relative contributions from both (S) and (T). An important point is that the thermal expansion coefficient α becomes small relative to the haline contraction coefficient β at low temperatures. Therefore, salinity generally has the largest impact on density in the high latitudes (see Fig. 1-3) and in the deep ocean, where waters are cold. To illustrate, for typical properties of North Atlantic Deep Water (NADW; $S = 35\,\text{psu}$, $T = 2\,^\circ\text{C}$), a 1 psu freshening has the same effect on buoyancy as a $7.7\,^\circ\text{C}$ warming.

To quantify the relative contributions from (S) and (T) in CMIP5, we define:

$$\begin{aligned} \Delta\rho_{Sfrac} &= \frac{\rho_{2000} \cdot \beta\Delta S - \rho_{2000}}{\rho_{2100} - \rho_{2000}} \\ \Delta\rho_{Tfrac} &= \frac{\rho_{2000} \cdot \alpha\Delta T - \rho_{2000}}{\rho_{2100} - \rho_{2000}} \end{aligned} \tag{5.1}$$

where ρ_{2000} and ρ_{2100} are the surface densities for the beginning and end of the 21st century, respectively, and ΔS and ΔT are the 100-year changes in temperature and salinity. The values are computed by fitting a linear regression over the RCP8.5 experiment and taking the endpoints, then averaging into a multi-model mean.

Fig. 5-1 shows the decomposition performed for the annual mean density changes, and for March and September, when the deepest convection occurs in the Northern and Southern hemispheres respectively. The models used are listed in Table 5.1. While temperature increases are the dominant contributor to surface buoyancy increases across most of the oceans, this is not the case in the high latitudes. In the subpolar Atlantic, Arctic, and the coastal margins of Antarctica, buoyancy changes due to freshening exceed those due to

warming. This is particularly true in winter, when α becomes small and warming has less effect on density. This suggests that salinity effects are likely leading-order for changes in deep water formation processes in the RCP8.5 scenario.

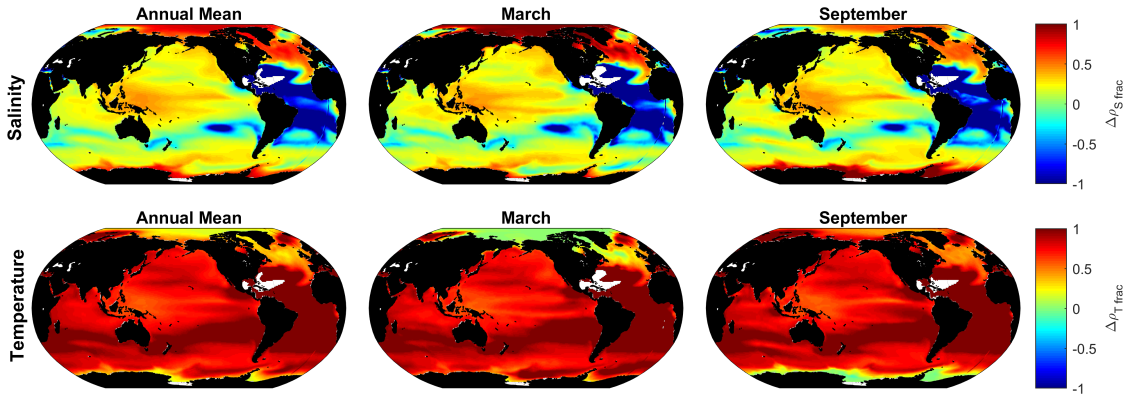

Figure 5-1: Decomposition of surface density decrease in CMIP5 (100-year change from RCP8.5) into (upper) salinity and (lower) temperature components. The fraction of lightening due to salinity and temperature are plotted for (left) the annual average, (center) March, and (right) September, chosen as the late winter months when deep convection occurs in the high latitudes.

As surface freshening is indeed the dominant driver of surface buoyancy increases in the SPG under warming, we proceed to investigate the commonly described mechanism in which increasing subpolar stratification due to freshwater inhibits deep convection and ultimately weakens the AMOC. With the inter-model comparison framework of CMIP5, each model exhibits a different temperature and salinity response in the SPG, and these differences can be used to search for significant relationships between density changes and different aspects of the overturning circulation.

Fig. 5-2 shows the relationship between changes in surface S and T in the SPG and deep convection across the CMIP5 ensemble. The extent of deep convection is defined as the area where the March MLD exceeds 1000 m, the depth where convectively mixed waters may propagate into the southward flowing lower limb of the AMOC. Across models, freshening is relatively well correlated ($\rho = 0.65$) with reduced deep convection area, while warming is nearly uncorrelated ($\rho = -.04$). This is consistent with the density decomposition seen in Fig. 5-1, where freshening dominates the total wintertime density changes in the SPG. All models show a reduction in deep convection, with 7 of 28 ceasing deep convection entirely in the climatological average.

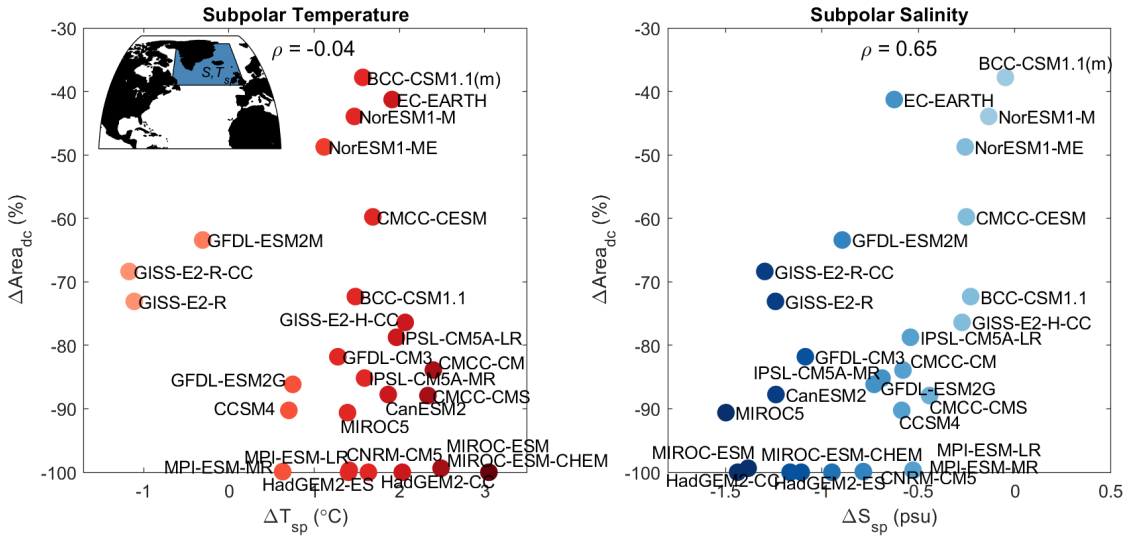

Figure 5-2: 100-year changes in (left) SST and (right) SSS averaged over the subpolar gyre (blue area, inset) are plotted against changes the area of deep convection $Area_{dc}$ defined as locations where $MLD > 1000\,\text{m}$ for 28 CMIP5 models from the RCP8.5 scenario.

Next, we search for evidence of teleconnections between subpolar surface density anomalies and the overturning strength further south. The overturning streamfunction at 40°N is chosen for comparison, as this is near the point of maximum overturning strength for most models, and represents a location disconnected from the SPG by the intergyre boundary. Fig. 5-3 shows the relationship across models between SPG surface S and T changes and Ψ at 40°N. Again, freshening is relatively well correlated ($\rho = 0.65$) with a weakening of Ψ_{40N}, while warming is very weakly correlated ($\rho = 0.10$).

However, we emphasize that these correlations are inadequate to assign causality, particularly due to the presence of advective feedbacks in AMOC. In the upper limb, the northward flow of the AMOC carries salt and heat into the SPG. Hence, it is expected that if the AMOC were to weaken for other reasons, the SPG would freshen and cool, such that the correlation in Fig. 5-3 may not be caused by salinity changes.

To understand the true cause of a changes to the subtropical AMOC, we make use of the fact that the AMOC strength on climate timescales can largely be described by the thermal wind relationship (Buckley et al., 2012), as the large-scale flow is approximately in geostrophic balance. To understand these changes, we analyze depth sections of S and T directly at 40°N to see how local density changes alter the streamfunction, and then interpret the ways in which these changes may have propagated along circulation pathways.

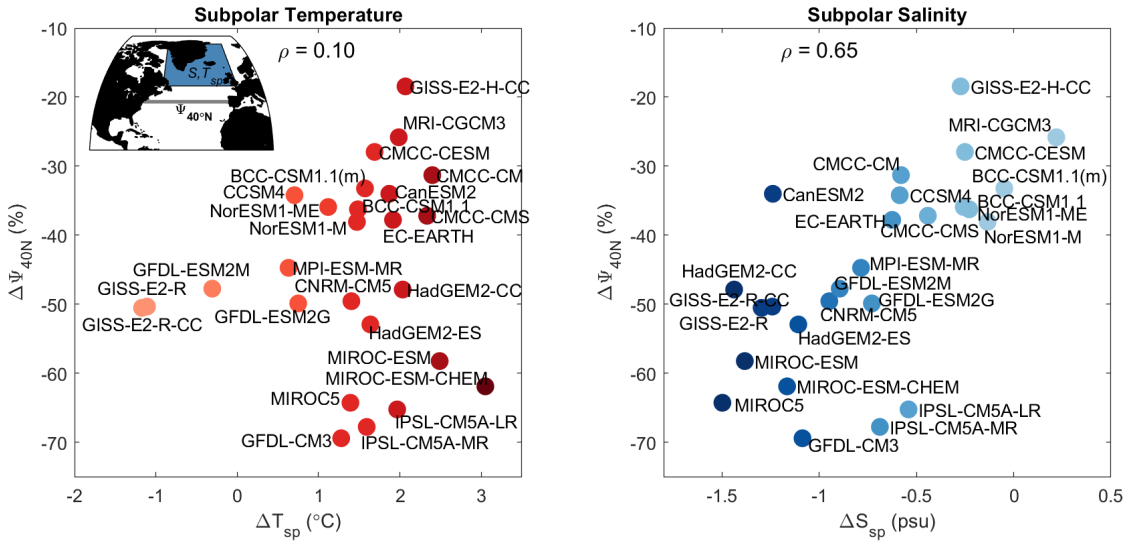

Figure 5-3: As in Fig. 5-2, 100-year changes in (left) surface temperature and (right) surface salinity averaged over the subpolar gyre (blue area, inset) are plotted against changes in the meridional overturning streamfunction at 40°N for 28 CMIP5 models from the RCP8.5 scenario.

5.4 Thermal Wind Diagnostics

Following Hirschi and Marotzke (2007), Buckley et al. (2012), and others we calculate the geostrophic component of the AMOC using density anomalies on the eastern (ρ_e) and western (ρ_w) margins of the Atlantic basin. The zonally averaged velocity $\overline{v}_g$ is calculated from thermal wind as:

$$\overline{v}_g(z) = \frac{g}{\rho_0 f} \int_{-H}^{z} \frac{1}{L(z)} (\rho_w - \rho_e)\, dz \tag{5.2}$$

where H is the ocean depth, g is the gravitational acceleration, ρ_0 is a reference density, and $L(z)$ is the basin width. There is also a wind-driven component of the AMOC, but here we focus only on the geostrophic contribution which is affected by density changes. An overturning streamfunction $\Psi(z)$ is then calculated, where mass conservation is enforced by subtracting the vertically averaged geostrophic velocity, known as the external mode:

$$\Psi(z) = \int_{x_w}^{x_e} \int_{-H}^{z} \left[\overline{v}_g - \frac{1}{H} \int_{-H}^{z} \overline{v}_g\, dz \right] dz\, dx \tag{5.3}$$

The streamfunction is calculated for individual models by first extracting ρ_e and ρ_w on their native grids, as each model has a different representation of bathymetry and coastlines,

and then interpolating this vertical profile of density gradients onto a common depth profile and averaging into a multi-model mean.

Fig. 5-4 shows the multi-model mean temperature and salinity changes for a latitude-depth section at 40°N. Buoyancy increases across the basin from about 2500 m to the surface, with little change below this depth. A bowl of relatively warm and salty water pools on the western side of the basin (also visible in in Fig. 5-6), a sign of surface anomalies accumulated in the mean gyre flow. However, these signals are largely compensated, with salinification cancelling out much of the warming. There is also a thin layer of large positive buoyancy anomalies along the eastern side of the basin, due to freshened subpolar water reaching the subtropical gyre via southward Ekman transport across the intergyre boundary.

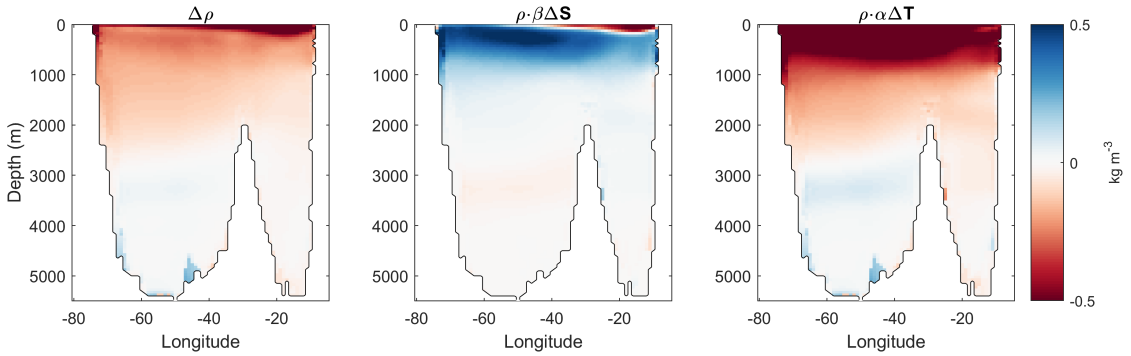

Figure 5-4: Cross section of 100-year multi-model mean RCP8.5 density changes at 40°N. Plotted are the (left) total density changes, (middle) the contribution from salinity, and (right) the contribution from temperature.

Fig. 5-5 shows changes in the AMOC calculated from thermal wind, and the density anomalies on the zonal margins which produce the changes. A time series of the geostrophic streamfunction is calculated over the RCP8.5 multi-model mean, taking into account only temperature and salinity changes separately, as well as the total change (Fig. 5-5A). This calculation reveals that temperature changes drive a weakening of the AMOC at 40°N, while salinity changes actually work to strengthen the overturning, with the total density changes producing a moderate net weakening. The lower panel of Fig. 5-5 shows the density anomalies extracted from the eastern and western margins which are used to calculate the streamfunction from thermal wind. It can be seen that in the mean state, isopycnals slope downwards from west to east ($\rho_w > \rho_e$) above 2000 m, which is the salient feature that drives the overturning cell. In the RCP8.5 changes, western waters gain more buoyancy than eastern waters between the depths of 2500 m and 500 m, and it is this flattening of

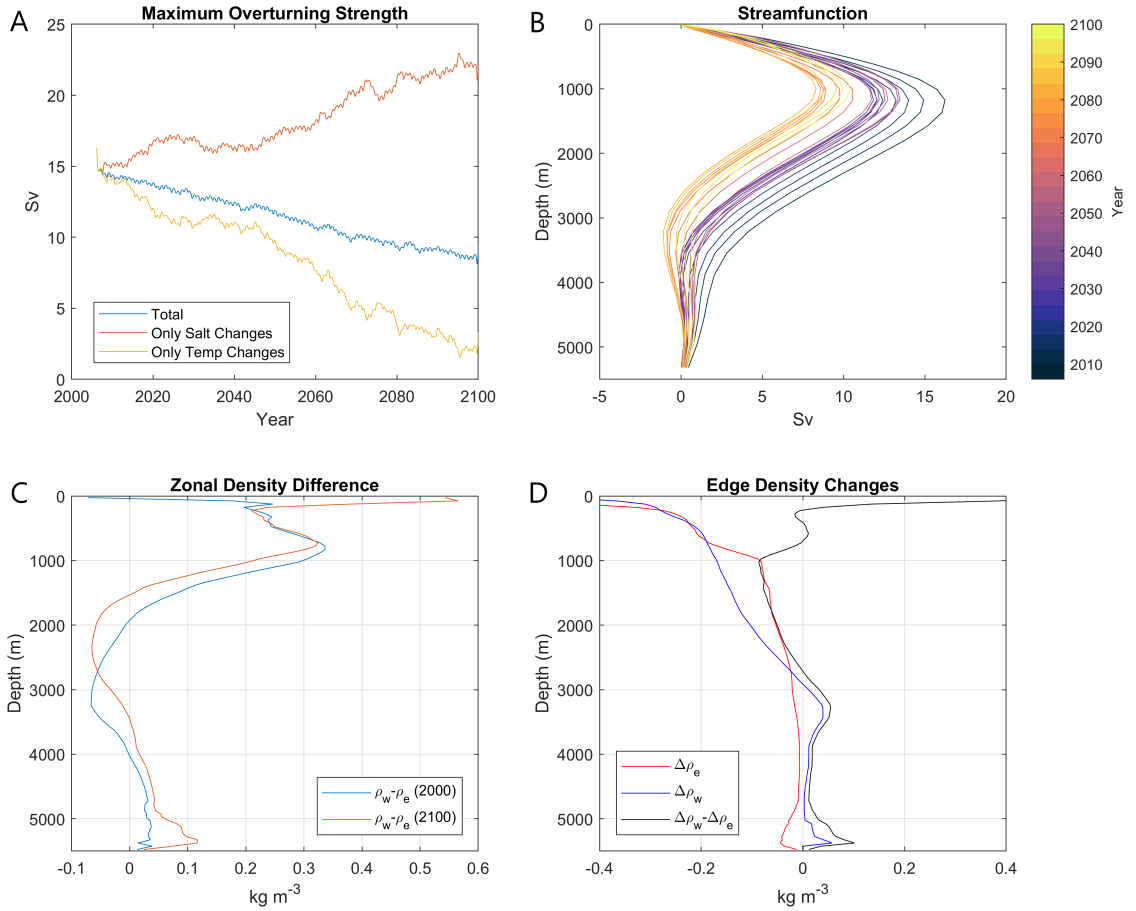

Figure 5-5: 100-year multi-model mean RCP8.5 changes at 40°N. (A) Maximum of the overturning streamfunction calculated from thermal wind through the RCP8.5 time period. (B) Depth structure of the overturning streamfunction changes. (C) Density difference across the Atlantic basin at the beginning and end of RCP8.5. (D) Density changes on the eastern and western margins over RCP8.5.

isopycnals that drives the reduction in the streamfunction. At the surface, buoyancy gain at the eastern margin exceeds that at the west, but this thin layer has only a weak effect on the depth-integrated streamfunction.

The largest change in isopycnal slopes occurs between 1000 m and 2000 m in the deep southward flowing branch of the AMOC. The positive buoyancy anomalies in the deep branch on the western margin are a result of warming. In the multi-model mean, salinities at this depth actually increase slightly. This result is contrary to traditional assumptions that fresh surface anomalies in the SPG will propagate along the deep western boundary current (DWBC) and freshen the western side of the basin, weakening the circulation.

It is not obvious how this salinity signal reaches the lower-limb in the subtropical gyre.

A more detailed assessment could be provided through tracer release or particle tracking experiments. One possibility is that warm and salty waters are being diffused downwards through the thermocline at an excessive rate. However, we note here that even in the SPG, there is a weak salinification of waters below a thin 100 m surface fresh layer (Fig. 5-7, and Heuzé et al., 2014). This suggests that the subsurface SPG is being influenced by advected subtropical waters, and that a thin surface fresh layer in the SPG is not indicative of the total vertical salinity change.

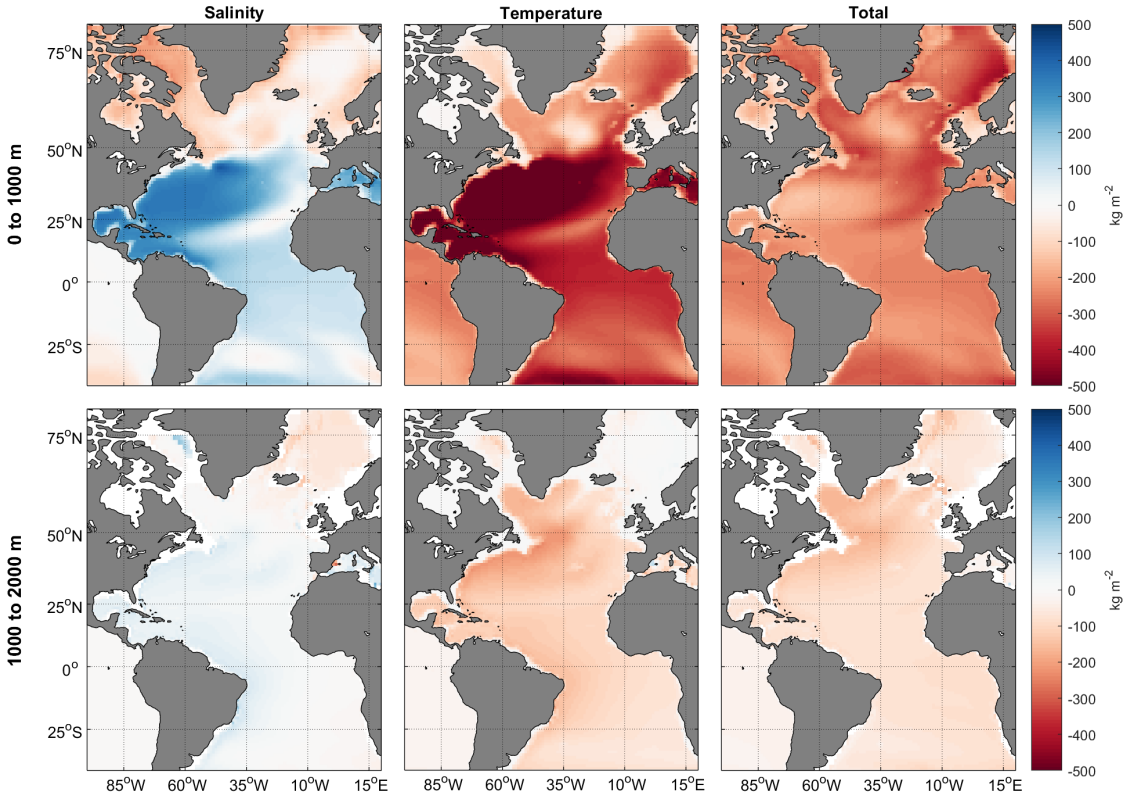

Figure 5-6: 100-year multi-model mean density changes in RCP8.5 vertically integrated from (upper) 0-1000 m and (lower) 1000-2000 m depth in the Atlantic. The total density change is shown on the right, and is also decomposed into (left) salinity and (middle) temperature components.

While there is no clear evidence of freshened subpolar surface waters propagating in the DWBC, this does not necessarily indicate a lack of connectivity between the SPG and the DWBC. Rather, the weak salinification is consistent with an overturning streamfunction that carries saltier subtropical waters northward across a broad upper layer between 0 m and 1000 m (see streamfunction in Fig. 5-5). Therefore, it may be more accurate to consider the full vertical profile of S and T changes over the SPG as the source waters for buoyancy

anomalies in the DWBC rather than surface waters alone, given that the lower limb also draws from waters at depth. This perspective is consistent with the work of Marshall and Schott (1999) and others, who found that convective plumes produce a negligible downward mass flux, so that source waters in the downwelling branch of the AMOC are not fed directly from the surface by convective events.

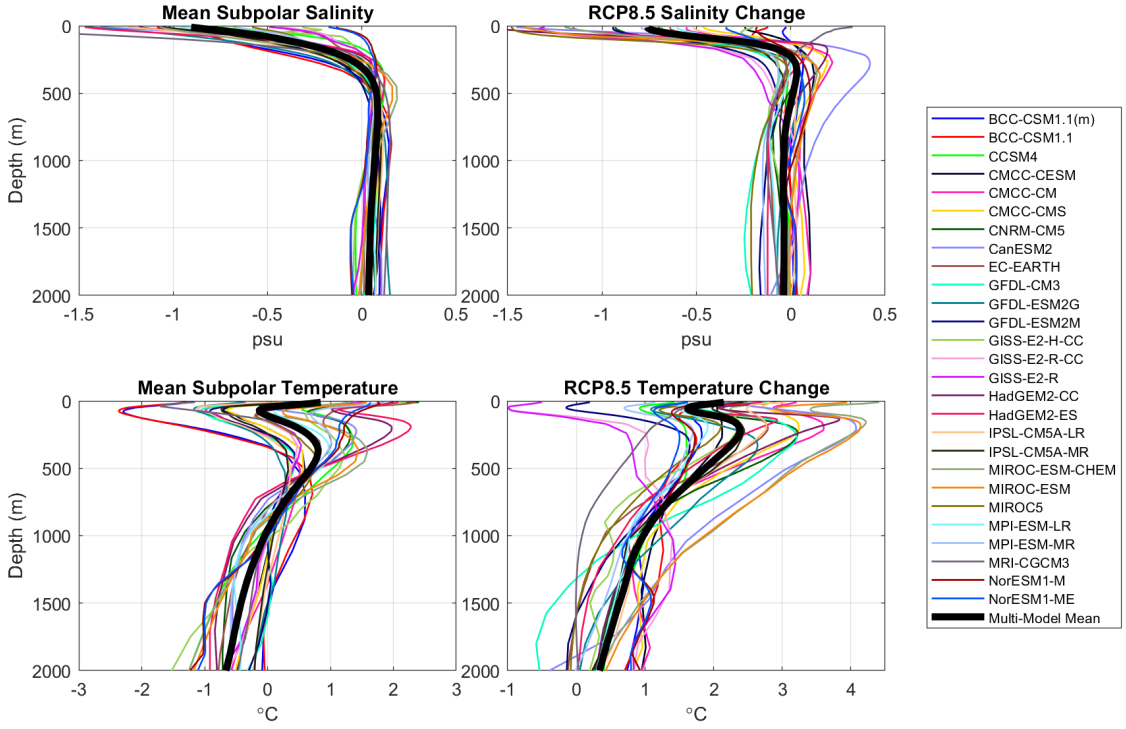

Figure 5-7: Vertical profiles of salinity (upper) and temperature (lower) averaged over the subpolar box shown in Fig. 5-2 and 5-3 for individual CIMP5 models. On the left is the mean vertical profile for the year 2000 with the vertical average subtracted out, and on the right are the 100-year RCP8.5 changes. Warming occurs throughout the upper 2000 m, with substantial freshening in the upper 100 m but a slight increase in salinity below this layer.

This result provides a very different perspective on the role of salt in AMOC changes under a warming scenario. The net effect of the salinity change is to stabilize the AMOC against warm anomalies which accumulate on the western side of the gyre. The dominant influence of salt in the AMOC response is from salinified subtropical waters produced by increased evaporation. These high salinities strongly counteract the tendency of warming in the upper limb, which would otherwise further weaken the AMOC. Despite a strong fresh layer at the SPG surface, we do not find evidence of this positive buoyancy anomaly further south along the DWBC. While there is significant freshwater input to the SPG, vertically integrated salinity tendencies in the SPG are weak, potentially balanced out by

the influence of anomalously salty subtropical water which has propagated northward at intermediate depths.

One potential caveat to this analysis is the limited representation of Mediterranean overflow water in CMIP5 models. Mediterranean waters have been implicated as a potentially important source of salt to the Atlantic SPG (Lozier and Stewart, 2008), and observations indicate that the Mediterranean is getting significantly saltier and warmer (Potter and Lozier, 2004) in agreement with the CMIP5 models. However, Fig. 5-5 and Fig. 5-6 do not show evidence of this anomalously warm and salty water mass flowing northward at depth. Narrow overflow dynamics are difficult to represent in coarse models, and a better representation of Mediterranean overflow in coupled models could potentially provide another means of carrying subtropical salinity anomalies into the SPG. Furthermore, Mediterranean overflow water is typically carried at 1000-1200 m depth, which is significantly deeper than any other water mass with subtropical surface origins, which could more readily influence the deep limb of the AMOC.

5.5 Conclusions

In this study, we address a persistent theory that subpolar freshening is responsible for a weakening AMOC under climate warming scenarios. The specific balance of energy sources that drive the AMOC remains controversial, but here we use the fact that the overturning circulation is nearly geostrophic to identify how density changes throughout the water column alter the streamfunction.

In CMIP5, weakening of the AMOC is fundamentally driven by temperature anomalies rather than freshwater anomalies. The role of freshwater forcing is more complex than previously thought. In the RCP8.5 scenario, the influence of subpolar surface freshening is secondary to the influence of subtropical salinification. In the upper layer of the subtropics, this anomalously salty water mass pools on the western side of the gyre, balancing the effect of temperature increases. We also infer that this salty subtropical water has propagated into the deep limb of the AMOC. Subtropical water first flows northward across the intergyre boundary at intermediate depths in the upper branch of the AMOC, and is eventually subducted into the DWBC after being mixed together with freshened surface waters. The resulting water mass found in the DWBC at 40°N has a moderate temperature increase and

very little salinity change. The composition of source waters for the DWBC could be further studied with particle tracking experiments as in Chapter 4, to identify the relative balance of subtropical and subpolar surface influences in the deep limb of the AMOC.

In a warming scenario with water cycle amplification, contrary to previous studies, freshwater flux changes actually act to stabilize the AMOC. However, there is still much to learn about these dynamics and the role of surface freshening in setting the response on longer timescales. For example, it is possible that with a fresh and buoyant subpolar surface layer, the inhibition of deep convection works to gradually warm the DWBC as cold wintertime surface waters do not enter the deep circulation. A better understanding of these relationships would require targeted modeling experiments in order to more effectively isolate the effects of freshwater and heat forcing, and to identify precisely how these anomalies propagate through the system. Furthermore, CMIP5 models do not include the effects of Greenland melt, which may alter the freshwater balance in the SPG.

These results again highlight the importance of oceanic connectivity in the climate response. This is particularly evident for salinity dynamics, as climate forcing tends to produce an alternating pattern of fresh and salty anomalies across the global oceans. The degree to which these opposite-signed anomalies are communicated between the gyres can have profound implications for the ocean circulation response.

5.6 Chapter Acknowledgements

We acknowledge the World Climate Research Programme's Working Group on Coupled Modelling, which is responsible for CMIP, and we thank the climate modeling groups (listed in Table 5.1 of this paper) for producing and making available their model output. This work was supported by NASA Headquarters under the NASA Earth and Space Science Fellowship Program award 80NSSC17K0372.

5.7 Supplementary Material

5.8 Other Influences of Salt on Circulation

While Chapter 5 focuses on the influence of salinity changes on the AMOC response, salt is also important to other aspects of the circulation and stratification response. Fig. 5-1 shows that in addition to the Atlantic SPG, freshening dominates surface buoyancy increases along the coastal margins of Antarctica, and also contributes significantly across the tropical oceans. The only region where salinity increases exceed warming in terms of density is the Sargasso Sea, where surface waters become heavier over the RCP8.5 experiment (white area in Fig. 5-1). Here we briefly address some of these other regions.

5.8.1 Global Mixed-Layer Depth

Transient buoyancy increases at the surface tend to increase stratification of the upper ocean, as deeper layers adjust more slowly to climate forcing (Capotondi et al., 2012). This in turn affects the surface mixed-layer depth (MLD). Fig. 5-8 shows the annual average fractional change in MLD for the 100-year RCP8.5 period. MLD is reduced nearly everywhere, except for small areas of the subtropical gyre centers in the North Atlantic, South Atlantic, and South Pacific, and in the Barents Sea, all locations where salinity increases in CMIP5. The mixed-layer shoals significantly across the subpolar North Atlantic and in the far Southern Ocean, where freshening occurs. MLD is also affected by changes in wind, thermocline ventilation, and other factors, but the relative contributions of T and S to MLD changes can be roughly inferred from the decomposition in Fig. 5-1.

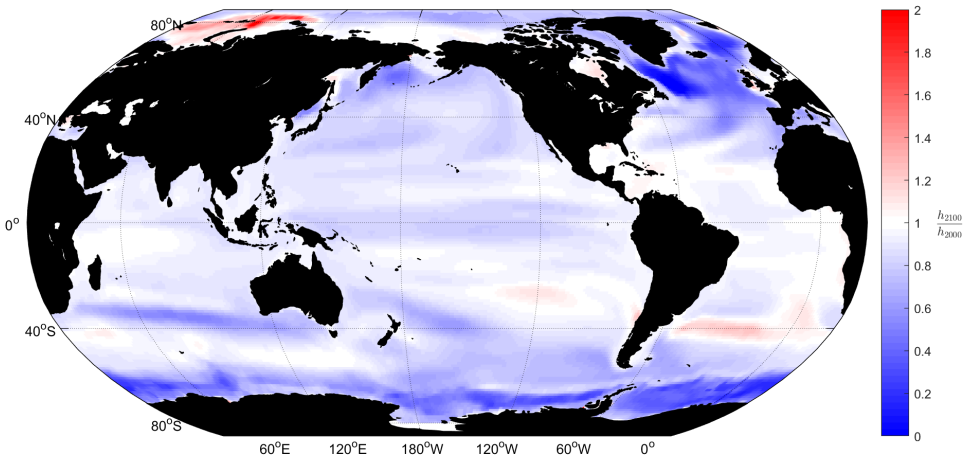

Figure 5-8: 100-year change in MLD from CMIP5 RCP8.5, expressed as a fractional change of $\frac{h_{2100}}{h_{2000}}$. Warming increases vertical stratification and reduces the MLD nearly everywhere, which is enhanced in regions with freshening, namely the high-latitudes and tropical Pacific.

5.8.2 Tropical Barrier Layers

In the tropics, freshwater input from the ITCZ acts to generate haline stratification which is shallower than the isothermal layer. This layer below the surface, which is mixed in temperature but salt-stratified, is known as the barrier layer. Barrier layers change the ocean's response to atmospheric fluxes, because entrainment does not cool the surface mixed-layer as it does when the water below the surface mixed-layer is temperature-stratified. There is some evidence that the barrier layer is relevant to tropical ocean-atmosphere coupling phenomena such as the El Nino-Southern Oscillation (Maes et al., 2018; Zhu et al., 2014) and the Madden-Julian Oscillation (Drushka et al., 2011).

In CMIP5, salinity contributes 20-50% of surface buoyancy increase in the tropical Pacific (Fig. 5-1), with the rest due to warming. Subsequently, the MLD shoals by about 20% in the 100-year RCP8.5 changes (Fig. 5-8). The shoaling is weaker in the equatorial Indian and Atlantic, where freshening is weak or nonexistent. We also compute 100-year trends in the barrier layer thickness (BLT). Following de Boyer Montégut et al. (2007), the BLT is defined as the difference between the depth where temperature has decreased by 0.2 °C and the depth where density has increased by an amount equivalent to an 0.2 °C change at constant salinity. Fig. 5-9 shows the multi-model mean BLT climatology and 100-year trends from RCP8.5. With the large increase in ITCZ rainfall, BLT grows across much of the deep tropics, particularly in the western equatorial Pacific.

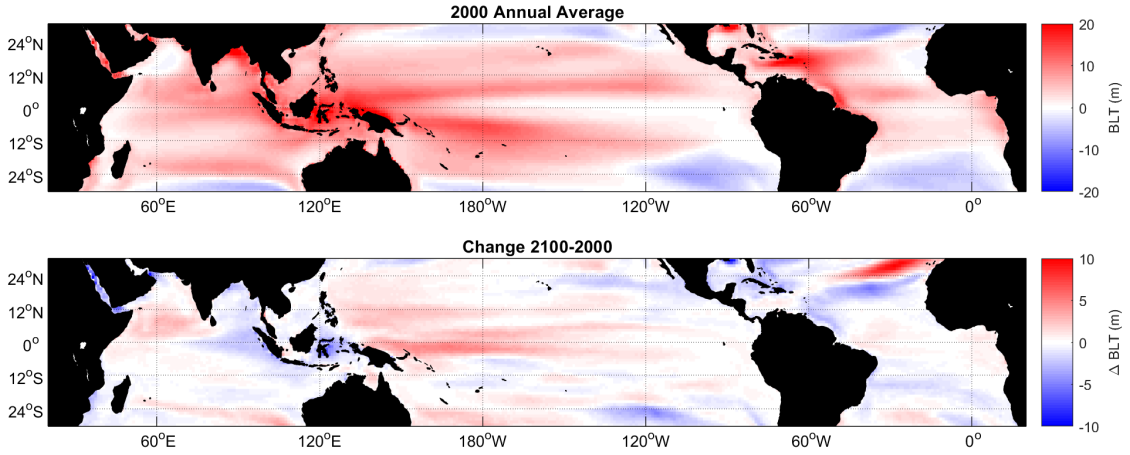

Figure 5-9: (upper) Annual average multi-model mean BLT at the beginning of the RCP8.5 experiment and (lower) 100-year change in BLT. Additional freshwater input in the Pacific ITCZ enhances salinity stratification and produces a tendency towards shallower mixed layers with thicker barrier layers.

5.8.3 Deep Water Formation in the Southern Ocean

Besides the North Atlantic, the other global source of deep water formation is in the Southern Ocean, along the coastal margins of Antarctica. Salinity also plays an important role in setting the high density of precursors to Antarctic Bottom Water (AABW), where brine rejection from sea ice formation works to increase surface salinities (Ohshima et al., 2013). In both present-day observations and model projections, the Southern Ocean appears as a region of delayed response to climate forcing. To first order, this is a result of the background circulation, where Southern Ocean surface waters are upwelled from great depths (Armour et al., 2016). The timescale of this upwelling is $O(100-1000\text{yrs})$, such that upwelled waters have not felt the influences of climate warming at the ocean surface on centennial timescales.

This is compounded by the fact that the Southern Ocean has a very deep surface mixed layer during the winter months, driven by strong wind forcing and weak vertical stratification. Therefore, any anomalous surface fluxes are diluted throughout a thick layer. We also note that the precursors to AABW have a much different surface exposure history than the precursors to NADW. NADW source waters typically experience a long surface pathway, first upwelling in the Southern Ocean or crossing from the Indo-Pacific via the Agulhas Leakage, feeling influences at the surface from the entire Atlantic basin before eventually sinking in the subpolar gyre. AABW sources, on the other hand, cover a shorter surface route between upwelling in the Southern Ocean and sinking near Antarctica.

Nevertheless, models (Levang and Schmitt, 2015) and observations (Durack et al., 2012) do show a modest ongoing freshening trend across the Southern Ocean due to increased net precipitation. The Southern Ocean also shows a substantial decrease in winter MLD in CMIP5 (Fig. 5-8). The surface density changes are primarily due to warming across most of the Southern Ocean, but salinity dominated near the Antarctic coast (Fig. 5-1). Glacial melt from the Antarctic ice sheets may also add to this freshening tendency, which is not included in CMIP5.

Some work suggests that freshening of the Southern Ocean may have a significant impact on deep overturning (de Lavergne et al., 2014; Purich et al., 2018). In CMIP5, the Southern Meridional Overturning Circulation (SMOC) shows slight weakening but with little confidence between models (Heuzé et al., 2014). There is also no clear trend in bottom water salinities.

With freshening around the coast of Antarctica, there is also the potential for a positive feedback loop. In the mechanism proposed by Silvano et al. (2018), increased surface stratification prevents mixing between relatively cooler surface waters and warmer waters at depth. This maintains a warmer temperature in the deeper layers which generate basal melt, adding further freshwater and stratification to the system. This mechanism cannot be analyzed in CMIP5 given the lack of active ice sheets, but it provides further incentive to understand the Southern Ocean salinity response.

Institute	Model	CMIP5 variables: so, to, vo
BCC	BCC-CSM1.1	x
BCC	BCC-CSM1.1(m)	x
CMCC	CMCC-CESM	x
CMCC	CMCC-CM	x
CMCC	CMCC-CMS	x
CNRM-CERFACS	CNRM-CM5	x
ICHEC	EC-EARTH	x
INM	INM-CM4	x
IPSL	IPSL-CM5A-LR	x
IPSL	IPSL-CM5A-MR	x
MIROC	MIROC-ESM	x
MIROC	MIROC-ESM-CHEM	x
MIROC	MIROC5	x
MOHC	HadGEM2-CC	x
MOHC	HadGEM2-ES	x
MPI-M	MPI-ESM-LR	x
MPI-M	MPI-ESM-MR	x
MRI	MRI-CGCM3	x
NASA-GISS	GISS-E2-H-CC	x
NASA-GISS	GISS-E2-R	x
NASA-GISS	GISS-E2-R-CC	x
NCAR	CCSM4	x
NCC	NorESM1-M	x
NCC	NorESM1-ME	x
NOAA-GFDL	GFDL-CM3	x
NOAA-GFDL	GFDL-ESM2G	x
NOAA-GFDL	GFDL-ESM2M	x

Table 5.1: List of CMIP5 models used to produce all figures in Chapter 5 for the variables ocean salinity (*so*), ocean temperature (*to*), and northward ocean velocity (*vo*). Further details for each model may be found in Flato et al. (2014).

THIS PAGE INTENTIONALLY LEFT BLANK

Chapter 6

Conclusion

6.1 Summary of Findings

Salinity is an important physical property in the ocean, both as a driver of circulation and as an indicator for the atmospheric water cycle. This thesis investigates how the global salinity field may change under planetary warming, and how that could affect ocean circulation. As this is fundamentally a question about the future ocean rather than its current state, we rely primarily on model simulations, but try to ground-truth simulations with an observational basis wherever possible.

Chapter 2 analyzes climate projections for the water cycle and salinity in the fully coupled ocean-atmosphere models of CMIP5. Using a model intercomparison framework gives information about where the response is robust and consistent across models. While the models can of course have systematic biases, model intercomparison is a powerful tool when combined with theoretical arguments, guiding future work toward the most uncertain aspects of the system.

Results from CMIP5 indicate that the atmospheric water cycle undergoes coherent amplification under warming, generally following the "rich get richer" pattern. The equator and high latitudes see increased net P, while the subtropics see increased net E. Additionally, the transport of water vapor from Atlantic to Pacific is amplified, causing a particularly large increase in P near the equatorial Pacific. Salinity changes generally mirror these trends, with surface salinification in the subtropics and freshening in the tropics and high latitudes, as well as salinification of the Atlantic relative to the Indo-Pacific.

Some aspects of the multi-model mean response show a clear influence from ocean advec-

tion. In the subtropical Pacific where E increases, the models show either weak salinification or freshening, which indicates mixing with additional freshwater input near the equator. Similarly in the equatorial Atlantic, where P increases, the models show salinification due to mixing with surrounding subtropical waters. The degree to which these signals mix varies between models. The subpolar gyres appear to be relatively isolated from basin-wide forcing. While most models show freshening in the subpolar Atlantic, a subset (20%) show propagation of saltier subtropical waters into the SPG. This region is of particular interest due to its role in setting properties in the deep branch of the AMOC.

Given these uncertainties which stem from differences in ocean advection of salinity anomalies, it is important to understand the major transport pathways for salt in the upper ocean. In Chapter 3, we step back from coupled simulations and analyze a steady-state SML salinity budget for the present day climate, based on ECCO and an observational dataset. A decomposition identifies regions where the surface forcing is primarily balanced by either lateral transports within the SML or vertical transports with the thermocline below. This provides context for oceanic pathways that may transport salinity anomalies in the CMIP5 results.

Between the equator and the subtropics, the ocean is efficiently connected at the surface by the shallow subtropical cell, which carries freshwater poleward from the ITCZ and returns salty water equatorward at depth. This connection allows climate salinity anomalies to become relatively well mixed on the timescale of the forcing. On the other hand, the subpolar gyres are dominated by vertical exchange with deeper waters, and little surface connection exists between the subpolar and subtropical gyres. However, an area of particularly strong lateral mixing in the Gulf Stream and North Atlantic Current suggest that eddy processes could play a role in carrying salty subtropical anomalies into the subpolar gyre, as seen in some CMIP5 models.

The Eulerian framework of the SML budget gives only basic information about regional connectivity, so we use a complimentary Lagrangian particle tracking technique in Chapter 4 to better understand how salinity anomalies are transported. A series of timescale experiments using trajectories generated in different ocean state estimates confirms that the exchange of surface waters between the tropics and subtropics takes only $O(1yr)$, while the exchange between the subtropical and subpolar gyres is much slower. In a coarse model with parameterized eddies this timescale may be $O(100yrs)$, while an eddy permitting model

shows much faster exchange of $O(20yrs)$.

To apply the Lagrangian methods directly to the salinity response problem, we develop a technique to advect freshwater forcing anomalies along trajectories as a passive tracer. When the CMIP5 multi-model mean $\Delta(E-P)$ is applied as the tracer, the method shows remarkable success in replicating the CMIP5 salinity response. Experiments with both an eddy-permitting model and a coarse-resolution model confirm that eddies increase the transport of salty subtropical anomalies into the subpolar gyre.

With a better understanding of the salinity changes that occur and mechanisms for inter-model spread, Chapter 5 aims to assess how these changes affect ocean circulation with a focus on the AMOC. While freshening dominates the subpolar surface density budget, this water mass does not significantly influence the strength of the AMOC in the subtropics, and AMOC weakening is fundamentally driven by temperature changes. The major influence of salt is due to the salinification of subtropical waters, which balance out buoyancy increases due to temperature anomalies. This salty subtropical water also appears to propagate along the deep limb of the circulation, mixing together with and balancing out the density changes of subpolar surface freshening.

6.2 Implications

6.2.1 Role of Salinity in the AMOC Response

While the classical paradigm holds that changes in wintertime subpolar surface waters propagate through the deep branch of the AMOC and alter its strength, we find that changes in the DWBC are more similar to the depth-averaged subpolar properties in CMIP5. The AMOC streamfunction carries a northward transport across a broad upper layer of 1000 m depth, and this picture indicates that the DWBC is not only supplied by subpolar surface waters, but is instead fed more broadly from the upper layer. In a warming scenario, this layer is likely to to feel the influence of subtropical water property changes, as the AMOC carries subtropical waters across the intergyre boundary along primarily subsurface pathways. Therefore, even with a strong fresh cap at the subpolar surface, salty anomalies which propagate from the subtropical gyre at depth may cancel out surface freshening in the total changes to deep-water properties.

6.2.2 Importance of Oceanic Connectivity to the Climate Response

Water cycle intensification induces an alternating pattern of positive and negative freshwater flux anomalies across the global oceans. This forcing pattern provides an illustrative example of how oceanic connectivity can substantially alter the ocean's response to climate trends. Because the anomalies are opposite-signed, the strength of oceanic freshwater transport between hydrologic regimes can fundamentally alter the salinity response. This is best seen in the Atlantic subpolar gyre, where all CMIP5 models show increased positive freshwater fluxes, but surface salinity changes range from strongly negative to moderately positive between the models. We demonstrate that eddy fluxes at the intergyre boundary are fundamental to this exchange. The intergyre boundary is a highly energetic region where the intense western boundary current breaks down into a meandering and unstable jet, and this enhanced eddy transport is not captured in coarse models that use constant Redi and GM coefficients. Therefore, coarse models with variable mixing coefficients that account for the enhanced eddy energy at the intergyre boundaries, as well as eddy-permitting models, likely produce a more accurate climate response.

6.2.3 Effectiveness of the Ocean Rain Gauge

The role of ocean transports in modifying the salinity response relative to changes in freshwater fluxes limits the use of ocean salinity as a rain-gauge to monitor changes in the atmospheric water cycle under climate change. Attempting to quantitatively infer a rate of water cycle intensification based on salinity changes will be subject to large uncertainty without precise knowledge of the advective transports explored in this thesis. However, arguments presented here suggest that particular regions are better suited for early detection of significant salinity trends induced by water cycle intensification. Generally, these are regions where basin-wide trends reinforce local trends, namely the subtropical Atlantic and the tropical Pacific. Regions subject to large uncertainty due to ocean dynamics are the subpolar North Atlantic, which is influenced to an unknown degree by the import of anomalously salty subtropical water, and the Indian Ocean, where the transport of Pacific freshwater anomalies through the Indonesian Throughflow is poorly constrained. The Southern Ocean is likely to display a weak freshening trend, due to deep mixed-layers and constant replenishment with upwelled deep waters.

6.3 Future Work

To build on the insights of this thesis, we suggest a number of directions for continued research:

Further constraining the atmospheric response. The atmospheric models of CMIP5 show a relatively coherent water cycle response to warming, but significant biases still exist in these models. In particular, GCMs have issues with tropical precipitation and water vapor transport over sharp mountain ranges when compared to observations. To increase confidence in model projections, further work is needed to understand the ways in which they fail to match the observed mean climate.

Individual analysis of coupled models. Particle tracking experiments presented here use ocean state estimates for the velocity fields as a simplification of the problem. Further work could be done to test anomaly propagation with trajectories in coupled models to also allow for changes in circulation pathways. These experiments were not performed here for the CMIP5 runs because CMIP5 models do not generally include outputs of their GM fluxes.

Eddy-resolving coupled MIPs. CMIP6 will be the next iteration of collaborative climate modeling experiments, and will include a high-resolution ensemble (HighResMIP; Haarsma et al., 2016). These models will offer a useful test of results from Chapter 4, which indicate that resolved eddies provide greater intergyre salt transport than typical coarse model parameterizations, and may alter the composition of DWBC waters and the AMOC response.

Further exploration of the AMOC response. As demonstrated here, the propagation of forcing anomalies through the AMOC system is complex and difficult to fully disentangle in coupled simulations with changes to both freshwater and heat fluxes. Hence, simplified model runs in which only one of these forcing terms is allowed to change may help to elucidate the evolution of the system. A particle tracking approach, such as the one used in Chapter 4, could better quantify the mixture of source waters for the DWBC in the Atlantic, and how this mixture produces the deep salinity response seen in CMIP5.

Other salt-driven circulations. We focus on the AMOC as an important circulation where salt can influence the climate response, but as described briefly in Chapter 5, interesting dynamics occur in other regions as well. In the ocean's other deep overturning cell fed by dense waters off of Antarctica, freshening also dominates the buoyancy budget in

CMIP5. There is limited understanding of how these changes affect the larger overturning cell, and how they may feed back on ice sheet dynamics.

Continuous observing systems. As the records from Argo and microwave satellite salinity retrievals grow in length, these datasets should be carefully examined for signatures of water cycle intensification. Observable trends will lend confidence to projections that are currently based primarily on models and theory.

6.4 Final Thoughts

Changes in the water cycle will have some of the largest societal influences under climate change (Field et al., 2014). The ocean serves as a useful indicator for these changes, as salinity integrates freshwater forcing over long timescales and provides a memory of atmospheric processes. This thesis has analyzed some of the most dynamic aspects of the salinity response to climate change as represented in coupled models. These changes can significantly alter ocean circulation, especially in the AMOC, with implications for global and regional climates. Despite advances presented here, high-confidence projections of the AMOC response to warming remain out of reach. Salinity changes are key to the response, and many aspects of this complex system are still not understood.

Bibliography

Aagaard, K. and Carmack, E. C. (1989). The role of sea ice and other fresh water in the Arctic circulation. *Journal of Geophysical Research: Oceans*, 94(C10):14485–14498.

Abernathey, R. P. and Marshall, J. (2013). Global surface eddy diffusivities derived from satellite altimetry. *Journal of Geophysical Research: Oceans*, 118(2):901–916.

Adcroft, A. and Campin, J.-M. (2004). Rescaled height coordinates for accurate representation of free-surface flows in ocean circulation models. *Ocean Modelling*, 7(3):269–284.

Adler, R. F., Huffman, G. J., Chang, A., Ferraro, R., Xie, P.-P., Janowiak, J., Rudolf, B., Schneider, U., Curtis, S., Bolvin, D., Gruber, A., Susskind, J., Arkin, P., and Nelkin, E. (2003). The Version-2 Global Precipitation Climatology Project (GPCP) Monthly Precipitation Analysis (1979–Present). *Journal of Hydrometeorology*, 4(6):1147–1167.

Allan, R. P. (2012). The Role of Water Vapour in Earth's Energy Flows. *Surveys in Geophysics*, 33(3):557–564.

Allan, R. P., Liu, C., Zahn, M., Lavers, D. A., Koukouvagias, E., and Bodas-Salcedo, A. (2014). Physically Consistent Responses of the Global Atmospheric Hydrological Cycle in Models and Observations. *Surveys in Geophysics*, 35(3):533–552.

Allen, M. R. and Ingram, W. J. (2002). Constraints on future changes in climate and the hydrologic cycle. *Nature*, 419:224–232.

Armour, K. C., Marshall, J., Scott, J. R., Donohoe, A., and Newsom, E. R. (2016). Southern Ocean warming delayed by circumpolar upwelling and equatorward transport. *Nature Geoscience*, 9(7):549–554.

AVISO (2018). Aviso + user handbooks. Technical report, CNES.

Baumgartner, A. and Reichel, E. (1975). *The world water balance: mean annual global, continental and maritime precipitation, evaporation and run-off*. Elsevier Scientific Pub. Co., Amsterdam; New York. OCLC: 647091051.

Beron-Vera, F. J., Ochoa, J., and Ripa, P. (1999). A note on boundary conditions for salt and freshwater balances. *Ocean Modelling*, 1(2–4):111–118.

Bower, A. S. (1991). A Simple Kinematic Mechanism for Mixing Fluid Parcels across a Meandering Jet. *Journal of Physical Oceanography*, 21(1):173–180.

Boyer, T. P., Levitus, S., Antonov, J. I., Locarnini, R. A., and Garcia, H. E. (2005). Linear trends in salinity for the World Ocean, 1955–1998. *Geophysical Research Letters*, 32(1).

Brambilla, E. and Talley, L. D. (2006). Surface drifter exchange between the North Atlantic subtropical and subpolar gyres. *Journal of Geophysical Research: Oceans*, 111(C7):C07026.

Bretherton, F. P., Davis, R. E., and Fandry, C. B. (1976). A technique for objective analysis and design of oceanographic experiments applied to MODE-73. *Deep Sea Research and Oceanographic Abstracts*, 23(7):559–582.

Broecker, W. (1991). The Great Ocean Conveyor. *Oceanography*, 4(2):79–89.

Broecker, W. S. (1994). Massive iceberg discharges as triggers for global climate change. *Nature*, 372(6505):421–424.

Broecker, W. S., Peng, T. H., Jouzel, J., and Russell, G. (1990). The magnitude of global fresh-water transports of importance to ocean circulation. *Climate Dynamics*, 4(2):73–79.

Brown, J. R., Moise, A. F., and Colman, R. A. (2013). The South Pacific Convergence Zone in CMIP5 simulations of historical and future climate. *Climate Dynamics*, 41(7):2179–2197.

Bryan, F. and Bachman, S. (2014). Isohaline Salinity Budget of the North Atlantic Salinity Maximum. *Journal of Physical Oceanography*, 45(3):724–736.

Buckley, M. W., Ferreira, D., Campin, J.-M., Marshall, J., and Tulloch, R. (2012). On the Relationship between Decadal Buoyancy Anomalies and Variability of the Atlantic Meridional Overturning Circulation. *Journal of Climate*, 25(23):8009–8030.

Buckley, M. W. and Marshall, J. (2016). Observations, inferences, and mechanisms of the Atlantic Meridional Overturning Circulation: A review. *Reviews of Geophysics*, 54(1):5–63.

Burkholder, K. C. and Lozier, M. S. (2011). Subtropical to subpolar pathways in the North Atlantic: Deductions from Lagrangian trajectories. *Journal of Geophysical Research: Oceans*, 116(C7):C07017.

Busecke, J., Abernathey, R. P., and Gordon, A. L. (2017). Lateral Eddy Mixing in the Subtropical Salinity Maxima of the Global Ocean. *Journal of Physical Oceanography*, 47(4):737–754.

Busecke, J., Gordon, A. L., Li, Z., Bingham, F. M., and Font, J. (2014). Subtropical surface layer salinity budget and the role of mesoscale turbulence. *Journal of Geophysical Research: Oceans*, 119(7):4124–4140.

Cai, W., Borlace, S., Lengaigne, M., van Rensch, P., Collins, M., Vecchi, G., Timmermann, A., Santoso, A., McPhaden, M. J., Wu, L., England, M. H., Wang, G., Guilyardi, E., and Jin, F.-F. (2014). Increasing frequency of extreme El Niño events due to greenhouse warming. *Nature Climate Change*, 4(2):111–116.

Capotondi, A., Alexander, M. A., Bond, N. A., Curchitser, E. N., and Scott, J. D. (2012). Enhanced upper ocean stratification with climate change in the CMIP3 models. *Journal of Geophysical Research: Oceans*, 117(C4).

Carton, J. A., Chepurin, G. A., and Chen, L. (2018). SODA3: A New Ocean Climate Reanalysis. *Journal of Climate*, 31(17):6967–6983.

Chou, C. and Neelin, J. D. (2004). Mechanisms of Global Warming Impacts on Regional Tropical Precipitation. *Journal of Climate*, 17(13):2688–2701.

Chou, C., Neelin, J. D., Chen, C.-A., and Tu, J.-Y. (2009). Evaluating the "Rich-Get-Richer" Mechanism in Tropical Precipitation Change under Global Warming. *Journal of Climate*, 22(8):1982–2005.

Coachman, L. K. and Aagaard, K. (1988). Transports through Bering Strait: Annual and interannual variability. *Journal of Geophysical Research: Oceans*, 93(C12):15535–15539.

Cohen, J. L., Salstein, D. A., and Rosen, R. D. (2000). Interannual Variability in the Meridional Transport of Water Vapor. *Journal of Hydrometeorology*, 1(6):547–553.

Collins, M., Booth, B. B. B., Bhaskaran, B., Harris, G. R., Murphy, J. M., Sexton, D. M. H., and Webb, M. J. (2011). Climate model errors, feedbacks and forcings: a comparison of perturbed physics and multi-model ensembles. *Climate Dynamics*, 36(9):1737–1766.

Cronin, M. F. and McPhaden, M. J. (1998). Upper ocean salinity balance in the western equatorial Pacific. *Journal of Geophysical Research: Oceans*, 103(C12):27567–27587.

Dai, A. and Trenberth, K. E. (2002). Estimates of Freshwater Discharge from Continents: Latitudinal and Seasonal Variations. *Journal of Hydrometeorology*, 3(6):660–687.

Dansgaard, W., Johnsen, S. J., Clausen, H. B., Dahl-Jensen, D., Gundestrup, N. S., Hammer, C. U., Hvidberg, C. S., Steffensen, J. P., Sveinbjörnsdottir, A. E., Jouzel, J., and Bond, G. (1993). Evidence for general instability of past climate from a 250-kyr ice-core record. *Nature*, 364(6434):218–220.

de Boyer Montégut, C., Madec, G., Fischer, A. S., Lazar, A., and Iudicone, D. (2004). Mixed layer depth over the global ocean: An examination of profile data and a profile-based climatology. *Journal of Geophysical Research: Oceans*, 109(C12):C12003.

de Boyer Montégut, C., Mignot, J., Lazar, A., and Cravatte, S. (2007). Control of salinity on the mixed layer depth in the world ocean: 1. General description. *Journal of Geophysical Research: Oceans*, 112(C6):C06011.

de Lavergne, C., Palter, J. B., Galbraith, E. D., Bernardello, R., and Marinov, I. (2014). Cessation of deep convection in the open Southern Ocean under anthropogenic climate change. *Nature Climate Change*, 4(4):278–282.

Dee, D. P., Uppala, S. M., Simmons, A. J., Berrisford, P., Poli, P., Kobayashi, S., Andrae, U., Balmaseda, M. A., Balsamo, G., Bauer, P., Bechtold, P., Beljaars, A. C. M., van de Berg, L., Bidlot, J., Bormann, N., Delsol, C., Dragani, R., Fuentes, M., Geer, A. J., Haimberger, L., Healy, S. B., Hersbach, H., Hólm, E. V., Isaksen, L., Kållberg, P., Köhler, M., Matricardi, M., McNally, A. P., Monge-Sanz, B. M., Morcrette, J.-J., Park, B.-K., Peubey, C., de Rosnay, P., Tavolato, C., Thépaut, J.-N., and Vitart, F. (2011). The ERA-Interim reanalysis: configuration and performance of the data assimilation system. *Quarterly Journal of the Royal Meteorological Society*, 137(656):553–597.

Delworth, T. L., Rosati, A., Anderson, W., Adcroft, A. J., Balaji, V., Benson, R., Dixon, K., Griffies, S. M., Lee, H.-C., Pacanowski, R. C., Vecchi, G. A., Wittenberg, A. T., Zeng, F., and Zhang, R. (2011). Simulated Climate and Climate Change in the GFDL CM2.5 High-Resolution Coupled Climate Model. *Journal of Climate*, 25(8):2755–2781.

Demory, M.-E., Vidale, P. L., Roberts, M. J., Berrisford, P., Strachan, J., Schiemann, R., and Mizielinski, M. S. (2014). The role of horizontal resolution in simulating drivers of the global hydrological cycle. *Climate Dynamics*, 42(7):2201–2225.

Dickson, R. R., Meincke, J., Malmberg, S.-A., and Lee, A. J. (1988). The "great salinity anomaly" in the Northern North Atlantic 1968–1982. *Progress in Oceanography*, 20(2):103–151.

DiNezio, P. N., Vecchi, G. A., and Clement, A. C. (2013). Detectability of Changes in the Walker Circulation in Response to Global Warming. *Journal of Climate*, 26(12):4038–4048.

Dommenget, D. (2009). The Ocean's Role in Continental Climate Variability and Change. *Journal of Climate*, 22(18):4939–4952.

Dong, S., Garzoli, S. L., and Baringer, M. (2009). An assessment of the seasonal mixed layer salinity budget in the Southern Ocean. *Journal of Geophysical Research: Oceans*, 114(C12).

Drushka, K., Sprintall, J., Gille, S. T., and Wijffels, S. (2011). In Situ Observations of Madden–Julian Oscillation Mixed Layer Dynamics in the Indian and Western Pacific Oceans. *Journal of Climate*, 25(7):2306–2328.

Durack, P. (2015). Ocean Salinity and the Global Water Cycle. *Oceanography*, 28(1):20–31.

Durack, P. J. and Wijffels, S. E. (2010). Fifty-Year Trends in Global Ocean Salinities and Their Relationship to Broad-Scale Warming. *Journal of Climate*, 23(16):4342–4362.

Durack, P. J., Wijffels, S. E., and Gleckler, P. J. (2014). Long-term sea-level change revisited: the role of salinity. *Environmental Research Letters*, 9(11):114017.

Durack, P. J., Wijffels, S. E., and Matear, R. J. (2012). Ocean Salinities Reveal Strong Global Water Cycle Intensification During 1950 to 2000. *Science*, 336(6080):455–458.

Ent, R. J. v. d. and Savenije, H. H. G. (2013). Oceanic sources of continental precipitation and the correlation with sea surface temperature. *Water Resources Research*, 49(7):3993–4004.

Farrar, J. T., Rainville, L., Plueddemann, A. J., Kessler, W. S., Lee, C. M., Hodges, B. A., Schmitt, R. W., Edson, J. B., Riser, S. C., Eriksen, C. C., and Fratantoni, D. M. (2015). Salinity and temperature balances at the SPURS central mooring during fall and winter. *Oceanography*.

Ferreira, D., Cessi, P., Coxall, H. K., de Boer, A., Dijkstra, H. A., Drijfhout, S. S., Eldevik, T., Harnik, N., McManus, J. F., Marshall, D. P., Nilsson, J., Roquet, F., Schneider, T., and Wills, R. C. (2018). Atlantic-Pacific Asymmetry in Deep Water Formation. *Annual Review of Earth and Planetary Sciences*, 46(1):327–352.

Field, C. B., Barros, V. R., and Coauthors (2014). AR5 Climate Change 2014: Impacts, Adaptation, and Vulnerability. Technical report, IPCC.

Flato, G. M., Marotzke, J., Abiodun, B., Braconnot, P., Chou, S., Collins, W., and Cox, P. (2014). Evaluation of Climate Models. In *Climate Change 2013 – The Physical Science Basis: Working Group I Contribution to the Fifth Assessment Report of the Intergovernmental Panel on Climate Change*, pages 741–866. Cambridge University Press.

Forget, G., Campin, J.-M., Heimbach, P., Hill, C. N., Ponte, R. M., and Wunsch, C. (2015). ECCO version 4: an integrated framework for non-linear inverse modeling and global ocean state estimation. *Geosci. Model Dev.*, 8(10):3071–3104.

Forster, P. M., Andrews, T., Good, P., Gregory, J. M., Jackson, L. S., and Zelinka, M. (2013). Evaluating adjusted forcing and model spread for historical and future scenarios in the CMIP5 generation of climate models. *Journal of Geophysical Research: Atmospheres*, 118(3):1139–1150.

Foukal, N. P. and Lozier, M. S. (2016). No inter-gyre pathway for sea-surface temperature anomalies in the North Atlantic. *Nature Communications*, 7:11333.

Fox-Kemper, B., Danabasoglu, G., Ferrari, R., Griffies, S. M., Hallberg, R. W., Holland, M. M., Maltrud, M. E., Peacock, S., and Samuels, B. L. (2011). Parameterization of mixed layer eddies. III: Implementation and impact in global ocean climate simulations. *Ocean Modelling*, 39(1):61–78.

Gaffen, D. J., Rosen, R. D., Salstein, D. A., and Boyle, J. S. (1997). Evaluation of Tropospheric Water Vapor Simulations from the Atmospheric Model Intercomparison Project. *Journal of Climate*, 10(7):1648–1661.

Gaspar, P., Grégoris, Y., and Lefevre, J.-M. (1990). A simple eddy kinetic energy model for simulations of the oceanic vertical mixing: Tests at station Papa and long-term upper ocean study site. *Journal of Geophysical Research: Oceans*, 95(C9):16179–16193.

Gebbie, G. and Huybers, P. (2019). The Little Ice Age and 20th-century deep Pacific cooling. *Science*, 363(6422):70–74.

Gent, P. R. and Mcwilliams, J. C. (1990). Isopycnal Mixing in Ocean Circulation Models. *Journal of Physical Oceanography*, 20(1):150–155.

Gimeno, L., Drumond, A., Nieto, R., Trigo, R. M., and Stohl, A. (2010). On the origin of continental precipitation. *Geophysical Research Letters*, 37(13).

Gimeno, L., Nieto, R., Drumond, A., Durán-Quesada, A. M., Stohl, A., Sodemann, H., and Trigo, R. M. (2011). A close look at oceanic sources of continental precipitation. *Eos, Transactions American Geophysical Union*, 92(23):193–194.

Goldsbrough, G. R. (1933). Ocean currents produced by evaporation and precipitation. *Proceedings of the Royal Society of London. Series A, Containing Papers of a Mathematical and Physical Character*, 141(845):512–517.

Gordon, A., Giulivi, C., Busecke, J., and Bingham, F. (2015). Differences Among Subtropical Surface Salinity Patterns. *Oceanography*, 28(1):32–39.

Haarsma, R. J., Roberts, M. J., Vidale, P. L., Senior, C. A., Bellucci, A., Bao, Q., Chang, P., Corti, S., Fučkar, N. S., Guemas, V., Hardenberg, J. v., Hazeleger, W., Kodama, C., Koenigk, T., Leung, L. R., Lu, J., Luo, J.-J., Mao, J., Mizielinski, M. S., Mizuta, R., Nobre, P., Satoh, M., Scoccimarro, E., Semmler, T., Small, J., and Storch, J.-S. v. (2016). High Resolution Model Intercomparison Project (HighResMIP v1.0) for CMIP6. *Geoscientific Model Development*, 9(11):4185–4208.

Hasumi, H. (2002). Sensitivity of the Global Thermohaline Circulation to Interbasin Freshwater Transport by the Atmosphere and the Bering Strait Throughflow. *Journal of Climate*, 15(17):2516–2526.

Hegerl, G. C., Black, E., Allan, R. P., Ingram, W. J., Polson, D., Trenberth, K. E., Chadwick, R. S., Arkin, P. A., Sarojini, B. B., Becker, A., Dai, A., Durack, P. J., Easterling, D., Fowler, H. J., Kendon, E. J., Huffman, G. J., Liu, C., Marsh, R., New, M., Osborn, T. J., Skliris, N., Stott, P. A., Vidale, P.-L., Wijffels, S. E., Wilcox, L. J., Willett, K. M., and Zhang, X. (2014). Challenges in Quantifying Changes in the Global Water Cycle. *Bulletin of the American Meteorological Society*, 96(7):1097–1115.

Held, I. M. and Soden, B. J. (2006). Robust Responses of the Hydrological Cycle to Global Warming. *Journal of Climate*, 19(21):5686–5699.

Heuzé, C., Heywood, K. J., Stevens, D. P., and Ridley, J. K. (2014). Changes in Global Ocean Bottom Properties and Volume Transports in CMIP5 Models under Climate Change Scenarios. *Journal of Climate*, 28(8):2917–2944.

Hirschi, J. and Marotzke, J. (2007). Reconstructing the Meridional Overturning Circulation from Boundary Densities and the Zonal Wind Stress. *Journal of Physical Oceanography*, 37(3):743–763.

Hu, Q. and Buyanovsky, G. (2003). Climate Effects on Corn Yield in Missouri. *Journal of Applied Meteorology*, 42(11):1626–1635.

Huang, R. (2005). Contribution of oceanic circulation to the polewar heat flux. *Journal of Ocean University of China*, 4(4):277–287.

Huang, R. X. and Schmitt, R. W. (1993). The Goldsbrough–Stommel Circulation of the World Oceans. *Journal of Physical Oceanography*, 23(6):1277–1284.

Huntington, T. G. (2006). Evidence for intensification of the global water cycle: Review and synthesis. *Journal of Hydrology*, 319(1):83–95.

Hwang, Y.-T. and Frierson, D. M. W. (2013). Link between the double-Intertropical Convergence Zone problem and cloud biases over the Southern Ocean. *Proceedings of the National Academy of Sciences*, 110(13):4935–4940.

Johnson, B. K., Bryan, F. O., Grodsky, S. A., and Carton, J. A. (2016). Climatological Annual Cycle of the Salinity Budgets of the Subtropical Maxima. *Journal of Physical Oceanography*, 46(10):2981–2994.

Johnson, E. S., Lagerloef, G. S. E., Gunn, J. T., and Bonjean, F. (2002). Surface salinity advection in the tropical oceans compared with atmospheric freshwater forcing: A trial balance. *Journal of Geophysical Research: Oceans*, 107(C12):8014.

Josey, S. A., Gulev, S., and Yu, L. (2013). Chapter 5 - Exchanges Through the Ocean Surface. In Siedler, G., Griffies, S. M., Gould, J., and Church, J. A., editors, *International Geophysics*, volume 103 of *Ocean Circulation and Climate*, pages 115–140. Academic Press.

Kim, S.-B., Fukumori, I., and Lee, T. (2006). The Closure of the Ocean Mixed Layer Temperature Budget Using Level-Coordinate Model Fields. *Journal of Atmospheric and Oceanic Technology*, 23(6):840–853.

Knutson, T. R. and Manabe, S. (1995). Time-Mean Response over the Tropical Pacific to Increased C02 in a Coupled Ocean-Atmosphere Model. *Journal of Climate*, 8(9):2181–2199.

Kuhlbrodt, T., Griesel, A., Montoya, M., Levermann, A., Hofmann, M., and Rahmstorf, S. (2007). On the driving processes of the Atlantic meridional overturning circulation. *Reviews of Geophysics*, 45(2).

Lange, M. and van Sebille, E. (2017). Parcels v0.9: prototyping a Lagrangian ocean analysis framework for the petascale age. *Geosci. Model Dev.*, 10(11):4175–4186.

Large, W. G., McWilliams, J. C., and Doney, S. C. (1994). Oceanic vertical mixing: A review and a model with a nonlocal boundary layer parameterization. *Reviews of Geophysics*, 32(4):363–403.

Large, W. G. and Yeager, S. G. (2009). The global climatology of an interannually varying air–sea flux data set. *Climate Dynamics*, 33(2-3):341–364.

Latif, M., Roeckner, E., Mikolajewicz, U., and Voss, R. (2000). Tropical Stabilization of the Thermohaline Circulation in a Greenhouse Warming Simulation. *Journal of Climate*, 13(11):1809–1813.

Lavender, K. L., Davis, R. E., and Owens, W. B. (2002). Observations of Open-Ocean Deep Convection in the Labrador Sea from Subsurface Floats. *Journal of Physical Oceanography*, 32(2):511–526.

Laîné, A., Nakamura, H., Nishii, K., and Miyasaka, T. (2014). A diagnostic study of future evaporation changes projected in CMIP5 climate models. *Climate Dynamics*, 42(9):2745–2761.

Lee, J.-Y. and Wang, B. (2014). Future change of global monsoon in the CMIP5. *Climate Dynamics*, 42(1):101–119.

Lenaerts, J. T. M., Bars, D. L., Kampenhout, L. v., Vizcaino, M., Enderlin, E. M., and Broeke, M. R. v. d. (2015). Representing Greenland ice sheet freshwater fluxes in climate models. *Geophysical Research Letters*, 42(15):6373–6381.

Levang, S. J. and Schmitt, R. W. (2015). Centennial Changes of the Global Water Cycle in CMIP5 Models. *Journal of Climate*, 28(16):6489–6502.

Li, G. and Xie, S.-P. (2013). Tropical Biases in CMIP5 Multimodel Ensemble: The Excessive Equatorial Pacific Cold Tongue and Double ITCZ Problems. *Journal of Climate*, 27(4):1765–1780.

Liepert, B. G. and Lo, F. (2013). CMIP5 update of 'Inter-model variability and biases of the global water cycle in CMIP3 coupled climate models'. *Environmental Research Letters*, 8(2):029401.

Liepert, B. G. and Previdi, M. (2012). Inter-model variability and biases of the global water cycle in CMIP3 coupled climate models. *Environmental Research Letters*, 7(1):014006.

Lin, J.-L. (2007). The Double-ITCZ Problem in IPCC AR4 Coupled GCMs: Ocean–Atmosphere Feedback Analysis. *Journal of Climate*, 20(18):4497–4525.

Lohmann, G. (2003). Atmospheric and oceanic freshwater transport during weak Atlantic overturning circulation. *Tellus A: Dynamic Meteorology and Oceanography*, 55(5):438–449.

Lozier, M. S. (2010). Deconstructing the Conveyor Belt. *Science*, 328(5985):1507–1511.

Lozier, M. S. and Stewart, N. M. (2008). On the Temporally Varying Northward Penetration of Mediterranean Overflow Water and Eastward Penetration of Labrador Sea Water. *Journal of Physical Oceanography*, 38(9):2097–2103.

Lumpkin, R. and Johnson, G. C. (2013). Global ocean surface velocities from drifters: Mean, variance, El Niño–Southern Oscillation response, and seasonal cycle. *Journal of Geophysical Research: Oceans*, 118(6):2992–3006.

Ma, J. and Xie, S.-P. (2012). Regional Patterns of Sea Surface Temperature Change: A Source of Uncertainty in Future Projections of Precipitation and Atmospheric Circulation. *Journal of Climate*, 26(8):2482–2501.

Ma, J., Xie, S.-P., and Kosaka, Y. (2011). Mechanisms for Tropical Tropospheric Circulation Change in Response to Global Warming. *Journal of Climate*, 25(8):2979–2994.

Maes, C., Grima, N., Blanke, B., Martinez, E., Paviet-Salomon, T., and Huck, T. (2018). A Surface "Superconvergence" Pathway Connecting the South Indian Ocean to the Subtropical South Pacific Gyre. *Geophysical Research Letters*, 45(4):1915–1922.

Marshall, J. and Schott, F. (1999). Open-ocean convection: Observations, theory, and models. *Reviews of Geophysics*, 37(1):1–64.

Marshall, J., Scott, J. R., Armour, K. C., Campin, J.-M., Kelley, M., and Romanou, A. (2015). The ocean's role in the transient response of climate to abrupt greenhouse gas forcing. *Climate Dynamics*, 44(7-8):2287–2299.

Moisan, J. R. and Niiler, P. P. (1998). The Seasonal Heat Budget of the North Pacific: Net Heat Flux and Heat Storage Rates (1950–1990). *Journal of Physical Oceanography*, 28(3):401–421.

Molinari, R. L., Fine, R. A., Wilson, W. D., Curry, R. G., Abell, J., and McCartney, M. S. (1998). The arrival of recently formed Labrador sea water in the Deep Western Boundary Current at 26.5°N. *Geophysical Research Letters*, 25(13):2249–2252.

Muller, C. J. and O'Gorman, P. A. (2011). An energetic perspective on the regional response of precipitation to climate change. *Nature Climate Change*, 1(5):266–271.

Ohshima, K. I., Fukamachi, Y., Williams, G. D., Nihashi, S., Roquet, F., Kitade, Y., Tamura, T., Hirano, D., Herraiz-Borreguero, L., Field, I., Hindell, M., Aoki, S., and Wakatsuchi, M. (2013). Antarctic Bottom Water production by intense sea-ice formation in the Cape Darnley polynya. *Nature Geoscience*, 6(3):235–240.

O'Gorman, P. A., Allan, R. P., Byrne, M. P., and Previdi, M. (2012). Energetic Constraints on Precipitation Under Climate Change. *Surveys in Geophysics*, 33(3):585–608.

Peixóto, J. P. and Oort, A. H. (1983). The Atmospheric Branch Of The Hydrological Cycle And Climate. In Street-Perrott, A., Beran, M., and Ratcliffe, R., editors, *Variations in the Global Water Budget*, pages 5–65. Springer Netherlands, Dordrecht.

Pierce, D. W., Gleckler, P. J., Barnett, T. P., Santer, B. D., and Durack, P. J. (2012). The fingerprint of human-induced changes in the ocean's salinity and temperature fields. *Geophysical Research Letters*, 39(21).

Pincus, R., Batstone, C. P., Hofmann, R. J. P., Taylor, K. E., and Glecker, P. J. (2008). Evaluating the present-day simulation of clouds, precipitation, and radiation in climate models. *Journal of Geophysical Research: Atmospheres*, 113(D14).

Ponte, R. M. and Vinogradova, N. T. (2016). An assessment of basic processes controlling mean surface salinity over the global ocean. *Geophysical Research Letters*, 43(13):2016GL069857.

Potter, R. A. and Lozier, M. S. (2004). On the warming and salinification of the Mediterranean outflow waters in the North Atlantic. *Geophysical Research Letters*, 31(1).

Purich, A., England, M. H., Cai, W., Sullivan, A., and Durack, P. J. (2018). Impacts of Broad-Scale Surface Freshening of the Southern Ocean in a Coupled Climate Model. *Journal of Climate*, 31(7):2613–2632.

Qin, X., van Sebille, E., and Sen Gupta, A. (2014). Quantification of errors induced by temporal resolution on Lagrangian particles in an eddy-resolving model. *Ocean Modelling*, 76:20–30.

Qu, T., Gao, S., and Fukumori, I. (2011). What governs the North Atlantic salinity maximum in a global GCM? *Geophysical Research Letters*, 38(7):L07602.

Rao, R. R. and Sivakumar, R. (2003). Seasonal variability of sea surface salinity and salt budget of the mixed layer of the north Indian Ocean. *Journal of Geophysical Research: Oceans*, 108(C1):9–1–9–14.

Redi, M. H. (1982). Oceanic Isopycnal Mixing by Coordinate Rotation. *Journal of Physical Oceanography*, 12(10):1154–1158.

Reintges, A., Martin, T., Latif, M., and Keenlyside, N. S. (2017). Uncertainty in twenty-first century projections of the Atlantic Meridional Overturning Circulation in CMIP3 and CMIP5 models. *Climate Dynamics*, 49(5):1495–1511.

Richter, I. and Xie, S. P. (2010). Moisture transport from the Atlantic to the Pacific basin and its response to North Atlantic cooling and global warming. *Climate Dynamics*, 35(2-3):551–566.

Risien, C. M. and Chelton, D. B. (2008). A Global Climatology of Surface Wind and Wind Stress Fields from Eight Years of QuikSCAT Scatterometer Data. *Journal of Physical Oceanography*, 38(11):2379–2413.

Schanze, J. J., Schmitt, R. W., and Yu, L. L. (2010). The global oceanic freshwater cycle: A state-of-the-art quantification. *Journal of Marine Research*, 68(3-4):569–595(27).

Schanze, J. J. J. J. (2013). *The production of temperature and salinity variance and covariance : implications for mixing*. Thesis, Massachusetts Institute of Technology.

Schmidtko, S., Johnson, G. C., and Lyman, J. M. (2013). MIMOC: A global monthly isopycnal upper-ocean climatology with mixed layers. *Journal of Geophysical Research: Oceans*, 118(4):1658–1672.

Schmitt, R. (2008). Salinity and the Global Water Cycle. *Oceanography*, 21(1):12–19.

Schmitt, R. and Blair, A. (2015). A River of Salt. *Oceanography*, 28(1):40–45.

Schmittner, A., Silva, T. A. M., Fraedrich, K., Kirk, E., and Lunkeit, F. (2010). Effects of Mountains and Ice Sheets on Global Ocean Circulation. *Journal of Climate*, 24(11):2814–2829.

Silvano, A., Rintoul, S. R., Peña-Molino, B., Hobbs, W. R., Wijk, E. v., Aoki, S., Tamura, T., and Williams, G. D. (2018). Freshening by glacial meltwater enhances melting of ice shelves and reduces formation of Antarctic Bottom Water. *Science Advances*, 4(4):eaap9467.

Sohn, B.-J., Smith, E. A., Robertson, F. R., and Park, S.-C. (2004). Derived Over-Ocean Water Vapor Transports from Satellite-Retrieved E - P Datasets. *Journal of Climate*, 17(6):1352–1365.

Stammer, D., Wunsch, C., Giering, R., Eckert, C., Heimbach, P., Marotzke, J., Adcroft, A., Hill, C. N., and Marshall, J. (2003). Volume, heat, and freshwater transports of the global ocean circulation 1993–2000, estimated from a general circulation model constrained by World Ocean Circulation Experiment (WOCE) data. *Journal of Geophysical Research: Oceans*, 108(C1):7–1–7–23.

Stephens, G. L. and Ellis, T. D. (2008). Controls of Global-Mean Precipitation Increases in Global Warming GCM Experiments. *Journal of Climate*, 21(23):6141–6155.

Stephens, G. L., L'Ecuyer, T., Forbes, R., Gettelmen, A., Golaz, J.-C., Bodas-Salcedo, A., Suzuki, K., Gabriel, P., and Haynes, J. (2010). Dreary state of precipitation in global models. *Journal of Geophysical Research: Atmospheres*, 115(D24).

Stommel, H. (1961). Thermohaline Convection with Two Stable Regimes of Flow. *Tellus*, 13(2):224–230.

Stommel, H. (1979). Determination of water mass properties of water pumped down from the Ekman layer to the geostrophic flow below. *Proceedings of the National Academy of Sciences*, 76(7):3051–3055.

Stommel, H. (1980). Asymmetry of interoceanic fresh-water and heat fluxes. *Proceedings of the National Academy of Sciences*, 77(5):2377–2381.

Stott, P. A., Sutton, R. T., and Smith, D. M. (2008). Detection and attribution of Atlantic salinity changes. *Geophysical Research Letters*, 35(21).

Stouffer, R. J., Yin, J., Gregory, J. M., Dixon, K. W., Spelman, M. J., Hurlin, W., Weaver, A. J., Eby, M., Flato, G. M., Hasumi, H., Hu, A., Jungclaus, J. H., Kamenkovich, I. V., Levermann, A., Montoya, M., Murakami, S., Nawrath, S., Oka, A., Peltier, W. R., Robitaille, D. Y., Sokolov, A., Vettoretti, G., and Weber, S. L. (2006). Investigating the Causes of the Response of the Thermohaline Circulation to Past and Future Climate Changes. *Journal of Climate*, 19(8):1365–1387.

Su, H., Jiang, J. H., Neelin, J. D., Shen, T. J., Zhai, C., Yue, Q., Wang, Z., Huang, L., Choi, Y.-S., Stephens, G. L., and Yung, Y. L. (2017). Tightening of tropical ascent and high clouds key to precipitation change in a warmer climate. *Nature Communications*, 8:15771.

Sévellec, F. and Fedorov, A. V. (2016). AMOC sensitivity to surface buoyancy fluxes: Stronger ocean meridional heat transport with a weaker volume transport? *Climate Dynamics*, 47(5):1497–1513.

Talley, L. D. (2008). Freshwater transport estimates and the global overturning circulation: Shallow, deep and throughflow components. *Progress in Oceanography*, 78(4):257–303.

Taylor, K. E., Stouffer, R. J., and Meehl, G. A. (2011). An Overview of CMIP5 and the Experiment Design. *Bulletin of the American Meteorological Society*, 93(4):485–498.

Terray, L., Corre, L., Cravatte, S., Delcroix, T., Reverdin, G., and Ribes, A. (2011). Near-Surface Salinity as Nature's Rain Gauge to Detect Human Influence on the Tropical Water Cycle. *Journal of Climate*, 25(3):958–977.

Tian, B., Fetzer, E. J., Kahn, B. H., Teixeira, J., Manning, E., and Hearty, T. (2013). Evaluating CMIP5 models using AIRS tropospheric air temperature and specific humidity climatology. *Journal of Geophysical Research: Atmospheres*, 118(1):114–134.

Tokinaga, H., Xie, S.-P., Deser, C., Kosaka, Y., and Okumura, Y. M. (2012). Slowdown of the Walker circulation driven by tropical Indo-Pacific warming. *Nature*, 491(7424):439–443.

Trenberth, K. E. and Caron, J. M. (2001). Estimates of Meridional Atmosphere and Ocean Heat Transports. *Journal of Climate*, 14(16):3433–3443.

Trenberth, K. E., Smith, L., Qian, T., Dai, A., and Fasullo, J. (2007). Estimates of the Global Water Budget and Its Annual Cycle Using Observational and Model Data. *Journal of Hydrometeorology*, 8(4):758–769.

Turner, A. G. and Annamalai, H. (2012). Climate change and the South Asian summer monsoon. *Nature Climate Change*, 2(8):587–595.

van Sebille, E., Griffies, S. M., Abernathey, R., Adams, T. P., Berloff, P., Biastoch, A., Blanke, B., Chassignet, E. P., Cheng, Y., Cotter, C. J., Deleersnijder, E., Döös, K., Drake, H. F., Drijfhout, S., Gary, S. F., Heemink, A. W., Kjellsson, J., Koszalka, I. M., Lange, M., Lique, C., MacGilchrist, G. A., Marsh, R., Mayorga Adame, C. G., McAdam, R., Nencioli, F., Paris, C. B., Piggott, M. D., Polton, J. A., Rühs, S., Shah, S. H. A. M.,

Thomas, M. D., Wang, J., Wolfram, P. J., Zanna, L., and Zika, J. D. (2018). Lagrangian ocean analysis: Fundamentals and practices. *Ocean Modelling*, 121:49–75.

Vecchi, G. A., Soden, B. J., Wittenberg, A. T., Held, I. M., Leetmaa, A., and Harrison, M. J. (2006). Weakening of tropical Pacific atmospheric circulation due to anthropogenic forcing. *Nature*, 441(7089):73–76.

Vinogradova, N. T. and Ponte, R. M. (2017). In Search of Fingerprints of the Recent Intensification of the Ocean Water Cycle. *Journal of Climate*, 30(14):5513–5528.

Visbeck, M. (2007). Oceanography: Power of pull. *Nature*, 447:383.

Vizcaíno, M., Lipscomb, W. H., Sacks, W. J., and van den Broeke, M. (2013). Greenland Surface Mass Balance as Simulated by the Community Earth System Model. Part II: Twenty-First-Century Changes. *Journal of Climate*, 27(1):215–226.

Walin, G. (1982). On the relation between sea-surface heat flow and thermal circulation in the ocean. *Tellus*, 34(2):187–195.

Wang, C., Zhang, L., and Lee, S.-K. (2012). Response of Freshwater Flux and Sea Surface Salinity to Variability of the Atlantic Warm Pool. *Journal of Climate*, 26(4):1249–1267.

Wijffels, S. E., Schmitt, R. W., Bryden, H. L., and Stigebrandt, A. (1992). Transport of Freshwater by the Oceans. *Journal of Physical Oceanography*, 22(2):155–162.

Williams, R. G., Marshall, J. C., and Spall, M. A. (1995). Does Stommel's Mixed Layer "Demon" Work? *Journal of Physical Oceanography*, 25(12):3089–3102.

Wüst, G. (1936). Surface Salinity, Evaporation and Precipitation over the World's Ocean. In *Länderkundliche Forschung*, pages 347–359. Festschrift Norbert Krebs, Stuttgart, Germany.

Xu, H., Xie, S.-P., Wang, Y., and Small, R. J. (2005). Effects of Central American Mountains on the Eastern Pacific Winter ITCZ and Moisture Transport. *Journal of Climate*, 18(18):3856–3873.

Yoshimori, M. and Abe-Ouchi, A. (2011). Sources of Spread in Multimodel Projections of the Greenland Ice Sheet Surface Mass Balance. *Journal of Climate*, 25(4):1157–1175.

Yu, L. (2011). A global relationship between the ocean water cycle and near-surface salinity. *Journal of Geophysical Research: Oceans*, 116(C10):C10025.

Yu, L. and Weller, R. A. (2007). Objectively Analyzed Air–Sea Heat Fluxes for the Global Ice-Free Oceans (1981–2005). *Bulletin of the American Meteorological Society*, 88(4):527–539.

Zaucker, F. and Broecker, W. S. (1992). The influence of atmospheric moisture transport on the fresh water balance of the Atlantic drainage basin: General circulation model simulations and observations. *Journal of Geophysical Research: Atmospheres*, 97(D3):2765–2773.

Zaucker, F., Stocker, T. F., and Broecker, W. S. (1994). Atmospheric freshwater fluxes and their effect on the global thermohaline circulation. *Journal of Geophysical Research: Oceans*, 99(C6):12443–12457.

Zhou, T., Zhang, X., and Wang, S. (2000). The Interbasin Transport of Atmospheric Moisture Evaluated from NCEP/NCAR Reanalysis Data. *Journal of Meteorological Research*, 14(2):159–172.

Zhu, J., Huang, B., Zhang, R.-H., Hu, Z.-Z., Kumar, A., Balmaseda, M. A., Marx, L., and Iii, J. L. K. (2014). Salinity anomaly as a trigger for ENSO events. *Scientific Reports*, 4:6821.

Zhurbas, V., Lyzhkov, D., and Kuzmina, N. (2014). Drifter-derived estimates of lateral eddy diffusivity in the World Ocean with emphasis on the Indian Ocean and problems of parameterisation. *Deep Sea Research Part I: Oceanographic Research Papers*, 83:1–11.

Zou, S. and Lozier, M. S. (2016). Breaking the Linkage Between Labrador Sea Water Production and Its Advective Export to the Subtropical Gyre. *Journal of Physical Oceanography*, 46(7):2169–2182.